July 2021

PERFORMANCE EVALUATION OF GAS LIFT VALVES USING NUMERICAL SIMULATION

Felipe Simoes Maciel
Louisiana State University and Agricultural and Mechanical College

PERFORMANCE EVALUATION OF GAS LIFT VALVES USING NUMERICAL SIMULATION

A Thesis

Submitted to the Graduate Faculty of the
Louisiana State University and
Agricultural and Mechanical College
in partial fulfillment of the
requirements for the degree of
Master of Science in Petroleum Engineering

in

The Department of Petroleum Engineering

by
Felipe Simoes Maciel
B.S. Federal University of Espírito Santo, 2016
M.S. Federal University of Espírito Santo, 2020
August 2021

To the Lord God for all the inspiration and love, to my parents Pedro and Ma Josefa S. Maciel, to my brothers Rodrigo and Alvaro, and my fiancée Fabiana Trindade for the unique support in all my projects throughout my career.

Acknowledgments

I would like to sincerely thank my advisor and committee chair, Dr. Paulo Waltrich, for all of his brilliant guidance and support while conducting this work. I also extend my appreciation to Dr. Ozdemir and Dr. Thompson for serving as committee members.

Also, I am forever grateful to my parents, Maria Josefa S. Maciel and Pedro C. Maciel, who continued to support me with all their love and guidance from a distance. I thank them for always encouraging me to keep working hard and do my best in everything. I also thank my brothers, Rodrigo and Alvaro Simoes Maciel, for sharing special moments and their wise advice. I am grateful to always have love and support from my brothers. My deep gratitude also goes to my dear fiancée Fabiana T. da Silva. Her love, kindness, patience, and friendship were fundamental and always moved me to do my best. I am also thankful to my fiancée's family—Silvia, Fabio, and Filipe—for all of their kindness and support. My journey has taken on a deeper meaning by having all of these remarkable people around me, and I dedicate this milestone to them.

I am also grateful to all of my colleagues and friends, including Bruno Xavier, Ligia Tornizelo, Renato Coutinho, Hand Redlich, Khodur Altarabusi, and Gerardo Sepulveda for all of their support, both academic and personal. I also thank Mrs. Janette Wooden, Ms. Janet Dugas, Mrs. Andi Donmyer, Mr. Doug, and Mr. Andreau Trepagnier for all of their technical and administrative support. I also extend my gratitude to the faculty of the Department of Petroleum Engineering.

I also thank the Valve Performance Clearinghouse Project, where I have had the opportunity to interact with brilliant people such as Mr. Ken Decker and the consortium members. I am grateful for the support as well as for the opportunity to work on a research project that can make an impact on the oil production field.

Table of Contents

List of Tables

List of Figures

List of Symbols, Subscripts, and Abbreviations

Symbol	Description
A	Area
a	Coefficients for equation 3.3 and 3.4
b	Coefficients for equation 3.3 and 3.4
C_D	Discharge coefficient
C	Velocity of sound
c_p	Specific heat at constant pressure
c_v	Specific heat at constant temperature
C_v	Flow coefficient
C_{vA}	Coefficient for equation 3.6
C_{vB}	Coefficient for equation 3.6
C_{vC}	Coefficient for equation 3.6
C_{vD}	Coefficient for equation 3.6
d	Diameter
d_{xs}	Stem position
F_k	Correction factor for the ratio of specific heats
g	Acceleration of gravity
G_k	Generation of turbulent kinetic energy due to velocity gradient
G_b	Generation of turbulent kinetic energy due to turbulent fluctuations
H	Energy source
K	Bulk modulus of elasticity
k_c	Thermal conductivity
k	Ideal gas isentropic exponent
m	Mass
M_W	Molecular weight
n	Number of moles
n	Real isentropic exponent
P	Pressure
P'_{cf}	Casing flowing pressure
P_{up}	Upstream pressure
Pr_t	Turbulent Prandtl number
q	Volumetric flow rate
$\overline{\mathrm{q}}$	Average measurements
S_{ij}	Deformation tensor
R	Gas constant
R_{cp}	Critical pressure ratio
R_c	Pressure ratio
R_{cpA}	Coefficient for equation 3.7
R_{cpB}	Coefficient for equation 3.7
R_{cpC}	Coefficient for equation 3.7
R_{cpD}	Coefficient for equation 3.7
T	Temperature
u_i	Velocity in i direction
$u_i{}'$	Velocity fluctuation in the i direction
V	Volume

(table cont'd)

Symbol	Description
v	Specific volume
x	Cartesian coordinates
x_T	Terminal pressure drop ratio
Y	Expansion factor
Z	Compressibility factor
α	Linear thermal expansion coefficient
dp	Differential pressure increase
dv	Differential decrease in volume
ε	Turbulent kinetic energy dissipation rate
ρ	Density
γ	Specific heat ratio
μ	Dynamic viscosity

Subscripts	Description
1	Upstream
1	Initial conditions
2	Final conditions
Avg.	Average
c	Critical
d	Dome
eq	Equivalent
g	Gas
i	Count number
m	Constant
max	Maximum
min	Minimum
p	Port
$R_{eff}.$	Reference
sc	Standard condition

Abbreviation	Description
API	American Petroleum Institute
EOS	Equation of state
GLR	Gas-liquid ratio
GLV	Gas lift valve
IPO	Injection pressure operated
ISA	Instrumentation Society of America
LSU	Louisiana State University
OD	Outer diameter
PPO	Production pressure operated
SCF	Standard cubic feet
VPC	Valve Performance Clearinghouse

Abstract

This work aimed to assess the performance of two numerical simulation methods to replicate flow capacity test (FCT) results and predict the flow coefficient (C_v) and critical pressure ratio (R_{cp}) of gas lift valves (GLVs). FCTs use a modified GLV with an adjustable stem positioning system to obtain pressure as a function of flow rate for different stem positions to calculate C_v and R_{cp}. Therefore, this study used both a one-dimensional (1D) mechanistic model and computational fluid dynamics (CFD) to predict the same variable from the FCT without tests using modified GLVs. This methodology demonstrates accurate results, which were compared to benchmarking information from tests and an extensive GLV database.

This study developed a 1D model and mechanistic flow equation representing the restrictions of GLV internal flow domains. This model considers the equivalent open area at the orifice and check valve and uses experimental data from the dynamic test of the GLV performance test to calibrate the model before running for multiple stem positions. Twelve different GLVs were modeled and simulated using this approach. Similarly, a CFD model of the full GLV including all internal features was built to assess the potential for using CFD to predict the correlation coefficients for flow coefficients (C_v) and critical pressure ration R_{cp}. The results were also compared against experimental data from the Valve Performance Clearinghouse (VPC) database.

The 1D and CFD simulation results show strong consistency and accuracy when compared to experimental results and data from the VPC database. CFD results show greater accuracy than the less complex 1D model results. Most flow coefficients (C_v) and critical pressure ration R_{cp} datapoints from CFD simulations for different stem positions are within a 15% error range. While the 1D model shows higher variability than the CFD methodology, 9 out of the 12 valve

configurations evaluated show the majority of data points for C_v and R_{cp} within a 15% error range of the experimental results. VPC correlation is the best available correlation and predicts flow rates with +/-20% accuracy over the pressure range.

Chapter 1. Introduction

The production lifetime of an oil well typically experiences a natural flow rate decline driven by reservoir energy depletion. Eventually, the reservoir cannot supply enough pressure to naturally lift the fluids to surface facilities. To overcome this issue, artificial lift methods are often employed to lift reservoir fluids to the surface. Artificial lift systems may also be included in well designs to operate from the start of well operation and optimize production. The design of artificial lift methods must consider parameters including fluid properties, gas content, well depth, solids content, downhole pressure, and production flow rates, among others. Notably, the gas lift (GL) method is one of the most commonly deployed artificial lift methods for both offshore and onshore wells (Tang et al., 1999).

GL is a traditional artificial lift method with over 130 years of operation history in the United States and its popularity is linked to its strong reliability and ability to operate at a wide range of production flow rates (Pittman, 1982; Xu et al., 2013). The GL method primarily consists of reducing the bottom hole pressure (BHP) by continuously or intermittently injecting gas into the fluid column. The lighter fluid in the wellbore decreases the density of the flowing fluid mixture, which leads to lower hydrostatic pressure. Subsequently, lower buttonhole pressure creates a higher differential pressure between the bottom hole and surface, which increases production or reestablishes flow when there is insufficient energy to lift the fluids (Coutinho, 2018).

Figure 1.1 presents a schematic of a GL system. In such systems, high-pressure gas is typically injected into the annular space between the casing and the production tubing and then flows down to reach the depth where the gas lift valves (GLVs) are installed. When the annulus

pressure is higher than the tubing pressure, the gas flows through the GLV into the tubing and mixes with wellbore fluids. The gas ultimately reduces the mixture density, which facilitates a production flow to the surface. In the case of a continuous GL, the injection is relatively constant as long as production rates and reservoir pressure remain relatively unchanged. For intermittent GL—typically used when reservoir pressure is insufficient even when the GL injection rate is optimized—the well is shut for a certain amount of time until the reservoir pressure near the wellbore has increased enough to lift the production fluids to the surface. Then, a slug of gas is injected to lift the fluids that accumulated in the wellbore.

The GLV is one of the main elements of this system and functions as a form of communication between the injected gas in the casing and the tubing string. Moreover, GLVs are categorized as either operating valves or unloading valves.

Operating valves (also known as "orifice valves") are typically installed at the deepest point of injection (i.e., closest to the bottom of the well). Additionally, operating valves are always open, with flow only being controlled by the pressure drop and valve orifice size. The second type of GLV is the unloading valve, also known as an injection pressure-operated (IPO) or production pressure-operated (PPO) valve. As their names suggest, the difference between operating and unloading valves is related to their functions in GL operations. Unloading valves are only required for the so-called well unloading process, while the operating valves are designed to allow gas flow only during continuous GL operation.

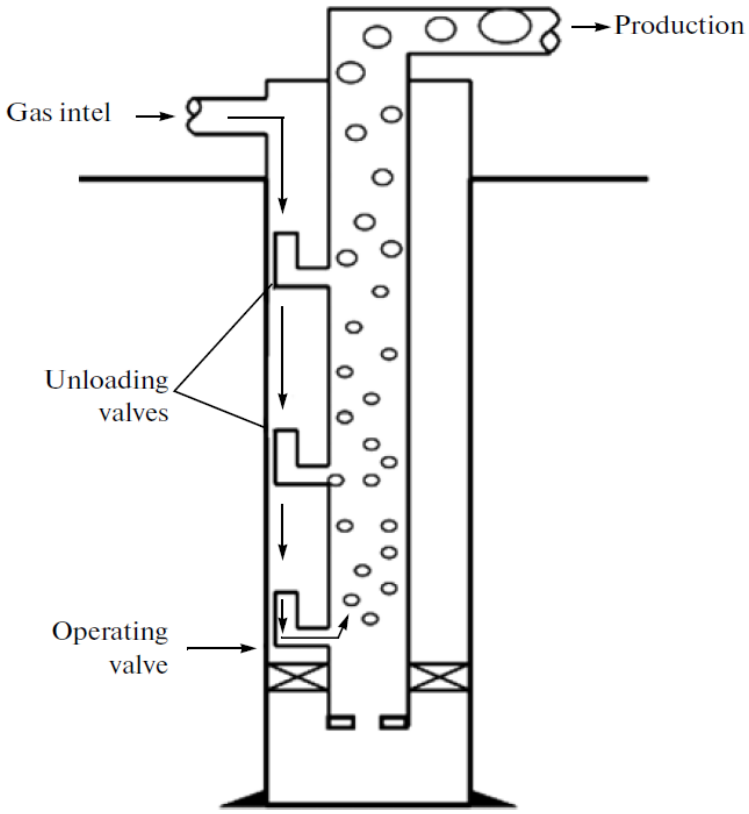

Figure 1.1. Schematic of an oil well producing liquid using a gas lift system (Rasouli et al., 2013).

The unloading process consists of removing the static liquid column from the well (i.e., "unloading" the well), which occurs before initiating continuous production or after well intervention in a GL well. Unloading valves are designed to open at specific set pressures to enable the unloading process. Typically, multiple unloading valves are installed along the well. Parameters such as minimum opening pressure and orifice size are set at the surface before attaching the valves to the tubing string and installing them in the well. One major valve design element is the orifice size and stem position mechanism, which regulates the valve's opening and closing "status" and thus controls the injection gas rate. Moreover, stem movement is governed by a force balance between the injection pressure acting on the bellows areas and the nitrogen pressure

injected within a dome or bellows' volume. A schematic of a typical IPO GLV is provided in Figure 1.2.

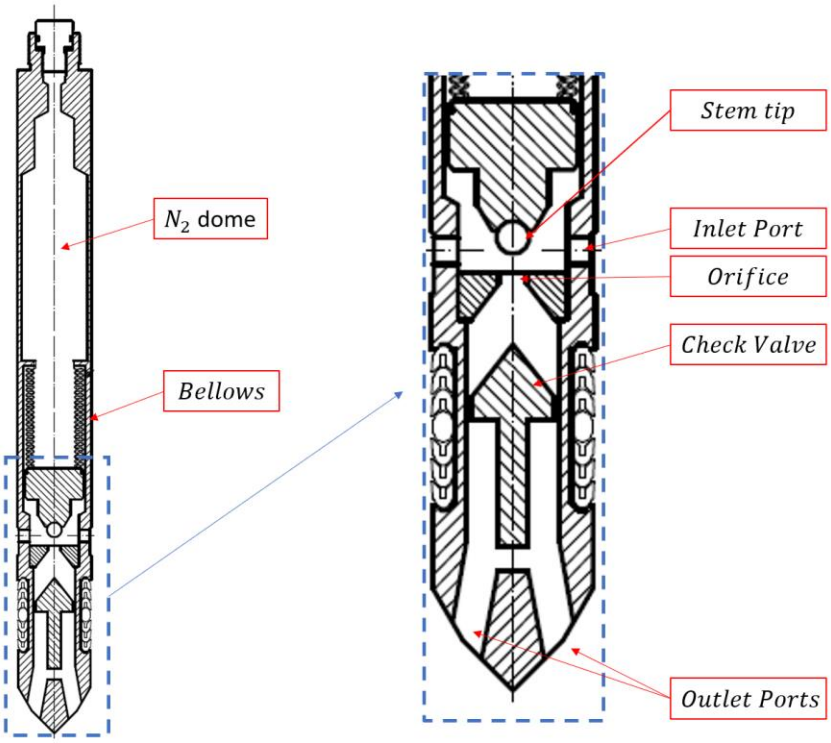

Figure 1.2. Schematic of a typical injection pressure-operated (IPO) gas lift valve. The dashed box provides more details on the major components of an IPO valve. *Source*: Modified from API 19G2 et al. (2010).

1.1. Gas Lift Valve Performance

Valve performance is a crucial factor that dictates the success of a GL system for both unloading and continuous production operations. Since valve parameters are set at the surface and cannot easily be changed without a well intervention, it is important to understand how valves perform under downhole conditions to accurately design GL well systems. Decker (1993) defines GLV performance as a measure of the valve's flow rate in response to changes in the casing and/or

tubing pressure for a given dome set pressure. Poor valve performance might lead to insufficient gas being injected into the tubing, thereby reducing production efficiency or even precluding the unloading process for the designed conditions. On the other hand, an excessive gas flow may create excessive liquid unloading, which may affect separation facilities at the surface and violate restrictions for sand control and water coning, thereby reducing production efficiency. (Economides, 2013). Design details such as valve spacing, compressor capacity, and GLV port sizing are also strongly dependent on valve performance information. Therefore, determining accurate valve performance is of utmost importance for the proper design and operation of GL systems.

Figure 1.3 presents an example of a performance curve for an IPO GLV. Depending on the stem position relative to the seat, the pressure distribution in the valve's flow domain and characteristics of the flow field may differentiate. For a fully open valve with the stem up to a point that makes the minimum restriction flow area the entire orifice area, the maximum flow rate through the valve is achieved. In this case, the flow mode is known as orifice flow. Furthermore, the orifice mode can be divided into two sub-regions: critical and subcritical. For the critical flow, changes in downstream pressure do not affect the flow rate, which remains constant regardless of the downstream pressure. Under subcritical flow conditions, downstream pressure drop considerably affects the flow rate. Notably, while upstream pressure affects the gas flow rate through the GLV in the critical sub-region, downstream pressure does not.

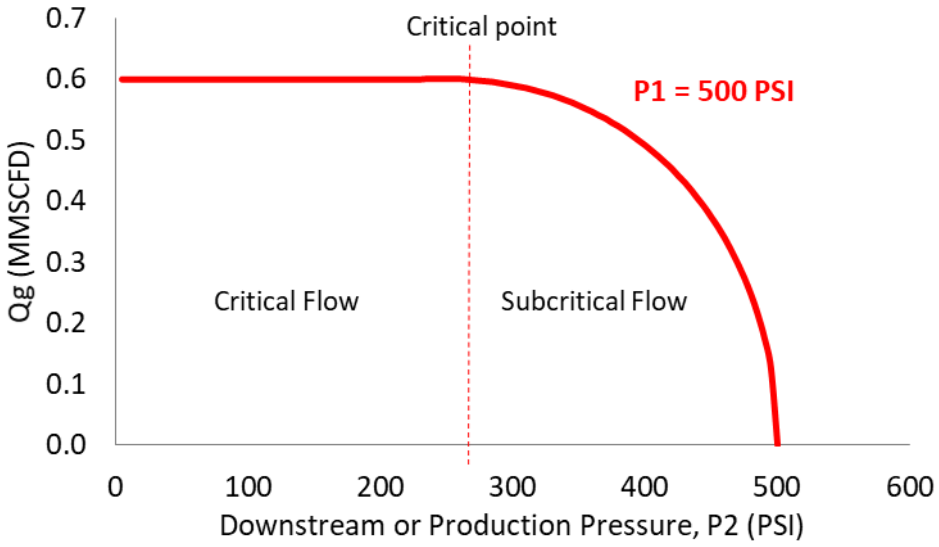

Figure 1.3. Gas lift valve performance curve highlighting the critical and subcritical flow sub-regions.

Equation 1.1 calculates the flow rate (Q) to estimate the flow performance curve. Notably, the flow coefficient (C_v) and pressure ratio (R_p) must be experimentally determined.

$$Q = 32.6 C_v Y P_{inj} \sqrt{R_p/(\gamma_g T_g Z)} \quad 1.1$$

where P_{inj} is injection pressure, T is temperature, γ_g is specific gravity, and Z is the compressibility factor.

Since valve restrictions create hydraulic head loss upstream and downstream of the valve, an experimentally determined factor known as the discharge coefficient (C_d) is introduced in the flow rate equation (Driskell, 1983). C_d accounts for factors such as friction, heat transfer, boundary layer thickness, and other factors that may affect flow and lead to differences between actual and theoretical flow (Brahma, 2019). C_d can be understood as the rate between the actual flow rate (Q_{actual}) and theoretical flow rate (Q_{theo}) while considering the theoretical flow rate through an ideal orifice (ASME, 1971). Regarding the concept of flow coefficient or flow capacity (C_v) that

appears in Equation 1.1, it is used to characterize the capacity or efficiency of a GLV. This constant is related to the geometry of the valve and assumes a specific value for each valve position or valve travel. In summary, the flow capacity of the valve (C_v) accounts for multiple factors such as irreversible losses (discharge coefficient, C_d) and the velocity of approach and contraction coefficient (Driskell, 1983). An accurate prediction of C_v is very important for obtaining an accurate characterization of GLV performance. Mathematically, C_v can be derived from the theorem of energy conservation and is presented in a widely used form in Equation 1.2:

$$C_v = Q\sqrt{\frac{SG}{\Delta P}} \tag{1.2}$$

where Q is the flow rate, SG is the gas specific gravity and ΔP is the pressure drop across the restriction.

The Y term in Equation 1.1 is the expansion factor quantified in pounds per cubic foot. For compressible fluids, expansion occurs with decreasing pressure. Therefore, the specific weight of a fluid decreases as it flows from upstream (high pressure) to downstream of the restriction (Driskell, 1983). As a result, a compressible flow must be accelerated to a greater velocity than an equal mass of an incompressible fluid, such as a liquid. To account for this effect, the expansion factor is added as a correction in the equation for compressible flow rate calculation. The expansion factor Y is determined as follows (Decker, 1993b):

$$Y = 1 - \frac{R_p}{3F_k R_{cp}} \tag{1.3}$$

where R_p is the critical pressure, R_{cp} is the critical pressure ratio, k is the specific heat ratio of the gas defined as the ratio between specific heat at constant pressure and specific heat at constant volume (c_p/c_v). F_k is a correction factor for the ratio of specific heats (k). For air and diatomic

gases, the specific heat is 1.4; however, for other gases and vapor, the critical pressure ratio must be corrected for the difference in thermodynamic properties. The correction factor is defined as $F_k = \frac{k}{1.4}$. Details regarding the definition and derivation of the expansion factor can be found in Driskell (1983).

Critical pressure ratio R_{cp} is a value that indicates the pressure conditions at which the flow transitions to critical or supersonic. At this point, the flow is also known as choked or critical flow. This is a very important concept to consider when designing many types of flow devices. As the flow achieves the critical point, the system reaches its maximum possible mass flow rate condition as a function of downstream pressure. In other words, the mass flow rate after the critical point is no longer dependent on the downstream pressure. The critical pressure P_c is the downstream pressure at the critical pressure ratio. For an ideal gas, the critical pressure can be calculated using the critical pressure ratio equation. The equation describing the critical pressure (P_c) for a compressible fluid and isentropic process with upstream pressure P_1 is expressed as follows (Brill & Mukherjee, 1999):

$$R_{cp} = \frac{P_c}{P_1} = \left(\frac{2}{k+1}\right)^{\frac{k}{k+1}} \tag{1.4}$$

Both C_v and R_{cp} are related to the geometry of the valve. For each valve position or valve travel, the flow coefficient and critical pressure ratio assumes a different value.

A series of experimental procedures and recommendations detailed by the American Petroleum Institute (API) is defined to guide the determination of GLV flow performance. These tests include the following (API 11V2, 2001; API 19G2 et al., 2010; Decker, 1993b):

- Dynamic or live valve test (LVT)

- Load rate test (LRT)
- Flow capacity test (FCT)

The aforementioned tests are described in greater detail in Section 2.7 of this thesis. Notably, each of these tests requires specific equipment, training, and hazard mitigation.

Louisiana State University is currently responsible for the Valve Performance Clearinghouse (VPC) Project, which aims to conduct GLV performance tests and establish a database that facilitates the creation of performance curves for distinct operational conditions. The VPC database gathers a series of coefficients generated from test data that are used to determine the flow performance of GLVs under distinct operational conditions (Decker, 2014). The VPC database contains information for approximately 230 different GLV configurations, including various valve models and port sizes. The information from the VPC database is typically employed to estimate valve performance for real GL systems design. Section 3.1 presents a more detailed description of the VPC database.

Working with high-pressure, high-flow-rate tests increases the complexity of experimental setups, which require significant gas storage volumes and high-pressure equipment. In the context of FCTs, one additional challenge is the need for a modified valve capable of accurately adjusting the stem position of the GLV. Figure 1.4 presents a comparison between the standard GLV and the modified valve with an adjustable screw. Since valve manufacturers do not provide these modified valves, machining work is necessary on the original valve before performing the FCTs. The process of preparing the modified valve is considerably time consuming and expensive. Furthermore, the valve cannot be re-used after modification to perform LVTs or LRTs since the bellows or springs are removed to install the adjustable stem. In other words, valve modification incapacitates valves for any other use. Maintaining an accurate stem position (d_x) may also be

challenging since the d_x is adjusted based on the number of turns of the precision screwed rod connected to the stem tip. Precision can be affected by the tolerance of the machined screw as well as the operation and manual adjustment of its position.

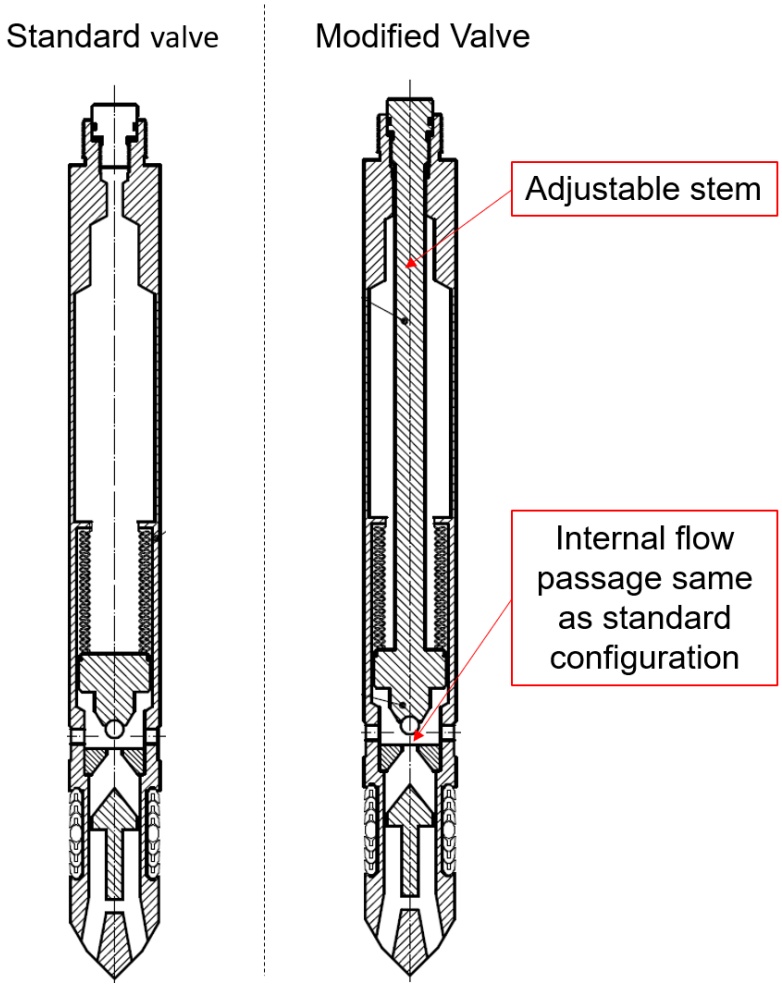

Figure 1.4. Representation of a modified injection pressure-operated valve (right) with a stem adjusted for a flow capacity test.

According to Decker (2014), the API recommended practice (API 19G2 et al., 2010) overpredicts the flow rate prediction with ports smaller than 12/64 inches by approximately 30%.

Moreover, for port sizes larger than 12/64 inches, the errors in valve performance determination can reach 50%. This accuracy level raises the importance of robust research methods and the optimization of current practices.

Considering the aforementioned issues related to FCTs, efforts to improve the capacity tests for GLVs are crucial to increase the efficiency of testing procedures and better manage the use of resources to perform the GLV tests. The use of computational techniques (e.g., numerical modeling) has already solved a distinct problem (Turzo & Takacs, 2009) and can also be used to evaluate GLV performance. Methods such as the computational fluid dynamics (CFD) model have been employed to address problems in many different industries, such as oil and gas, aviation, chemical, environmental, urban planning, and biomedical (Buchan et al., 2020; Meriem-Benziane et al., 2020; Sami & Turzo, 2020; Trindade et al., 2021). Specifically, the CFD facilitates the replication of complex flow domains and flow simulation using the conservation equations that govern the flow field.

Besides CFD, one-dimensional (1D) models are also commonly employed to solve engineering problems. 1D models are generally less complex than CFD models; however, 1D models usually do not resolve the systems but employs correlations, physical equations, and empirical considerations to reduce the system's complexity. For instance, 1D models can simulate flow while considering the main equivalent areas open to flux with an accuracy that meets the requirements of many engineering problems (Azim, 2019; Ruiz et al., 2014). Some advantages of 1D steady-state flow models include their simplicity for creating and running simulations as well as their shorter simulation times.

Both CFD and the 1D steady-state models can be used as potential solutions for performing FCTs. A validated simulation methodology could reduce the number of tests or even avoid the

requirement of a modified valve. In light of the unfavorable aspects of current FCT practices, the present study aims to develop and validate a methodology based on computational fluid dynamics and a 1D steady-state model to numerically perform the flow capacity evaluation of GLVs.

1.2. Objectives

The main goal of this study was to develop and evaluate the efficacy of a steady-state 1D model and a CFD model to perform the flow capacity evaluation of IPO GLVs and predict C_v and R_{cp} for distinct stem positions. To achieve the main objective, the following goals were set:

- Gather available benchmark data from experimental results and the VPC database. The data will be used to assess the performance of the models to predict critical variables such as flow rate, C_v, and R_{cp};
- Develop both a 1D mechanistic model and a CFD model with multiple IPO GLV configurations (e.g., different valve models and orifice sizes);
- Implement 3D CFD models for different IPO GLVs that include all of the internal features (e.g., inlet ports, internal orifice, check valve, and outlet ports);
- Assess the effectiveness of the modeling approaches by comparing the 1D and CFD model results against data from existing experiments and the VPC database.

Chapter 2. Literature Review

The first section of this chapter includes a description of the three different experimental procedures employed for the determination of GLV performance. The following section presents a brief review of the literature and current practices related to determining GLV performance using both experimental and computational methods.

2.1. Gas Lift Valve Performance Determination: Testing Description

Two methods are generally available for creating GLV performance curves:

1- Experimental dynamic flow testing for pressure and temperature at field-level conditions (API 11V2, 2001; API 19G2 et al., 2010; Decker, 1993b).

2- Theoretical correlations (Altarabulsi, 2018).

Since testing a valve at field-level high-pressure conditions may not be feasible, most GL designs rely on theoretical correlations to determine the performance curve of a valve under various conditions. Some of these theoretical correlations include the VPC correlation, Thornhill-Craver equation (Cook & Dotterweich, 1946; Bertovic et al., 1997), and API Simplified correlation (API 19G2 et al., 2010).

The API recommended practice provides procedures for GLV performance tests and correlation development. Therefore, a combination of three experimental procedures facilitates the determination of necessary parameters for correlation development and the further calculation of performance curves for valves at field-level conditions (API 11V2, 2001; API 19G2 et al., 2010; Decker, 1993b). These tests include the LRT, LVT, and FCT. This thesis primarily focuses on the FCT to determine the flow coefficient (C_v) and critical pressure ratio (R_{cp}) as a function of stem

travel. Both C_v and R_{cp} are important parameters employed in the VPC correlation to determine performance curves. The following is a brief description of the three experimental procedures performed to determine GLV performance.

Load Rate Test*:* This test is conducted to determine the spring load rate and maximum effective stem travel. The test station is designed to apply pressure on the full area of the bellows and then measure the stem displacement as a function of pressure. The API 19G2 suggests using nitrogen, air, helium, or another compressed gas for these tests (API 19G2 et al., 2010). Plotting the stem travel versus the increase in pressure results in a nearly straight line, where the slope of the line is the load rate of the valve in psi/inches (Decker, 1993a). Stem displacement is directly measured using a linear variable displacement transducer (LVDT) that measures stem movement. Figure 2.1 presents a schematic of the test setup suggested by the API 19G2 for the LRT. This test can determine the mechanical behavior of a nitrogen-charged dome and bellows system. Figure 2.2 presents an example of the LRT results for an IPO GLV with a dome pressure of 800 psi. Additionally, the LRT also allows for the determination of the experimental R-ration, which is a function of the valve opening pressure (P_{voT}) and valve closing pressure (P_{vcT}) for a given temperature, as shown in Equation 2.1 (Decker 2014).

$$R = \frac{P_{voT} - P_{vcT}}{P_{voT}} \tag{2.1}$$

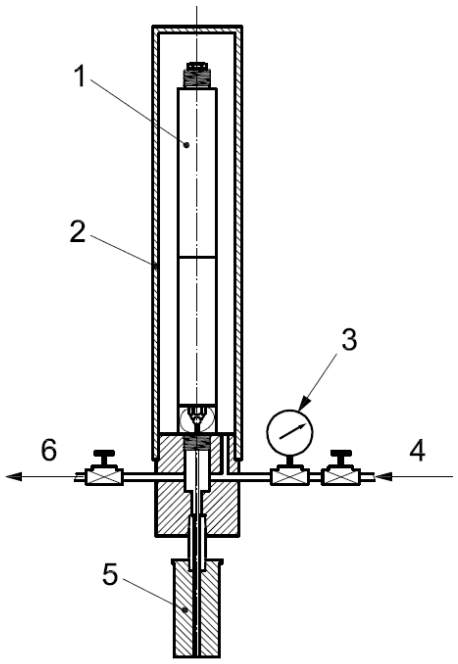

Figure 2.1. Schematics of the test setup for the load rate test. 1: gas lift valve; 2: tester; 3: upstream pressure gauge; 4: gas inlet; 5: linear variable displacement transducers; 6: bleed line. *Source*: API 19G2 et al. (2010).

Each dome pressure leads to different GLV load rates and the test is conducted at a few different dome pressures to determine the correlation between the load rate and dome pressure. Generally, plotting load rate against dome pressure also results in a nearly straight line. Both the slope of this line and a reference load rate at a specific dome pressure are parameters stored in the VPC database that enable the replication of the straight line and determine the load rates for other dome pressures.

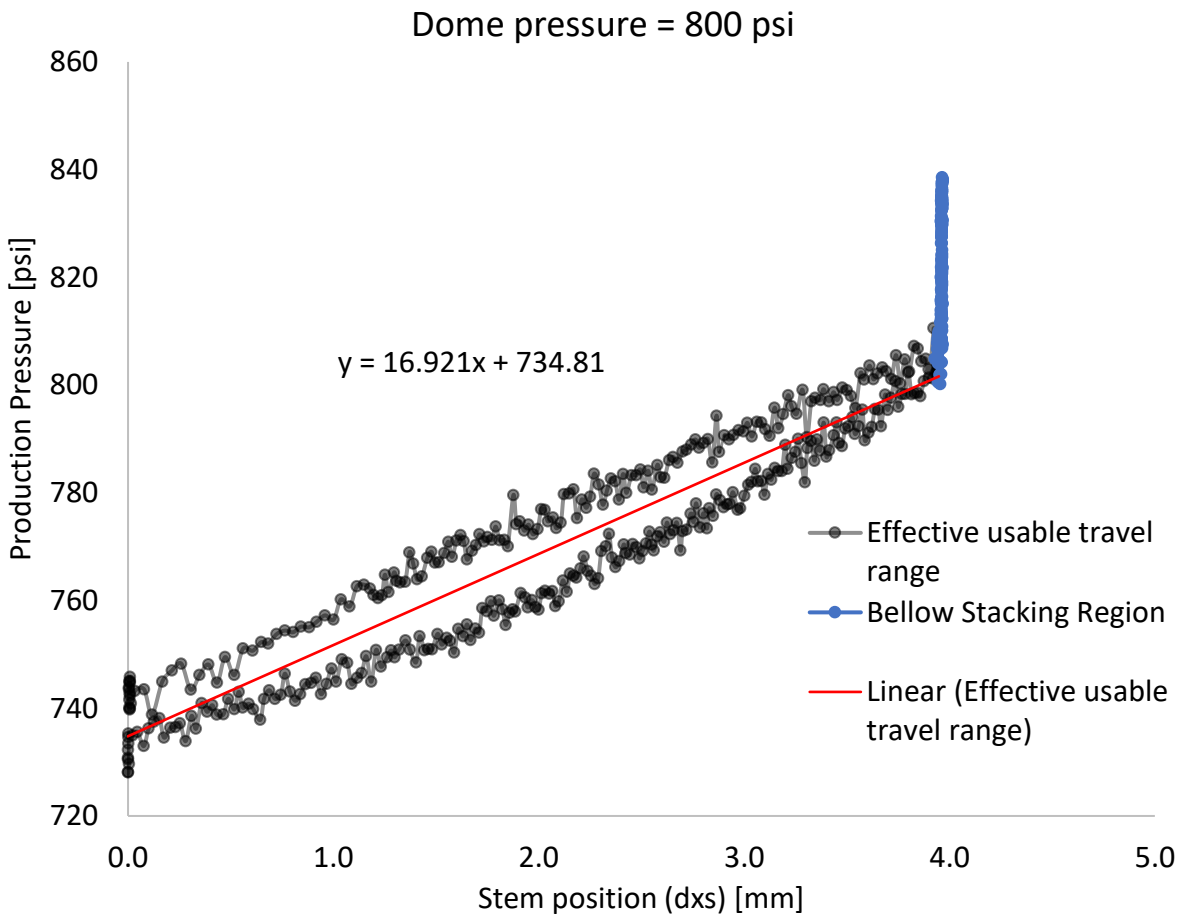

Figure 2.2. Example of pressure versus stem travel plot from an LRT. The slope of the straight line over the effective stem travel region gives the load rate for a specific dome pressure. The far-right region (in orange color) indicates the maximum stem travel and the bellows stacking region (i.e., non-usable stem travel).

Dynamic Test or Live Valve Test*:* This test is performed on a flow loop where the GLV is placed within a test pocket simulating the side-pocket mandrel. Figure 2.3 shows the flow loop used to indicate the test pocket and probe positions. This system can record the gas flow rate through the valve as well as the upstream pressure (P1), downstream pressure (P2), upstream temperature (T1), and downstream temperature (T2). To perform an LVT on an IPO valve, the upstream pressure is held constant while the downstream pressure is decreased, thereby creating a

larger gas flow rate across the GLV. This will cause the stem to move as the pressure changes, and the gas flow rate versus downstream pressure plot can be created for that pressure drop range. Notably, multiple tests run at different dome and upstream pressures are required to characterize GLVs.

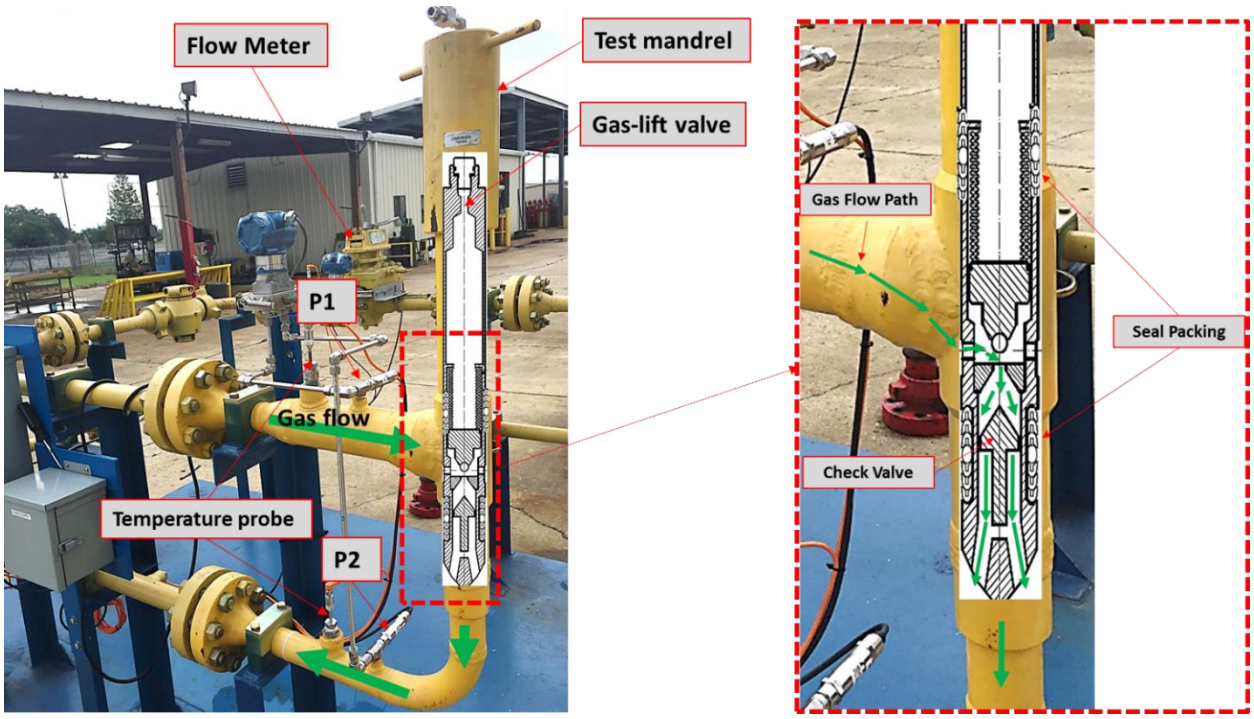

Figure 2.3. Valve Performance Clearinghouse flow loop with an indication of the test pocket and probe positions as well as details of the gas flow through the internal domain of the valve.

Flow Capacity Test: This test is performed to determine the valve flow coefficient (C_v) and the critical pressure ratio (R_{cp}) as a function of the stem displacement. The API recommends (API 11V2, 2001; API 19G2 et al., 2010) using a modified valve with an adjustable stem capable of being positioned at a fixed distance from the seat to perform the FCT. Generally, modification consists of replacing the internal bellows with a threaded rod that can position the stem during the

flow test (Decker, 1993a). A schematic of the modified GLV with an adjustable stem position is presented in Figure 1.4.

The modified valve is then placed in a test pocket capable of causing flow through the valve similar to that of the GL mandrels used in the field. Moreover, pressures and temperatures are recorded for the numerous differential pressures applied. Figure 2.4 presents the output of an FCT. Each run can provide a single point for the flow capacity (C_v) and critical pressure ratio (R_{cp}) for each stem position. More details regarding the three main tests used to evaluate GLV performance are provided in API 11V2 (2001), API 19G2 et al. (2010), and Decker (1993a).

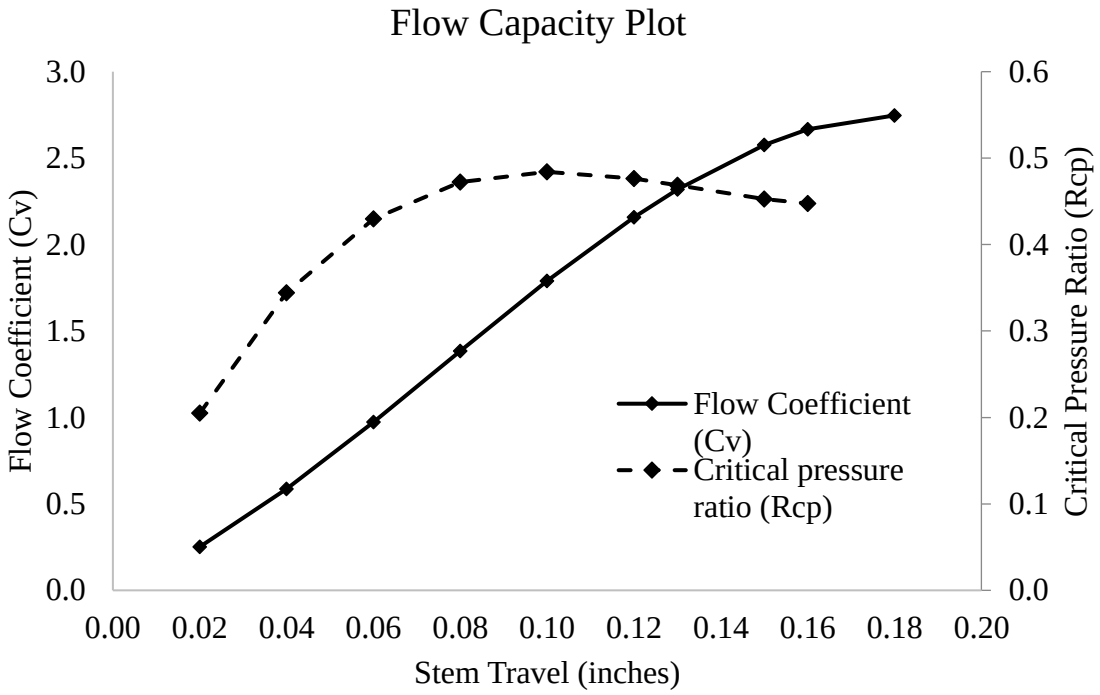

Figure 2.4. Flow coefficient versus stem travel: Example of result from the flow capacity test for an injection pressure-operated gas lift valve.

2.2. Models Developed to Estimate Gas Lift Valve Performance

The current standard for characterizing GLV performance is the Recommended Practice for Gas Lift Valve Performance Testing (API 11V2, 2001). This API document includes recommended practices and details for GLV tests. The API compiles a series of procedures that combine experimental methods and data processing guidelines to estimate GLV flow performance.

One of the main methods to used determine GLV performance was developed and described in Decker (1993b). The author presents a method for analyzing data on GLV performance that explores the ability to estimate the dynamic stem position under flowing conditions. Decker's work describes the LRT, FCT, and LVT, as presented in Section 2.1. The correlation for performance calculation is also presented in Decker (1993b). According to Decker, the data analysis method applies to any pressure-operated GLV and yields predictions within ±10% of the actual flow rate. Results indicate that the statistical accuracy of the correlation may be standard at approximately ±20%.

The work described by Decker (1993b) established the VPC project, which follows test and data processing procedures similar to those described by API recommended practices for GLV performance testing (API 11V2, 2001). The VPC project aims to continuously test GLVs from different manufacturers, models, and configurations to provide operators and service companies with access to accurate performance curves for as many valves as possible. After the valves are tested in a laboratory setup, a database with a list of numerical coefficients is stored and used to reproduce the experimental performance curve for each GLV in the database with an accuracy of approximately ±20%, as described in Decker (1993b). Louisiana State University is currently the administrator of the VPC project and responsible for conducting GLV performance tests, updating the VPC database, and further developing and improving the VPC model.

Hepguler (1988) developed a model similar to the approach of Decker (1986). In Hepguler's model, a dynamic force balance equation is used to calculate the stem position. The difference in this model is that the effective pressure is obtained by measuring the effective pressure and force acting on the ball. Figure 2.5 provides a schematic of the load test setup with the load cell attached to the stem. To determine the discharge coefficient, the product YC_d is determined from experiments that measure the pressure in the interior of the valve. To obtain the load rate, Hepguler suggests an apparatus to measure the dome's internal pressure. Results from the application of this method accurately describe the valve performance and also reduce the volume of data required (Hepguler et al., 1993). However, due to the complexity of the measurements required to calibrate this model, Hepguler's approach is considered highly impractical (Hérnandez, 2016). The methodology presented in this thesis can also model separated components and consider the effects of pressure drops at the check valve and orifice on the overall performance of the valve. However, the 1D mechanistic model used to computationally determine the pressure drop at each component considerably reduces the complexity of the procedure and eliminates the need to experimentally measure internal flowing pressures.

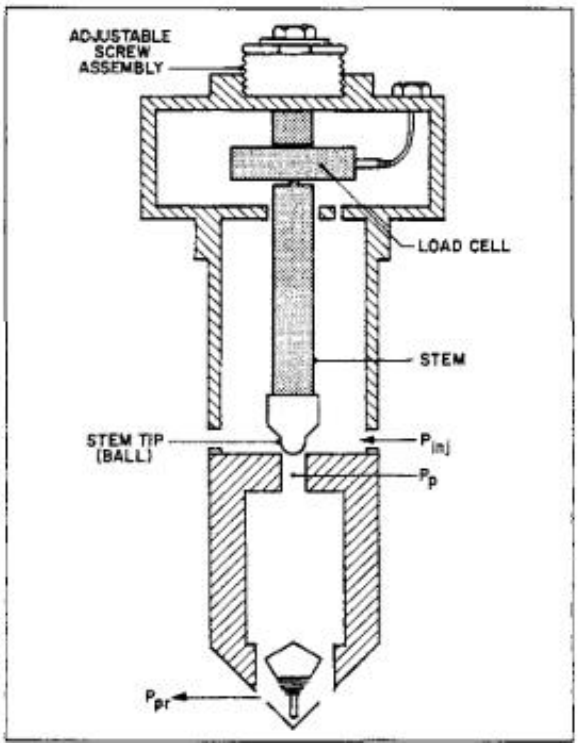

Figure 2.5. Schematics of the valve used in the effective load test (Hepguler et al., 1993).

Sagar (1991) also presented a mechanistic model that follows a similar approach to those of Decker and Hepguler. In Sagar's model, the effective pressure on the stem ball is obtained using the 1D compressible flow theory. One important assumption of this model is that the space between the ball and the seat is considered a converging-diverging nozzle. This model considers the flow area along the valve as a function of the stem travel and disregards the actual shape of the flow path. The stem travel is determined by the force balance equation based on the effective pressure on the ball. Although this model employs a physics-based approach, the actual complexity of the flow passage around the ball and seat may not be entirely captured by the assumption of the converging-diverging nozzle (Hérnandez, 2016). Similarly, the 1D model approach presented in

this thesis treats the area around the ball and seat for each stem position as well as the area of the check valve as a single equivalent circular flow area.

Bertovic (1995) developed a model capable of predicting gas flow for the entire range of GLV flow modes (orifice, throttling, and transitional flow) using only one set of equations. This type of model is also referred to as a unified model. Moreover, this model uses the orifice flow equation for the flow across the seat as well as a modified orifice flow equation to determine gas flow through the ball seat area. With these two equations, it is possible to determine the intermediate pressure between the minimum ball seat area and the seat. The flow rate is obtained by applying this intermediate pressure to any of the two equations. Although this model only requires six coefficients, the determination of these coefficients requires an extensive dynamic test, which makes this method relatively difficult (Hérnandez, 2016).

Another model used to determine the flow performance of nitrogen-charged GLVs was presented by Faustinelli and Doty (2001). The work of Faustinelli and Doty (2001) employed physical principles of flow mechanics and divided the GLV into four regions, as shown in Figure 2.6. Each of these four regions is characterized by pressure, temperature, and equivalent flow area. This model includes the prediction of isentropic processes from the upstream condition to the minimum flow area as well as the determination of pressure recovery due to a sudden gas expansion beyond the minimum flow area. Notably, Faustinelli and Doty (2001) stated that previous models did not accounted for the pressure recovery effect. Results from the modeling application show an increased accuracy with as low as 5.1% error when compared to experimental flow rate results for the JR-STDN 1-inch IPO gas lift valve. The highest error encountered within the benchmark was 28.04%. Although Faustinelli and Doty (2001) work only validates the methodology for up to 700 psi, the results highlight the promising potential of using mechanistic-

based models for GLV performance evaluation. Notably, the model better represents the physics of the compressible gas flow phenomena on GLVs compared to previous models.

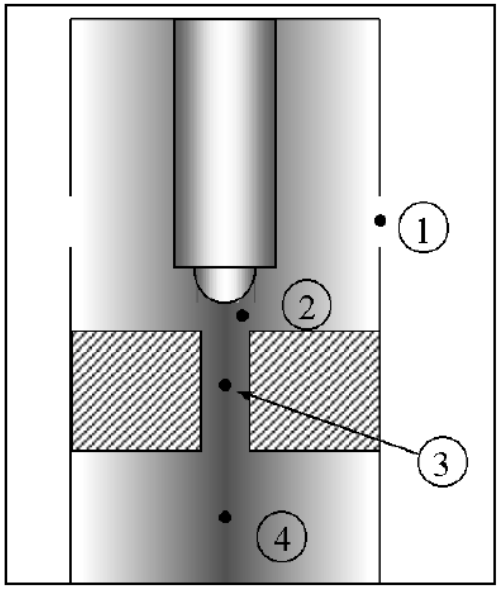

Figure 2.6. Schematics of the gas lift valve and four regions considered in Faustinelli and Doty's (2001) method to predict valve flow performance. 1) injection or inlet; 2) ball seat zone; 3) orifice or valve port; 4) production or outlet. *Source:* (Faustinelli & Doty, 2001)

Besides the physical models and experimental procedures, exploring alternative methods to model the performance curve of GLVs have shown some potential to either improve the method proposed by Decker (1993b) or minimize the number of tests required to accurately provide a correlation for a GLV performance curve, particularly for IPO valves. For instance, the study of Turzo and Takacs (2009) has shown the potential for using computational methods to determine the performance of GLVs. Turzo and Takacs (2009) presented a study that used CFD to determine the performance behavior of one specific GLV model. The authors developed an iterative procedure to describe the valve stem travel as a function of the net opening force by integrating

the pressure distribution on the valve stem tip. Notably, the results of the modeling procedure were compared against experimental data and showed a reasonable match. Additional simulations considering different valve models and flow ranges could increase the credibility of the CFD approach to characterizing GLVs.

CFD methods also facilitate the investigation of specific design modifications to optimize GLV performance. For instance, Elldakli (2015) evaluated the possibility of enhancing the flow performance of GLVs with a sharp-edged seat by using larger ball sizes. The work of Elldakli (2015) applied CFD to investigate the effect of using larger ball sizes than those conventionally used. For each port size/type, different ball sizes were tested at different stem positions under the same injection pressure and temperature. Figure 2.7 presents a schematic of the changes in ball size and a plot with the results of flow rate versus stem travel for various ball sizes. Among the results obtained from benchmark valve testing, an increasing trend in flow rate under the same stem travel was observed as the ball size increased. Elldakli's (2015) work not only confirms the promising potential of using modeling techniques to predict valve performance but also provides insights into using this methodology to suggest design optimizations for optimizing flow performance.

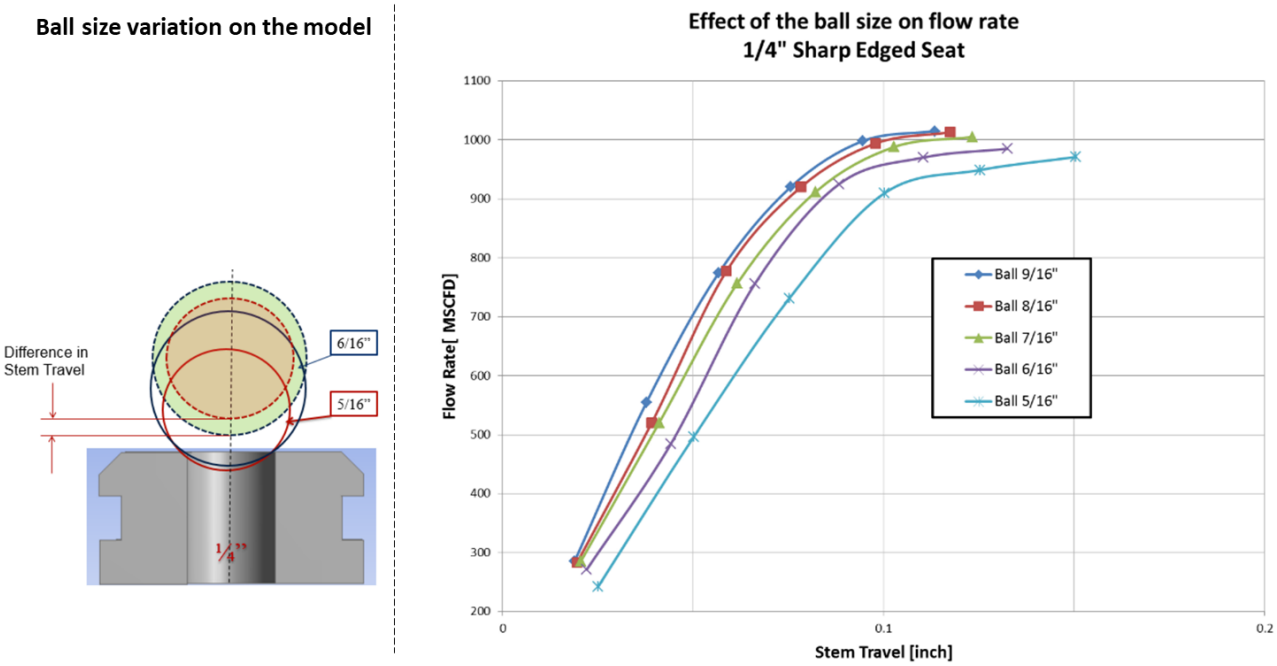

Figure 2.7. Schematics of ball size variation for the same port size and the results of flow rate versus stem travel for various ball sizes. *Source*: Elldakli (2015).

Elldakli and Soliman (2017) also used CFD to study the effect of minor geometric changes in stem and orifice shape on the performance of GLVs. These authors simulated flow through IPO GLVs with different orifice shapes. This simulation methodology facilitated the investigation of numerous designs without the need for machining and experimentally flow testing different valve geometries. The optimum design for each port was compared within the initial modified design (beveled seat) and a sharp-edged seat. Notably, the results show a significant improvement with the optimized design over the original design.

Kabir et al. (2020) recently published a CFD study to evaluate and optimize ball and seat shapes for GLV performance improvement. This work consisted of an experimental and numerical simulation approach that aimed to improve the design aspects of the valve for better performance. This study concluded that different seat and ball shapes change the open flow between the seat and

stem tip, which directly impacts the flow performance of the valve. Figure 2.8 presents the effect of such geometric changes on the open space between the seat and stem tip. This study also highlights the flexibility of applying numerical simulation methods for both performance assessment and the evaluation of GLV design features.

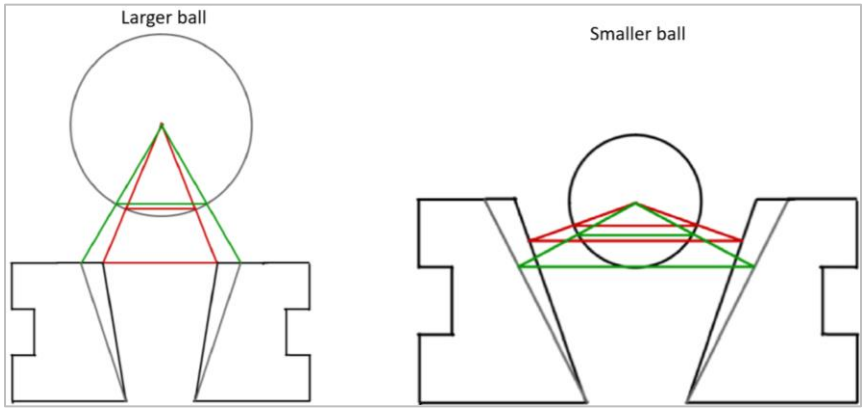

Figure 2.8. Effect of port diameter on the flow area changes for larger and smaller ball sizes and different seat geometries (Kabir et al., 2020).

The development of methodologies capable of characterizing GLV flow performance is highly important to accurately design GL applications. However, the complexity of the high-pressure compressible gas flow phenomena through the valve increases the challenge of obtaining a reliable and effective performance evaluation method. Methods such as those of Sagar (1991), Hepguler (1988), and Faustinelli and Doty (2001) have shown relatively accurate flow performance results and highlight the potential for considering the internal flow areas at restrictions using a physics-based approach. On the other hand, the experimental procedures involved in these methods are complex and require valve modifications to obtain pressure measurements at internal valve positions. The complexities of these experimental procedures and

their data processing make these methodologies impractical for application on multiple GLVs on a regular basis. The API recommended practices (API 11V2, 2001) and methodology described by Decker (1993a) are relatively less complex when compared to the methods of Faustinelli and Doty (2001), Hepguler (1988), and Sagar (1991). However, although largely employed for valve performance characterization, Decker (1993) method still requires extensive test runs, a modified GLV for the FCT, and complex data processing for correlation development, which also makes this method time consuming.

Using a computational method to characterize valve performance—as demonstrated by Elldakli (2015) and Turzo and Takacs (2009)—has the potential to reduce the number of experiments required to determine GLV flow behavior as well as the time required to obtain results. As demonstrated by Kabir et al. (2020), the use of computational models facilitates the evaluation of distinct control domain geometries and the impact on flow behavior. Regarding the determination of geometric dependent flow characteristics (e.g., C_v and R_{cp}), the use of computational models eliminates the need to modify a GLV to perform dynamic flow tests at fixed stem positions.

Chapter 3. Methodology

The primary objective of this study was to model GLV flow performance using the concept of flow coefficient (C_v) and critical pressure ratio (R_{cp}), as presented in the literature review chapter. However, previous studies have proposed the experimental determination of C_v and R_{cp} via several tests. Notably, the present study proposes the use of 1D model and three-dimensional (3D) model based on CFD simulations validated with only a few experimental tests to obtain C_v and R_{cp}.

This chapter describes the methods used to obtain the flow coefficient and critical pressure ratio from these 1D model and 3D CFD numerical model simulations. Firstly, the VPC database deployed to validate the models is presented. Following the database description, both the 1D and 3D CFD models are presented alongside the fundamental equations and assumptions behind these models.

3.1. Valve Performance Clearinghouse Database

This study utilizes the VPC database to validate the 1D mechanistic model and the 3D CFD model. The VPC database was created based on GLV flow tests for hundreds of valves from several manufacturers with different valve models and configurations. The VPC database contains a lookup table with numerical coefficients adjusted from the experimental tests for each valve. These coefficients can be used in the VPC correlation to calculate the flow performance curve for all valves in the database, with accuracy within ±10 % (Decker, 1993). The valves in the VPC database were typically flow tested at pressures between 800 and 2,000 psi and at temperatures no higher than 100°F.

The VPC database has gathered information for over 230 different GLV configurations, including orifice valves, IPO valves, PPO valves, and different port sizes for the same valve models. The VPC correlation employs a mechanistic model that utilizes a force balance equation to calculate the flow rate under dynamic stem positions (Decker, 2014). Nevertheless, the VPC correlation is only valid for constant flow gas flow rates, injection, and downstream pressure to the valve.

The performance tests described by Decker (1993) provide the parameters and correlation coefficients for each GLV. Equation 3.1 calculates the flow rate at a specific injection pressure (P_{cf}) and specific fluid properties. To obtain the flow rate, valve parameters such as the test-rack opening pressure (P_{TRO}), load rate (LR), maximum effective stem travel ($d_{x\,max}$), flow coefficient (C_v), and pressure ratio (R_p) as a function of stem travel (d_x) are required. The expansion factor (Y) can be written as a function of the critical pressure ratio R_{cp}. Equations 3.2 to 3.5 present the expressions for expansion factor, flow coefficient, critical pressure ratio, and pressure ratio (Decker, 1993).

$$Mscfd = 32.64 * C_v * Y * \left(P'_{cf} + 14.7\right) * \sqrt{\frac{R_p}{SG * R * Z * T}} \quad 3.1$$

$$Y = 1 - \frac{R_p}{\left(3 \times R_{cp} \times k\right)} \quad 3.2$$

$$C_v = a * d_{xc}^2 + b * d_{xc} + c \quad 3.3$$

$$R_{cp} = c * d_{xc}^2 + d * d_{xc} + c \quad 3.4$$

$$R_p = \frac{(P_1 - P_2)}{(P_1 + 14.7)} \quad 3.5$$

The flow coefficient (C_v) and critical pressure ratio (R_{cp}) are functions of the stem travel (d_x). For this reason, flow rate calculations require the values of C_v and R_{cp} for each stem position while considering the movement of the GLV stem. As described in API 11V2 (2001), the FCT facilitates the determination of $C_v$and R_{cp} for multiple stem. Notably, the FCT requires the use of a modified GLV with an adjustable stem.

Therefore, data from the FCT facilitates the development of an empirical correlation of C_v and R_{cp} as a function of stem position for the entire range of stem travel (d_x). The d_x ranges from a closed position (flow area is zero) to a maximum open valve (flow area equals the orifice area). Equations 3.6 and 3.7 show the correlation format for C_v and X_t, which is a third-order polynomial equation. Through the C_v versus d_{xs} and R_{cp} versus d_{xs} curves from the FCT, one can obtain the correlation coefficients $C_{vA}, C_{vB}, C_{vC}, and\ C_{vD}$ for C_v and $R_{cpA}, R_{cpB}, R_{cpC}, and\ R_{cpD}$ for R_{cp}.

$$C_v = C_{vA} \times d_{xs}^3 + C_{vA} \times d_{xs}^2 + C_{vA} \times d_{xs} + C_{vA} \tag{3.6}$$

$$R_{cp} = R_{cpA} \times d_{xs}^3 + R_{cpB} \times d_{xs}^2 + R_{cpC} \times d_{xs} + R_{cpD} \tag{3.7}$$

This thesis proposes using data from numerical simulation to obtain C_v and R_{cp}. Validation of this new concept can be done by using the C_v and R_{cp} values from previously tested valves in the VPC database. The VPC database is a source of correlation coefficients for multiple GLVs that enables the calculation of C_v and R_{cp}. Therefore, C_v and R_{cp} are calculated for multiple stem positions using Equations 3.6 and 3.7.. In the present study, graphs of C_v and R_{cp} as a function of stem travel were generated for 12 different IPO GLVs to provide sufficient data to compare to results from the 1D model and 3D CFD simulation.

Sections 3.2 and 3.3 present a description of the 1D model and 3D CFD models used to obtain the simulated C_v and R_{cp} values for 12 GLVs included in the VPC database. Then, the simulated results from the 1D and 3D CFD models were validated with data from the VPC database.

3.2. One-dimensional Model Description

In simple terms, a GLV can be understood as a set of restrictions that control the amount of gas flowing through a valve for a given pressure differential in the valve. The valve orifice (or port size) acts as a major flow restriction (or choke) since the orifice port size is considerably smaller than the inlet and outlet equivalent diameters, especially for valves with smaller orifice sizes (e.g., 8/64, 12/64, and 16/64 inches). Theoretically, a choke (shown schematically in Figure 3.1) is a device that controls the flow rate by restricting flow. Compressible fluids flowing through a constriction can accelerate enough to reach sonic velocity at a certain differential pressure between upstream and downstream the orifice. Generally, the sonic flow condition is referred to as critical flow, while the subsonic condition is known as subcritical flow. This behavior also occurs in GLVs, and this similarity facilitates the modeling of gas flow through a GLV using critical and subcritical flow correlations.

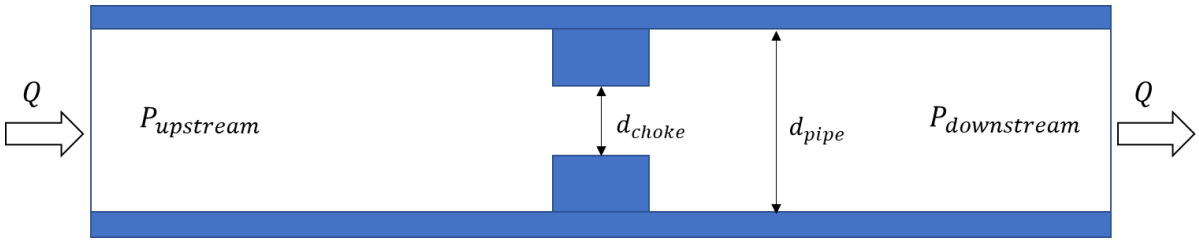

Figure 3.1. Schematic of a pipe flow restriction (or choke), where d_{ch} represents the diameter of the choke and d_l is the internal diameter of the upstream and downstream flow lines.

There are multiple correlations to compute the flow rate through a choke-like fixture. Some of these empirical correlations stem from the studies of Ashford and Pierce (1975), Sachdeva et al. (1963), API14B, Omana et al. (1969), and the mechanistic model (or semi-empirical correlations).

Depending on whether the flow is subcritical or critical, additional equations are necessary to calculate the pressure drop across the restriction. Sections 3.1.1 and 3.1.2 present the pressure drop formulas for both the critical and subcritical flow conditions employed in the mechanistic model used in this study.

3.2.1. ΔP Estimation for Subcritical Flow

This study used a mechanistic model to calculate gas flow through different GLV restrictions. The model was implemented using the commercial software PIPESIM (2018). For a complete description of the model, the references cited in the software's documentation should be consulted (Brill & Beggs, 1991). For the case of subcritical flow, the total pressure drop across the choke is derived from Bernoulli's equation, as presented in Equation 3.8. For single-phase gas flow, the total pressure drop comes from the gas phase since no liquid is involved.

$$\Delta p_G = \frac{\rho_G v^2}{2c} \frac{1}{(C_D Y)^2} \tag{3.8}$$

where v is the gas flow velocity through the orifice, A_{bean} is the orifice area, c is the conversion factor for engineering units $\left(c = 144\, g \frac{lb}{ft \cdot s^2} \frac{1}{psi}\right)$, C_D is the discharge coefficient, and Y is the expansion factor and accounts for the effect of gas compressibility, as described by Equation 3.9 (Brill & Beggs, 1991).

$$Y = 1 - \frac{0.41 + 0.35\delta^4}{\gamma}\frac{\Delta P}{P_{up}} \quad 3.9$$

where γ is the specific heat ratio, which is the ratio of the specific heat at constant pressure c_P to the specific heat at constant volume c_V. This variable is also referred to as heat capacity ratio, isentropic expansion factor, or the adiabatic index. For diatomic gases such as the nitrogen gas used in this work, the specific heat ratio is 1.4. The flow coefficient C_v can be calculated as a function of the discharge coefficient (C_D), as shown in Equation 3.9.

$$C_v = \frac{C_D}{\sqrt{1 - \delta^4}} \quad 3.10$$

$$\delta = \frac{d_{bean}}{d_1} \quad 3.11$$

The gas flow rate (q_G) through the restriction can be obtained by inverting Equation 3.8.

$$q_G = A_{bean}\sqrt{\frac{2g\rho_g\Delta P}{\left[\frac{c}{(C_D Y)^2}\right]}} \quad 3.12$$

The flow area of the restriction is represented by A_{bean} ($A_{bean} = {}^{\pi d_{bean}^2}/_4$) with an equivalent circular diameter d_{bean}.

3.2.2. ΔP Estimation for Critical Flow Correlation

Regarding critical flow through a GLV, pressure drop is a function of the critical pressure ratio (R_{cp}) and upstream pressure (P_{up}). As previously mentioned, the critical pressure ratio determines the downstream pressure at which the flow reaches sonic velocity. R_{cp} indicates the point where a further decrease in downstream pressure no longer affects the flow rate.

For single-phase gas flow, the critical pressure ratio is a function of the specific heat ratio $\left(\gamma = \frac{C_P}{C_V}\right)$. In the case of diatomic gases, the specific heat ratio assumes values of $\gamma = 1.4$ and $R_{cp} = 0.53$. Equation 3.13 describes the formula for pressure drop under critical flow conditions, where the R_{cp} is defined as Equation 1.4 (API Recommended Practice 520; Potter & Wiggert, 2010).

$$\Delta P = \left(1 - R_{cp}\right) P_{up} \tag{3.13}$$

3.2.3. Solver and Modeling Approach

The governing equations for calculating the flow rate as a function of the pressure drop through an orifice are relatively simple and commercial software packages (OLGA., n.d.; PIPESIM, 2018) implement the mechanistic model described in Sections 3.21 and 3.2.2. For the present study, the commercial software PIPESIM (PIPESIM, 2018) was employed to calculate the flow rate for a given set of operating conditions, such as different GLV configurations, port sizes, stem positions, fluid types, upstream and downstream pressures, and fluid temperatures. One of the advantages of this simulator is its intuitive interface, ability to customize a model according to its corresponding set of restrictions, and built-in PVT modeling and plotting capabilities. For instance, values such as equivalent diameter, discharge coefficient, fluid heat capacity ratio (c_p/c_v), and flow coefficient can be modified for each GLV.

Figure 3.2 presents a screenshot of the choke properties window from PIPESIM to show the variables that can be customized in this software. The variables and assumptions considered for this model are described in Table 3.1 (PIPESIM, 2018).

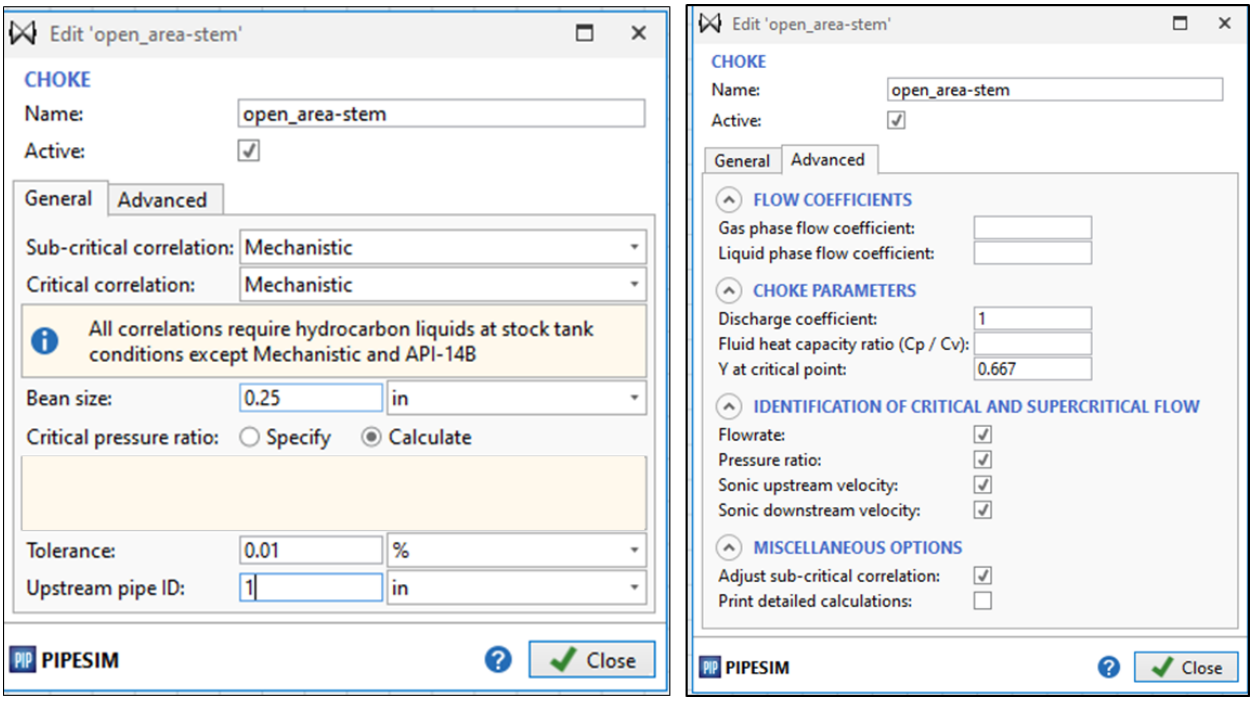

Figure 3.2. Choke configuration window in the PIPESIM simulator with parameters considered in the 1D model for GLV.

Table 3.1. Description of the properties available the chole configuration window in PIPESIM for the 1D mode for GLV.

General	
Subcritical correlation	Correlation from the list. This work is set to mechanistic, which uses the equations described in Section 3.2.1.
Critical correlation	Correlation from the list. This work is set to mechanistic, which uses the equations described in Section 3.2.2 to define pressure drop.
Bean size	Equivalent circular diameter of the available flow area of the restriction. In the present work, this variable is used to calibrate the model.
Critical pressure ratio	Used to determine the downstream pressure when critical flow occurs in the choke. The calculations are performed using the Ashford-Pierce method (Ashford and Pierce, 1975): $$\frac{dq}{d\varepsilon} = 0 \; at \; \varepsilon = R_{cp}$$

(table cont'd)

General	
Tolerance	Percentage tolerance for the identification of critical flow conditions.
Upstream pipe ID	Inside diameter of the pipe upstream of the choke.
Advanced choke options	
Flow coefficients	
Gas phase flow coefficient	Flow coefficient for the gas phase.
Liquid phase flow coefficient	Not considered in this work.
Choke parameters	
Discharge coefficient	Used to calculate the flow coefficients. In the present work, this variable is used to calibrate the model. The range of discharge coefficients available in PIPESIM ranges from 0 to 5. For this work, a typical range of values used in the calibration of the model is 0.4 to 1.
Fluid heat capacity ratio (C_p/C_v)	The valid range is 0.7 to 2. Typically, it is 1.26 for natural gas and 1.4 for a diatomic gas.
Y at the critical point	Gas expansion factor at critical flow. The valid range is 0.5 to 1. This is used to modify the pressure drop equation to allow for gas compressibility. In this work, Y is set at 0.663 (Decker, 1993b).
Identification of critical and supercritical flow	
Flow rate	Flow rate to identify the critical flow. Default option.
Pressure ratio	Pressure ratio to identify the critical flow. Default option.
Sonic upstream velocity	Identifies critical flow if sonic velocity is observed upstream of the restriction. Default option.
Sonic downstream velocity	Identifies critical flow if sonic velocity is observed downstream of the restriction. Default option.
Miscellaneous options	
Adjust subcritical correlation	Adjusts subcritical correlation to match the flow rate predicted by critical correlation. Default option.

The classical models of the Thornhill-Craver equation (Cook & Dotterweich, 1981) and Decker (1993) do not include separate calculations for the different restrictions in the flow path

within the GLV. The aforementioned models treat the flow coefficients and critical pressure ratio for all restrictions within the GLV combined as one. However, other models have attempted to model the separate components of the GLV. For instance, the studies of Hepguler (1988), Sagar (1991), Bertovic (1995), and Faustinelli (1997) have considered some of the internal components of the GLV, such as the orifice port, and check valve as well as flow expansion between the orifice port and the larger diameter part of the valve (see Figure 1.2).

The 1D model used in this study considers the main equivalent diameters of each restriction and calculates gas flow based on the pressure drop across each restriction. In other words, the input parameters for the model are the fluid properties, inlet pressure, outlet pressure, and the equivalent diameters of internal restrictions. For valve models/configurations in which the inlet port and outlet port areas of the valve are considerably larger than the orifice and the check valve area, the model neglects the inlet and outlet port as restrictions. In these cases, the 1D model used in this study only accounts for the open area between the valve stem and the orifice as well as the open flow area of the check valve. Figure 3.3 shows a representation of the GLV model considered for the PIPESIM simulation. Figure 3.3a contains all of the internal restrictions of the GLV, while Figure 3.3b presents the simplified model with only the restrictions at the orifice and the check valve.

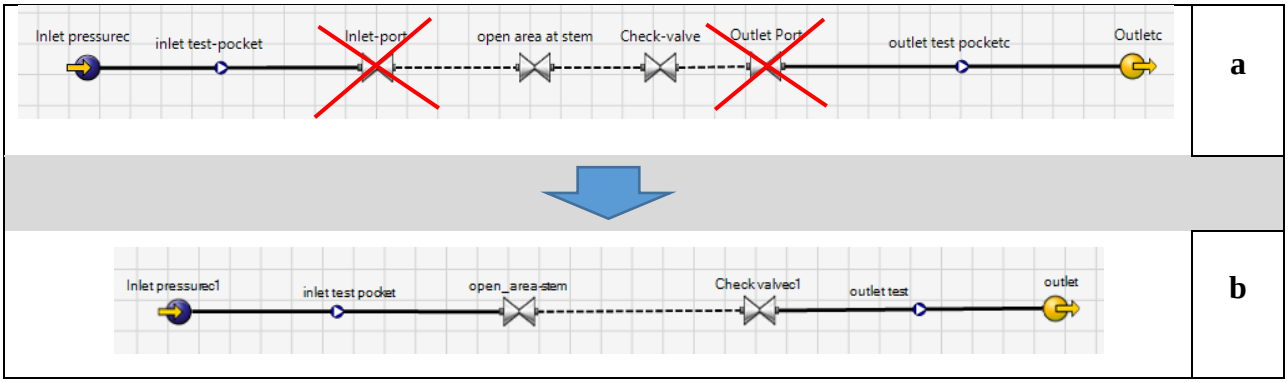

Figure 3.3. 1D steady-state model for the IPO gas lift valve. Each Venturi shape indicates a restriction within the flow domain. a) 1D model including most of the internal restrictions present

in a gas lift valve; b) simplified 1D model with only two main restrictions: the area between the orifice and stem tip and the area at the check valve.

Figure 3.4 presents a schematic of the frustum that represents the open flow area between the stem and the orifice. The revolution of the triangle connecting the two points at the orifice edge to the center of the sphere or stem tip shapes the conic area. The input for the mechanistic model implemented in PIPESIM is a circular equivalent diameter ($D_{eq} = 4 \cdot A_{bean}/\pi$) calculated using the frustum area. Furthermore, the flow area changes as the stem moves up and down. When the frustum area is equal to or larger than the orifice area itself, the opening achieves the maximum flow area. Elldakli (2015) and Shahri (2011) used a similar approach to determine the flow area between the orifice and the stem tip. Regarding the check valve, the equivalent circular diameter is calculated using the total open flow area. However, unlike the frustum, the equivalent diameter at the check valve did not change since this element remained fully open for all simulations in this study and functions as long as there is flow through the valve (e.g., if the pressure upstream is higher than downstream).

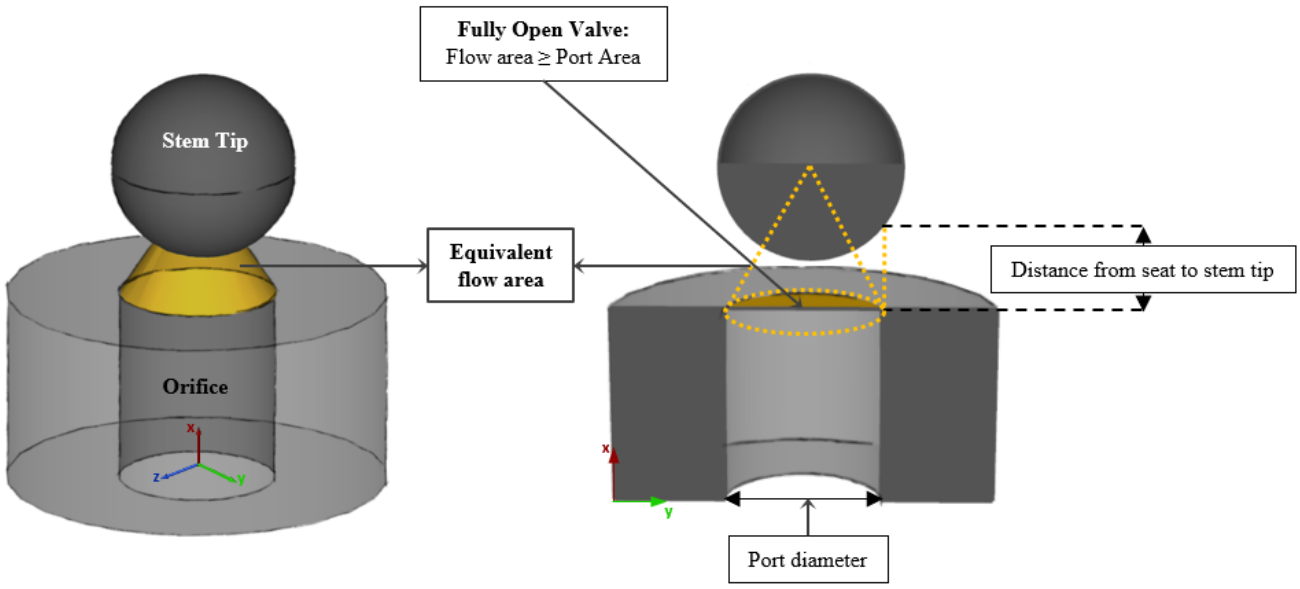

Figure 3.4. Schematics of the equivalent conical flow area used as input for the 1D model of gas flow through the gas lift valve.

3.2.4. Flow Capacity Simulations Using the One-dimensional Model

To replicate the FCT using the 1D mechanistic model, the present study followed a procedure based on the API 11V2 (2001) and API Spec 19G2 (2010) documents. The primary goal of the FCT is to characterize the GLV and determine the flow coefficient C_v and critical pressure ratio R_{cp} for each stem position. The 1D modeling approach based on the mechanistic model uses information from the GLV flow tests to calibrate the C_v and R_{cp} values for the 1D mechanistic model of maximum stem displacement. With the calibrated C_v and R_{cp} for the maximum stem position, it is possible to determine the flow rate for different stem positions without additional tests; however, this is only possible when using the calibrated 1D mechanistic model. Figure 3.5 presents a workflow that explains the steps taken to conduct the FCT using the 1D mechanistic model.

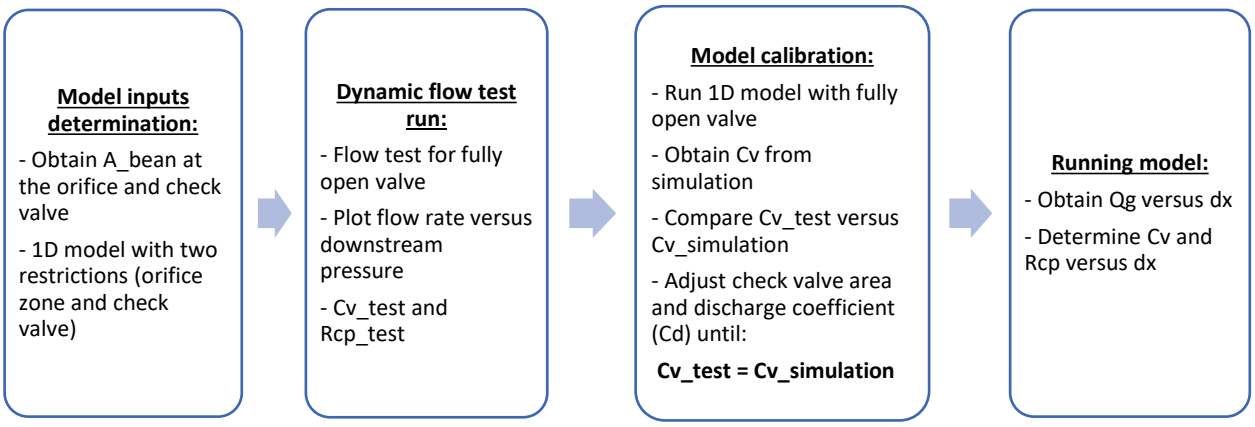

Figure 3.5. Workflow for flow capacity determination using the 1D mechanistic model approach.

1. Model inputs determination: The first step involved defining the model input parameters. The mechanistic model requires information about fluid properties, the equivalent diameter corresponding to each stem position, temperature, and pressure ranges for the simulation. Table 3.2 presents an example of the geometric information around the stem of a 20/64-inch GLV. Since the flow area only depends on the diameter of the port and the ball, the equivalent diameter is the same for both 1-inch and 1.5-inch outside diameter valves. Each stem position, from zero to the maximum opening, has corresponding information for the open flow area between the stem and the orifice. Moreover, the equivalent diameter for this area (considering a circular shape) is calculated and also serves as an input for the model. The valve achieves its maximum opening when the equivalent diameter equals the orifice diameter. As shown in Figure 3.3, the 1D model only considers two restrictions.

Table 3.2. Example of the geometric parameters considered for a 20/64-inch injection pressure-operated gas lift valve, where D_{eq} represents the equivalent circular diameter of the open flow area between the ball and port for each fixed stem position d_{xs}.

Open area (inches^2)	D_{eq} (inches)	d_{xs} (inches)
0.00	0.00	0.0
0.01	0.1194	0.02
0.02	0.1708	0.04
0.03	0.2105	0.06
0.05	0.2441	0.08
0.06	0.2736	0.10
0.07	0.3000	0.12
0.08	0.3123	0.13

Regarding flow dynamics, the determination of C_v and R_{cp} is dependent on the injection pressure. All simulations consider the same fixed upstream pressure for a range of downstream pressures. For the same GLV configuration with similar geometry, both the C_v and R_{cp} values should not

change significantly for different injection pressures since these quantities are primarily geometry-dependent.

2. Dynamic flow test run: This methodology suggests the use of a combination between the modeling and experimental methods to determine C_v and R_{cp}. Regarding the dynamic test, a single test run for a fully open valve is conducted to create data points to calibrate the 1D model. The fully open valve occurs at a point where the equivalent open area between the stem tip and the seat becomes larger than the orifice area itself. The test results facilitate the plotting of flow rate versus downstream pressure and the determination of flow coefficient (C_v) and critical pressure ratio (R_{cp}) for the fully open condition.

The flow coefficient is given by the intercept of the straight-line equation to the plot of YC_v versus R_c. Equation 3.14 for YC_v is derived from the flow rate (Equation 3.1). According to API 11V2 (2001), a horizontal from $0.667 \times C_v$ to the trend line in the plot indicates the value of R_{cp}. Figure 3.6. presents the plot of YC_v versus pressure ratio (R_p) as well as indications of the referent the procedure explained. Repeating this procedure for multiple stem positions facilitates the creation of the C_v versus d_{xs} and R_{cp} versus d_{xs} plots to further calculate the correlation coefficients.

$$YC_v = \frac{V_{MSCF/D}}{32.54\, P'_{cf} (R_p/T\,/\,\gamma_g/z)^{0.5}} \qquad 3.14$$

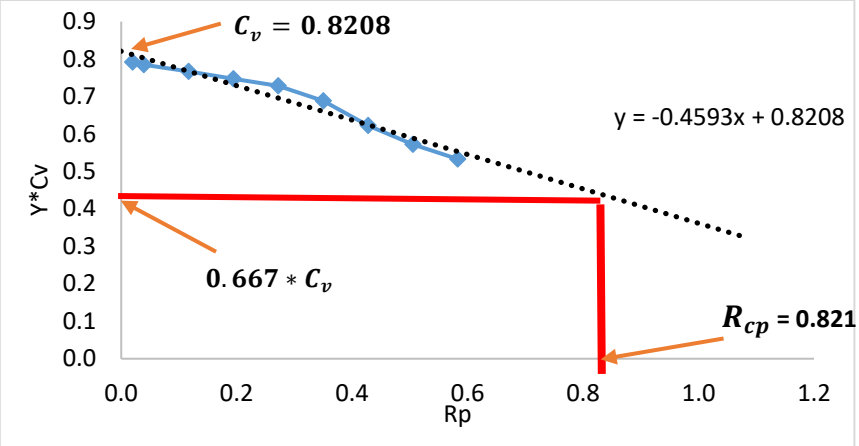

Figure 3.6. Plot of YC_v versus R_p and an indication of the procedure to determine the flow coefficient and critical pressure ratio for a fixed stem position.

3. 1D model calibration: Before simulating the full range of stem positions, this thesis proposes a model calibration using experimental data. The dynamic flow test provides data points of the flow coefficient at maximum stem travel, which are used to adjust the parameters of the model to match the test data. Since the valve is fully open at maximum stem travel, the maximum flow area is set as equal to the orifice area. In other words, the orifice fixed internal diameter becomes a constraint to the maximum possible open area of the valve.

   The adjusted parameters primarily include the check valve equivalent diameter and discharge coefficient. A few simulations with the valve fully open are required to manually adjust the parameters and minimize the difference between the C_v obtained from the simulation and the C_v obtained from the test at fully open dynamic flow. Figure 3.7. presents a flowchart of the model calibration procedure. The 1D model does not require detailed valve geometry and only considers the areas at the orifice and check valve. Therefore, to adjust the models, the open area at the check valve and the discharge coefficient serve as the calibrated parameters. The

adjustment continues until the modeled flow rate calculated by the 1D model matches the tested flow rate for a fully open valve.

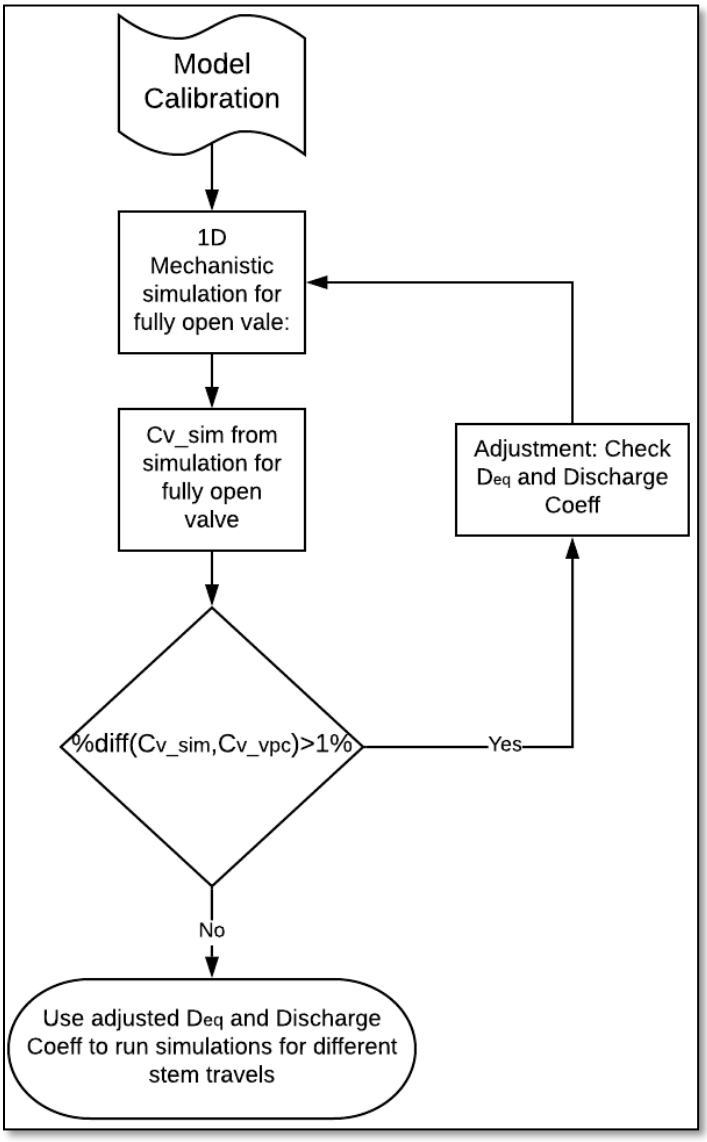

Figure 3.7. Workflow with steps utilized to calibrate the 1D mechanistic model

Information about the check valve open area is not always available from the manufacturer. Using test data facilitates adjustments to the area and discharge coefficient that would return C_v and R_{cp} values similar to those obtained from dynamic test data. Moreover, the check valve

condition is assumed to be fixed and independent of stem movement. Therefore, both the check valve and open area are the same for the entire range of stem travel.

4. Running for the entire range of d_x: After the model calibration procedure, the simulation was conducted for the entire range of stem travel and pressure drop across the valve. The injection pressure was assumed the same and equal to 1100 psi for all tested GLVs. Figure 3.8. presents a sample output from the 1D model for multiple stem positions. Each line data series in the graph represents results for one individual fixed stem position. After calculating the flow rates, C_v and R_{cp} were determined through the data processing procedures described by API 11V2 (2001) and Decker (1993b).

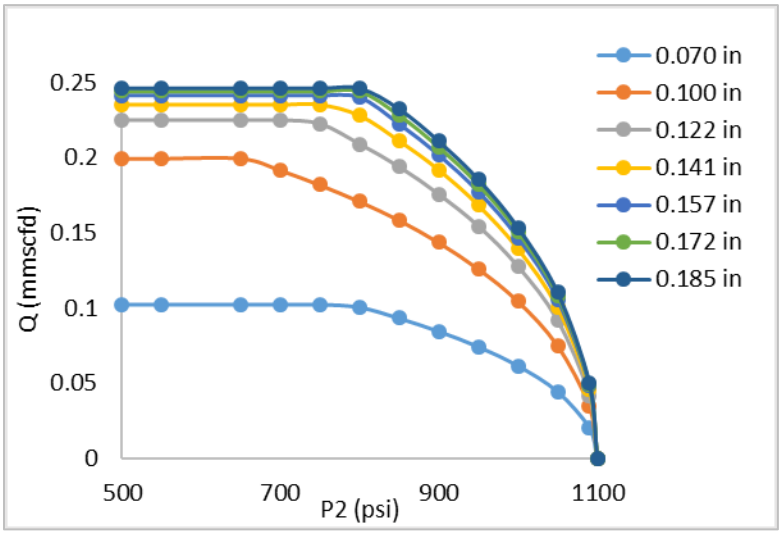

Figure 3.8. Sample output from the 1D model for a 12/64-inch valve and P1 = 1100 psi.

Since insufficient test data were available to compare against the simulation results for the present study, the VPC database served as a source of benchmark information. Thus, to validate the methodology, one of the criteria for selecting GLV configurations was the availability of information about the valve in the VPC database. As previously stated, the VPC database provides a means to determine the flow coefficient and critical pressure ratio as a function of stem travel. The database contains a set of polynomial coefficients that describe the behavior of C_v and R_{cp} for different stem positions. Equations 3.5 and 3.6 were used to obtain C_v and R_{cp}, respectively, which were used to benchmark results from the 1D model and assess model accuracy to characterize C_v and R_{cp}. Although this information does not represent direct test results, the coefficients originate from data processing and correlation development using the procedure described in API 11V2 (2001).

Additionally, the set of GLVs also included different manufacturers and multiple orifice sizes. This variability is important for assessing the efficacy of the model for different valve configurations. For this work, a selection of 12 different valve assemblies comprised the simulation matrix.

3.3. Computational Fluid Dynamic Modeling

Similar to the 1D modeling approach, CFD modeling is used to determine both C_v and R_{cp} as a function of stem travel for an IPO GLV. Briefly, this methodology consists of applying CFD to calculate the flow performance curve at specific stem positions and use this information to determine C_v and R_{cp}. The CFD technique consists of solving the governing equations for the 3D fluid domain, which represent the characteristics of the GLV. Specifically, this part of the research concentrates on assessing the efficacy of the CFD method to determine the coefficients of interest

and correlate C_v and R_{cp} with stem travel. For this study, a few general steps were performed to determine these coefficients for an IPO GLV and validate the results against information from test data compiled in the VPC database.

1) Select a set of GLVs with available experimental data that include information on the flow coefficient (C_v) and critical pressure ratio (R_{cp}).
2) Build tridimensional models for the selected valves using CFD techniques.
3) Run simulations for the valve configurations considering various combinations of upstream and downstream pressures on the GLV.
4) Process the data to determine the $C_v$and R_{cp} values for each stem position.
5) Compare the C_v and R_{cp} values from the CFD simulations to those of the experimental results.
6) Based on the results from item 5, discuss the applicability of the modeling techniques for determining the flow coefficient of GLV without the need to perform lab experiments (or the use of a reduced number of experiments).

3.3.1. CFD Mathematical Modeling

The CFD methodology consists of solving the equations of conservation of mass, momentum, and energy for a discretized fluid domain. In this study, the fluid domain consists of the 3D flow path through all of the internal components of the GLV. The CFD commercial package Ansys Fluent (Ansys, 2014) will be used in this study. This CFD package solves the governing conservation equations for each element of the discretized flow domain in a steady-state regime. Furthermore, since gas flow through the valve experiences high pressure and high flow velocities, especially under choke-like restrictions, the model also accounts for gas compressibility effects.

For a steady-state solution, time-dependent terms are neglected in the conservation equations. Equations 3.15, 3.16, and 3.17 are the three conservative equations solved for the discretized domain, and are described as follows:

(i) Mass conservation

$$\frac{\partial \rho u_i}{\partial x_i} = 0 \tag{3.15}$$

(ii) Momentum conservation

$$\frac{\partial \rho u_i u_j}{\partial x_j} = \frac{\partial \tau_{ij}}{\partial x_j} \tag{3.16}$$

(iii) Energy conservation

$$\frac{\partial \rho u_i h}{\partial x_i} = \frac{\partial}{\partial x_i}\left(k_c \frac{\partial T}{\partial x_i}\right) + \Phi + \left(u_i \frac{\partial p}{\partial x_i}\right) + H \tag{3.17}$$

The component τ_{ij} is defined as follows:

$$\tau_{ij} = 2\mu S_{ij} - p\delta_{ij} \tag{3.18}$$

and

$$S_{ij} = \frac{1}{2}\left(\frac{\partial u_i}{\partial x_j} + \frac{\partial u_j}{\partial x_i}\right) \tag{3.19}$$

where x_i indicates the cartesian coordinates, ρ is the density of the fluid, t is the time, u_i is the velocity component in the direction *i*, *p* is the static pressure, μ is the dynamic viscosity of the

fluid, h is the specific enthalpy, $k_c$is the thermal conductivity, T is the temperature, Φ is viscous dissipation, H is an energy source, and S_{ij} is the deformation tensor.

To account for gas properties regarding compressibility, the CFD model includes an equation of state (EOS), which is a mathematical relationship between the state function associated with the fluid. Variables such as temperature, pressure, volume, and internal energy are considered by the EOS. The ideal gas law is the simplest EOS and is commonly used for incompressible flow problems. However, for the specific problem in this research, which involves high pressure and high-velocity flow, the ideal gas law becomes inaccurate (Versteeg & Malalasekera, 2007). Therefore, the real gas model—i.e., the Aungier-Redlich-Kwong model—was used in this study to account for density variations with respect to pressure as well as temperature fluctuations along the flow path (Aungier, 1995; Poling et al., 1959).

The Aungier-Redlich-Kwong model implemented in Ansys Fluent employs an EOS in the following form (Ansys, 2014).

$$P = \frac{RT}{V - b - c} - \frac{\alpha(T)}{V(V + b)} \qquad 3.20$$

where R is described by R_u/MW (R_u = Universal gas constant; M_W = molecular weight), P is the absolute pressure (Pa), V is the specific volume (m^3/kg), and T is the temperature. The terms $\alpha(T), b,$ and c are expressions calculated as a function of the reduced pressure (P_r), reduced temperature (T_r), critical pressure (P_c), critical temperature (T_c), critical volume (V_c), and acentric factor ω (Aungier, 1995; Kontogeorgis & Tassios, 1997; Owczarek & Blazej, 2003; Sladkov, 2001). More details regarding the Aungier-Redlich-Kwong model implemented by the Ansys Fluent CFD solver can be found in Ansys (2014) and Aungier, (1995) .

The Reynolds Average Navier Stokes (RANS) equation, proposed by Reynolds (1895), is utilized to treat the turbulence phenomena. A series of turbulent models are built around the RANS approach of the so-called Reynolds average. The RANS approach uses a statistical method to model the effects of turbulent pressure and velocity fluctuations, and the governing equations are defined as a set of averages of the conservative equations. This approach simplifies the problem's solution since these quantities only vary slightly in time and space. Thus, a generic variable Φ, as presented in Equation 3.21, is described by the combination of an average portion and a fluctuation resulting from the turbulent effects.

$$\Phi = \Phi_m + \Phi' \tag{3.21}$$

$$u = \bar{u} + u' \; and \; p = \bar{p} + p' \tag{3.22}$$

where Φ is the value of the variable at a specific time t (e.g., velocity, pressure), Φ_m is the time-average of the variable Φ, and Φ' is the turbulent fluctuation at a time t. Figure 3.9. presents a graphic representation of the instantaneous velocity and the average line.

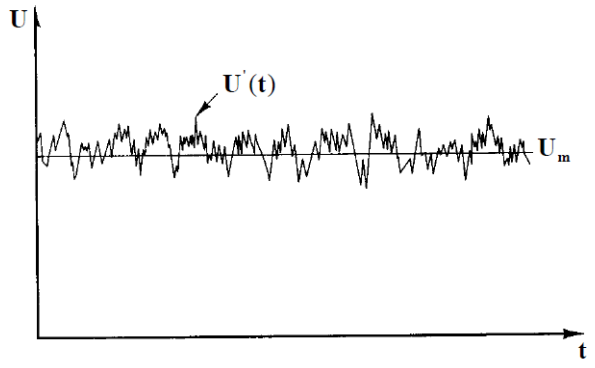

Figure 3.9. Representation of the instantaneous velocity component and the average velocity considered in RANS turbulence models.

By substituting the decomposed variables, the conservation equations for mass and momentum can be rewritten (see Equations 3.23 and 3.24).

$$\frac{\partial \overline{u}_i}{\partial x_i} = 0 \tag{3.23}$$

$$\frac{\partial \left(\rho \overline{u}_i \overline{u}_j\right)}{\partial_{xj}} = \frac{\partial \tau_{ij}^{turb}}{\partial_{xj}} + \frac{\partial \tau_{ij}}{\partial_{xj}} \tag{3.24}$$

The term τ_{ij}^{turb}, defined as the Reynolds tensor, appears as a consequence of the decomposition of the equations as a function of the mean and instantaneous fluctuations of the variables.

$$\tau_{ij}^{turb} = -\begin{bmatrix} \overline{u'_1 u'_1} & \overline{u'_1 u'_2} & \overline{u'_1 u'_3} \\ \overline{u'_2 u'_1} & \overline{u'_2 u'_2} & \overline{u'_2 u'_3} \\ \overline{u'_3 u'_1} & \overline{u'_3 u'_2} & \overline{u'_3 u'_3} \end{bmatrix} \tag{3.25}$$

Reducing the model complexity was important for the feasibility of the present study. Although the real-scale domain is not considered large, the use of more detailed modeling of the flow turbulence—such as large edge simulation (LES) and direct numerical simulation (DNS)—would require prohibitively long computational times (Versteeg & Malalasekera, 1980). Therefore, this work employs a two-equation RANS model referred to by the Ansys Fluent solver as the $k - \varepsilon$ standard, whose application is already consolidated with satisfactory results for cases involving gas flow modeling. The $k - \varepsilon$ standard model is largely employed to treat the turbulent phenomenon in diverse engineering and scientific problems (Kumar et al., 2020; Sakthivel et al., 2011; Yusof et al., 2020). Some benefits of this model include robustness, relatively low requirements for computational capabilities, and reasonable accuracy. Despite its wide use, the

model has certain deficiencies, such as flow in the presence of curvature of streamlines, flow under conditions of adverse gradients, flows in separation regions, flows with rotation, and the need for functions to treat the flow in close-to-wall regions(Ansys, 2013; Versteeg & Malalasekera, 1980).

The standard $k-\varepsilon$ approach is semi-empirical, which means that the derivation of the equations is based on phenomenological and empirical considerations. Assumptions for the k-ε model include the flow being completely turbulent and the omission of molecular viscosity (Pope, 2000). Moreover, turbulent viscosity is a function of the production of turbulent kinetic energy (k) and the dissipation of turbulent kinetic energy (ε), as follows:

$$\mu_T = {C_\mu \rho k^2}/{\varepsilon} \tag{3.26}$$

where $C_\mu = 0.09$ is an empirical constant.

From these two properties, it is possible to obtain the length scale ($L = k^{\frac{3}{2}}\varepsilon$) and the time scale ($\tau = C_\mu \frac{k^2}{\varepsilon}$). Equations 3.27 and 3.28 are the differential equations solved to calculate the values of turbulent kinetic energy (k) and its dissipation (ε), respectively.

$$\frac{\partial}{\partial x_j}\left(\rho \overline{u_j} k\right) = \frac{\partial}{\partial x_j}\left[\left(\mu + \frac{\mu_t}{\sigma_\kappa}\right)\frac{\partial k}{\partial x_j}\right] + G_\kappa + G_b - \rho\varepsilon \tag{3.27}$$

$$\frac{\partial}{\partial x_j}\left(\rho \overline{u_j} \varepsilon\right) = \frac{\partial}{\partial x_j}\left[\left(\mu + \frac{\mu_t}{\sigma_\varepsilon}\right)\frac{\partial \varepsilon}{\partial x_j}\right] + C_{1\varepsilon}\frac{\varepsilon}{k}\left(G_k + C_{3\varepsilon}G_b\right) - C_{2\varepsilon}\rho\frac{\varepsilon^2}{k} \tag{3.28}$$

where G_k represents the generation of turbulent kinetic energy due to the gradients of average velocity, G_b is the generation of turbulent kinetic energy due to turbulent fluctuations, $C_{1\varepsilon}$, $C_{2\varepsilon}$,

and $C_{3\varepsilon}$ are constant, and σ_k and σ_ε represent the turbulent Prandtl numbers for k and ε, respectively. Cable (2009) presented the definitions for the terms G_k and G_b as follows:

$$G_k = \rho\overline{u_i u_j}\frac{\partial u_j}{\partial x_i} \tag{3.29}$$

$$G_b = \beta g_i \frac{\mu_t}{\mathrm{Pr}_t}\frac{\partial T}{\partial x_i} \tag{3.30}$$

Further details regarding standard $k-\varepsilon$ modeling have been described by various authors (e.g., Kolmogorov, 1991; Ansys, 2013; Uygun et al., 2004; Versteeg & Malalasekera, 2007; Yusof et al., 2020), who also describe the equations for turbulent fluid flow modeling.

The solver used in this research was Ansys Fluent version 18.1. This software employs the finite volume method to solve the governing equations for the flow in every element of the flow domain.

The numerical discretization of the differential equations governing flow involves using the upwind method, which contributes to the numerical solution stability. However, in some cases, the first-order upwind is associated with numerical errors that can attribute to precision problems. Considering the numerical limitation of this method, the second-order upwind was used for the spatial discretization of transport equations in this work. Notably, Versteeg & Malalasekera (1980) discussed the upwind method in greater detail.

For gradient term discretization, least-squares cell-based discretization was used in this research. This choice was based on this method involving the lowest amount of computational effort for simulations when compared to other methods (e.g., Green-Gauss type methods). For the transient formulation, the first-order implicit method was applied. Further details regarding these methods can be found in Ansys (2013).

For pressure-velocity coupling, the semi-implicit method for pressure-linked equations (SIMPLE) was considered in the simulations. This approach initializes the pressure field based on an initial guess and resolves the discretized momentum equations based on these values. A correction for the pressure is then applied. Pressure and velocity adjustment occur through an iterative process until reaching the convergence criteria (Ansys, 2013; Versteeg & Malalasekera, 1980).

3.3.2. CFD Modeling Configuration

The computational model of a GLV represents the internal flow domain or the gas flow path through the valve. To create this type of model, GLV geometry details can be obtained from the valve's technical drawings or manual measurements of the actual GLV, if available. For these specific valve configurations, the model was built using information from the technical drawings from the valve manufacturer catalog. Since not all of the required details were available from the manufacturer catalog, some components (e.g., the geometry of the check valve format) were approximated based on valves of similar geometry. Different valve designs and the shape of the check valve vary from one model to another, changes in the fluid domain may influence the flow field for different valves. However, since valve designs typically consist of similar restrictions (e.g., inlet port, orifice, check valve, and outlet port), some similarities remain—even among valves from different manufacturers.

For the present study, the 3D model of the fluid domain corresponded to the valve section shown in Figure 3.10, which is constrained between the inlet port and the outlet port of the section. The computational fluid domain represents the internal volume of the valve for the gas flow path. Specifically, the model shown in this figure is for an IPO GLV with a 12/64-inch port size. This valve includes five inlet orifices, a 12/64-inch orifice port, a check valve, and an outlet port. To

facilitate the convergence of the numerical simulation, both inlet and outlet regions were elongated from the original dimensions. This technique allows a less turbulent flow and avoids backflow close to the inlet and outlet of the domain, which also reduces the formation of vortexes in these zones. Notably, backflow contributes to the instability of the numerical solution and may lead the simulation to diverge.

While the dimensions are closely related to the actual valve dimensions, slight deviations may occur due to the lack of detailed information and approximations being used for the drawings. Despite deviations from the real valve, the equivalent diameters at the main restrictions (e.g., the inlet port, outlet port, orifice, and check valve) match those of the original valve design. Furthermore, this valve model was specifically selected due to the availability of both FCT data (with a modified valve) and correlation data for the flow coefficient at different stem positions.

Regarding the boundary conditions, both the inlet and outlet of the domain are set using a specific pressure to replicate the method of the laboratory test using a modified GLV. To achieve this, the pressure-inlet boundary condition must cover the inlet, while the pressure-outlet boundary condition covers the outlet of the flow domain. The remaining faces of the domain are set using a wall (non-slip) boundary condition. Table 3.3 presents a summary of the boundary conditions and a brief description of their representation.

Figure 3.11 presents a view of a central plane going through the valve to allow visualization of the internal flow domain. Notably, each stem position translates into a different model or different flow domain, as can be observed in Figure 3.11.

Fluid domain and location of boundary conditions *Valve*

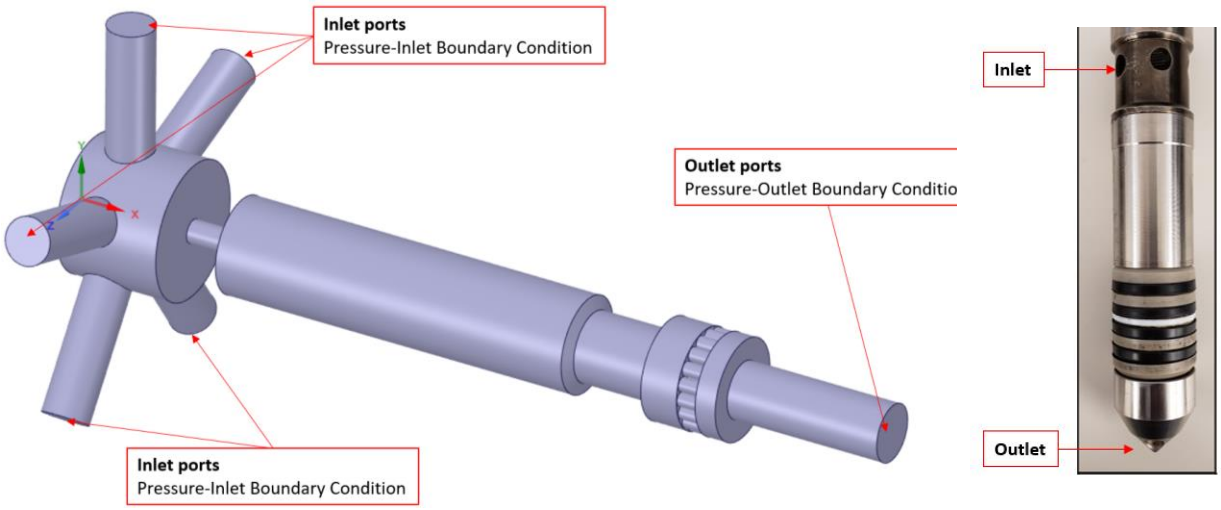

Figure 3.10. Representation of the flow domain of a 12/64-inch injection pressure-operated gas lift valve with the locations of the boundary conditions indicated. On the right side, the section corresponding to the fluid domains is shown.

Table 3.3. Description of boundary conditions for the gas lift valve computational fluid dynamics model

Face boundary	**Boundary condition**
Inlet port (five faces)	*Pressure-Inlet:* Defines a fixed pressure condition for the inlet. $P_{inlet\ boubdary} = P_{1\ (gauge)}$
Outlet port	*Pressure-Outlet:* Defines a fixed pressure condition for the outlet. $P_{Outlet\ boubdary} = P_{2\ (gauge)}$
Wall and stem tip (All solid faces that encompass the fluid domain, except for the inlet and outlet ports)	*Wall, no-slip:* Defines a no-slip wall condition with all three components equal to zero. $\bar{u} = \bar{v} = \bar{w} = 0$

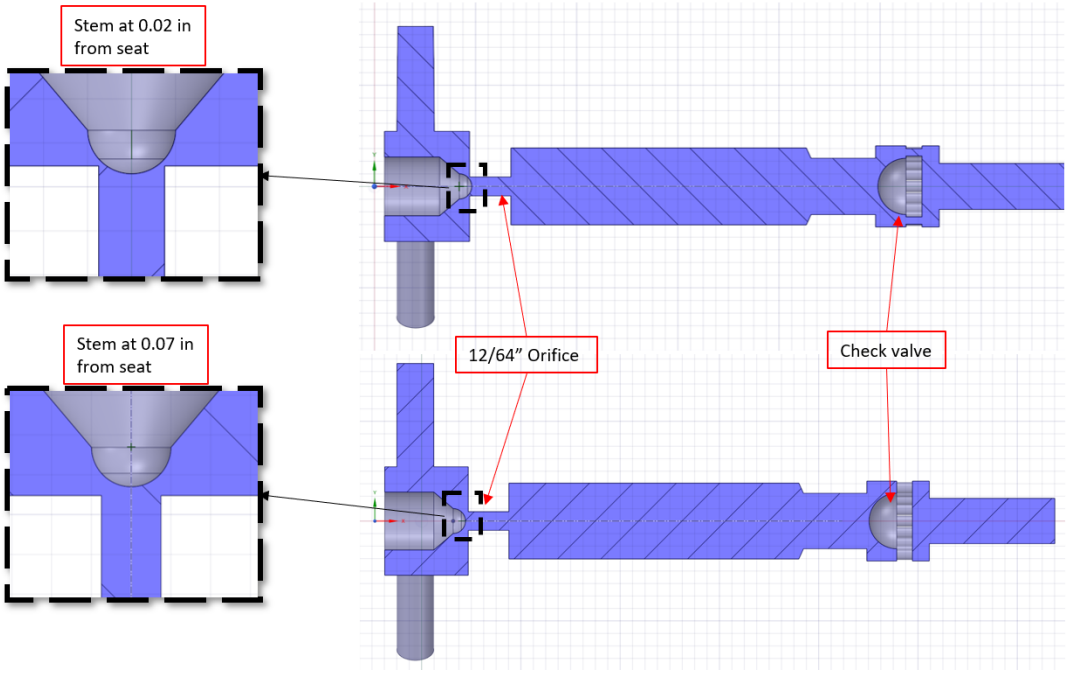

Figure 3.11. Internal details of the flow domain for the injection pressure-operated valve with a 12/64-inch port size and the stem position at 0.02 and 0.07 inches from the seat.

After building the computational flow domains, the next step of the CFD method involves discretizing the flow domain into a finite number of elements or cells. To determine the characteristics of the computational grid, a mesh independency test was conducted to evaluate the influence of different grid refinements on the solution accuracy. Since this work deals with multiple different geometries, the independence test serves as a basis for creating the grid and maintaining a similar number of elements among the different meshes. Typically, the grids are characterized by tridimensional tetrahedral cells with minimum cell sizes of 0.0043 inches at the region of finest refinement in the gap between the stem and the orifice seat edges. For the remainder of the geometry, the average cell size is 0.024 inches. A smooth inflation layer with three hexahedral cells is also considered to better predict the viscous sublayer close to the wall boundary. Regarding the number of cells, the grids contain between $3.1\,x\,10^6$ and $3.6\,x\,10^6$

tridimensional cells, on average. Besides the refined zones close to the orifice, the element size is relatively uniform throughout the domain, which positively affects the mesh quality and leads to fewer convergence issues. Figure 3.12 presents one of the discretized flow domains for 12/64-inch GLVs. For further details regarding the grid independence test, refer to Appendix I.

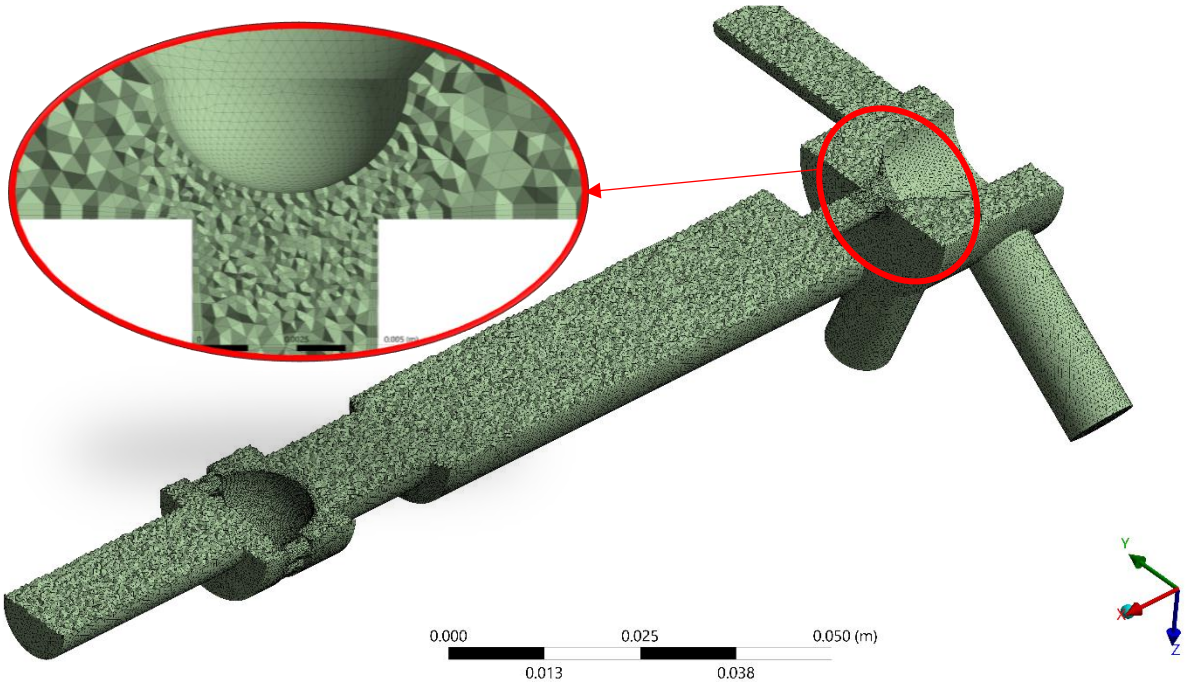

Figure 3.12. Computational grid of the domain of a 12/64-inch injection pressure-operated gas lift valve highlighting refinement at the restriction between the stem tip and orifice.

Table 3.4. Summary of the 3D grid quality metrics for the 12/64-inches gas lift valve shown in Figure 3.12

Mesh metric	Average	Descriptions
Orthogonal Quality	0.83	Range 0 to 1: values closer to 1 indicate the best quality
Skewness	0.21	Determines how close to ideal (that is, equilateral or equiangular) a face or cell is. 0 to 1: values closer to 0 indicate the best quality
Aspect Ratio (AR)	1.90	The ratio of the longest cell edge length to the shortest edge length. AR =1 for equilateral cells

In total, four different orifice port size configurations are considered for the CFD modeling of flow capacity: 12, 16, 20, and 24/64ths of an inch. Therefore, three different stem positions are considered for each orifice size, totaling 12 different geometries for the CFD simulations (see Table 3.3). To obtain the flow performance for each geometry, the injection pressure (P1) is kept constant while the production pressure changes in 200-psi increments until reaching critical flow.

Table 3.5 presents a summary of the cases used for CFD simulation, including the valve geometries and pressures (P1 and P2) considered for the simulations. It is important to emphasize the number of simulations required to characterize each valve. Considering three stem positions for each orifice size, a total of 18 simulations were required to cover all six downstream pressures. Therefore, for the four orifice sizes, the total number of cases for this work was 72.

The Louisiana State University High-Performance Computer (HPC) system was employed to perform the simulations with a set of 10 computing nodes with 16 processors and 64 GB of memory per node. The processor was an Intel Xeon 64bit with a 2.6GHz processor speed. In other

words, 160 cores were utilized per simulation, which took on average 5 hours to complete for each simulation case.

Results from the CFD methodology include flow performance curves (gas flow rate as a function of the downstream pressure) for fixed stem positions, flow coefficient (C_v) versus stem position, and critical pressure ratio versus stem position curves. The results were compared against available experimental data and data from the VPC database to assess the capability of the model to accurately predict the variables of interest.

Table 3.5. Cases considered for computational fluid dynamics modeling and simulation including four different orifice sizes and three stem positions per orifice size

Case geometry	Valve orifice size (inches)	Stem positions (inches)	P1 (psi)	P2 (psi)
01	12/64	0.02	1100	200, 400, 600, 800, 1000, 1050
02		0.04	1100	200, 400, 600, 800, 1000, 1050
03		0.07	1100	200, 400, 600, 800, 1000, 1050
04	16/64	0.02	1100	200, 400, 600, 800, 1000, 1050
05		0.04	1100	200, 400, 600, 800, 1000, 1050
06		0.08	1100	200, 400, 600, 800, 1000, 1050
07	20/64	0.04	1100	200, 400, 600, 800, 1000, 1050
08		0.08	1100	200, 400, 600, 800, 1000, 1050
09		0.12	1100	200, 400, 600, 800, 1000, 1050
10	24/64	0.04	1100	200, 400, 600, 800, 1000, 1050
11		0.10	1100	200, 400, 600, 800, 1000, 1050
12		0.16	1100	200, 400, 600, 800, 1000, 1050

Chapter 4. Results and Discussion

This chapter is divided into two main sections:

1- Results from the 1D mechanistic modeling: 12 different valve configurations modeled and simulated using PIPESIM as the solver platform.

2- Results from the CFD study: 4 different valve configurations simulated using Ansys Fluent.

For both sections, the simulated valve had the same four orifice port sizes: 12, 16, 20, and 24/64 inches. The main goal of these simulations was to determine the accuracy of using the 1D and 3D CFD models to replicate the results obtained experimentally for C_v and R_{cp}.

4.1. One-dimensional Modeling Results

This section contains the results of the 1D mechanistic modeling applied to replicate the FCT and determine the flow coefficient (C_v) and critical pressure ratio (R_{cp}) as a function of the stem travel. The results are compared to data from the VPC database and available test data to assess the performance of the 1D model proposed in this study.

4.1.1. One-dimensional Mechanistic Modeling Definition

To obtain a representative model to characterize the flow coefficient and critical pressure ratio, a few tests were conducted to determine whether every restriction in the valve geometry should be considered. Moreover, the tests also assessed the impact of the different upstream pressures on the results to determine an appropriate range of upstream pressures for the simulations.

Figure 4.1 resents a comparison between the results of the 1D model considering all internal restrictions (i.e. inlet port, orifice, check valve, and outlet port) and a simplified model considering only the equivalent area at the orifice and check valve. The C_v values shown in

were obtained using the procedure described in Section 3.2.4. Most of the data points show very similar behavior, and the two models could predict the flow coefficient with very similar accuracy. This result was expected since the equivalent diameters at both inlet and outlet ports are considerably larger than the orifice port and check valve diameters. In other words, pressure drop at the inlet and outlet can be omitted to simplify the modeling. The valve design intends to reduce pressure drop at the inlet and outlet port since the main flow control feature should be the orifice port.

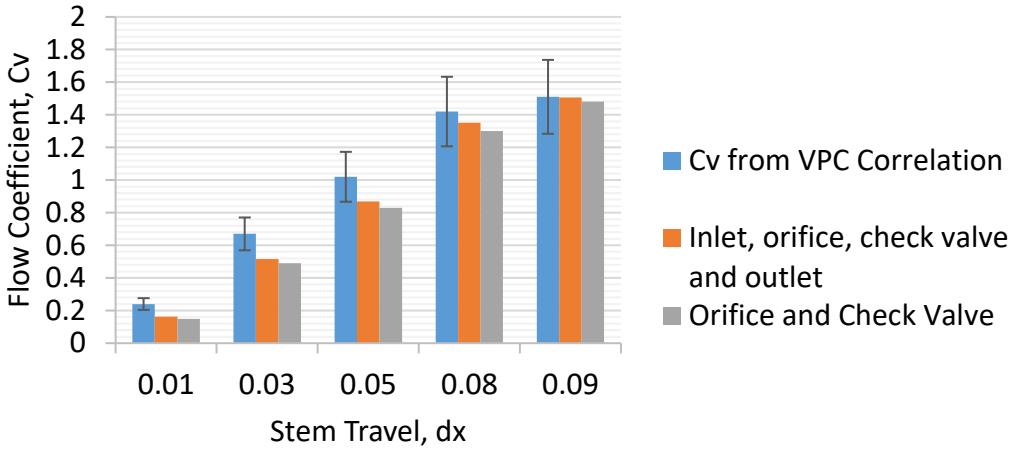

Figure 4.1. Comparison of results from the one-dimensional model considering all main restrictions and the one-dimensional model without the inlet and outlet port. The error bars indicate a variation of ±15% from the Valve Performance Clearinghouse correlation data.

Some important and positive aspects of this simplification include the fact that fewer features not only decrease the complexity of the model but also eliminate the requirement for

obtaining extra information about the valve. Additionally, fewer features also facilitate the calibration process and decrease the time required to run the simulations.

To assess the impact of different injection pressures on the flow coefficient and critical pressure ratio determination, this methodology includes four cases considering injection pressures of 500, 1100, 1500, and 2000 psi. Figure 4.2 shows the effect of upstream pressure on the estimation of C_v for different stem positions for the same 16/64-inch IPO valve. The results of the 1D model present C_v values for different injection pressures within an error range of 5%, which indicates no significant differences between data points for different upstream pressure levels. In other words, injection pressure does not have a significant impact on C_v, at least for the range of pressures considered in this study. Decker (1993b) emphasized that the flow coefficient combines the flow area and flow factor, and is weakly dependent on upstream pressure at each specific stem position. Similar behavior occurred for the critical pressure ratio shown in Figure 4.3, where R_{cp} values also fall within the range of the 5% error bars. In fact, the highest deviation of R_{cp} from the average value for a fixed stem position is approximately 2%. Therefore, we can conclude that, for this pressure range, both C_v and R_{cp} are weakly dependent on injection pressure when considering the same valve geometry with fixed stem travel. Importantly, this observation highlights the stability of the results and assists in defining the simulation matrix for the 1D modeling approach while reducing the number of simulations required to evaluate model performance. Since varying injection pressure does not lead to strong variability in the flow coefficient results, most of the 1D simulations in this thesis involved an upstream pressure of 1100 psi.

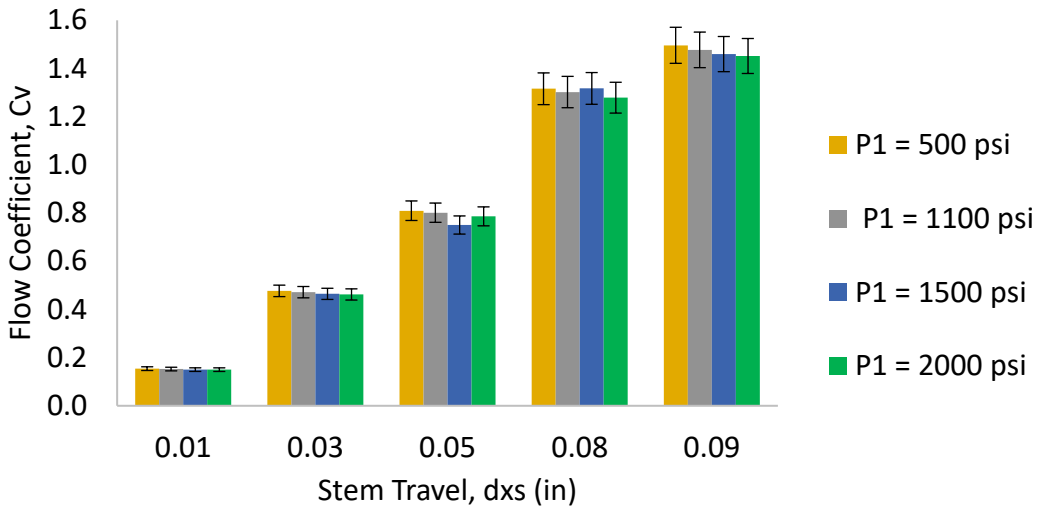

Figure 4.2. Bar plot of flow coefficient (C_v) versus stem position for different upstream pressures. The valve is considered a 16/64-inch injection pressure-operated gas lift valve. The error bars indicate a variation of ±5%.

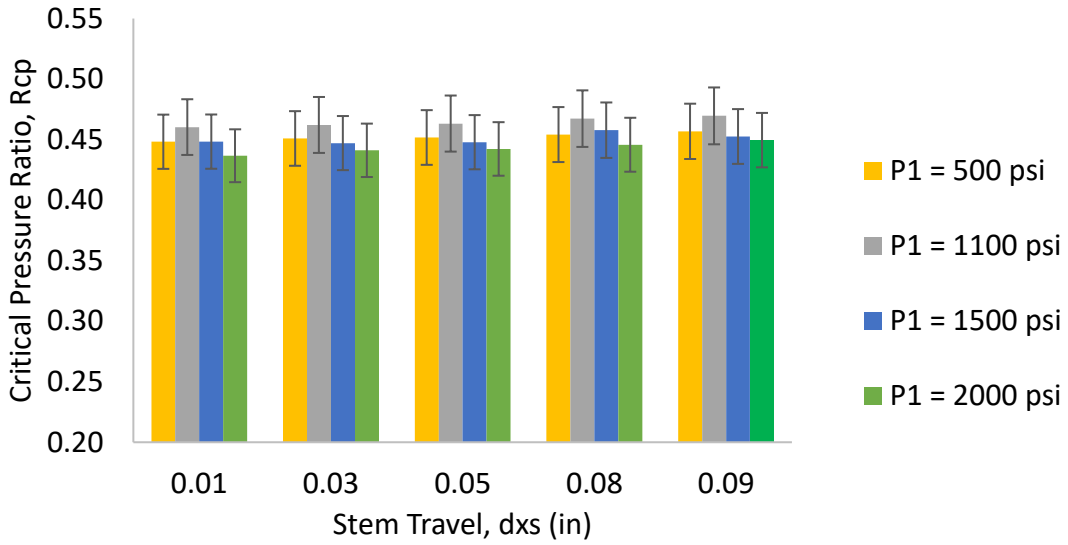

Figure 4.3. Bar plot of flow critical pressure ratio (R_{cp}) versus stem position for different upstream pressures. The valve is considered a 16/64-inch injection pressure-operated gas lift valve. The error bars indicate a variation of ±5%.

Due to the weak dependence of C_v and R_{cp} on injection pressure, a well as the need to reduce the number of simulations, an injection pressure of 1100 psi was considered for most of the

test runs in this work. Table 4.1 presents a description of the simulation conditions. Upstream pressure was maintained at 1100 psi, while downstream pressure varied from the injection pressure until critical flow was observed. For this thesis, the minimum production pressure was generally 100 psi, which generated a pressure drop of 1000 psi. The API recommends using a compressed gas such as nitrogen, air, or helium for GLV tests (API 19G2 et al., 2010). In this work, nitrogen (N_2) was used in simulations involving both the 1D and CFD models. Additionally, tests run by the VPC project at Louisiana State University also employ N_2 as the working fluid. The variables included the upstream pressure, downstream pressure, fluid type, and temperature ranges. Additionally, the simulation matrix considered different manufacturers with different port sizes for the valves. Each setup of valve model and orifice size was a distinct case, and a range of pressure differential was simulated to provide data points sufficient to determine the flow coefficient and critical pressure ratio. Table 4.2. presents the different valve models and port sizes used for the 1D model simulations. The first 12 valves were compared against data from either the VPC database or FCT using a modified valve to assess the accuracy of the model to determine C_v and R_{cp} values as a function of stem travel. Valve 13 was recently tested by the VPC project, and the modeling methodology proposed in this thesis was employed to predict C_v and R_{cp} as a function of stem travel.

Table 4.1. Parameters of the one-dimensional mechanistic model considered for this work

Inlet pressure *(psi)*	**Outlet pressure *(psi)***	**Fluid**	**Temperature (F)**
1100	1050 to 100	N_2	75

Table 4.2. List of valve models with respective port sizes considered for the 1D model simulations. The benchmark data column indicates origin of the data used for comparison to experimental results

Number	Valve name	Port size (/64 in)	Benchmark data	P1 (psi)
1	Weatherford R-1	12	VPC database	1100
2	Weatherford RH-2	12	Modified valve test data	1100
3	Camco R-20	12	VPC database	1100
4	Weatherford RH-2	16	Modified valve test data	1100
5	Weatherford R-2	16	VPC database	1100
6	Camco BK	16	VPC database	1100
7	Merla N-17R	20	VPC database	1100
8	PTC 15 IPO	20	VPC database	1100
9	Camco R-20	20	VPC database	1100
10	Weatherford RH-2	24	VPC database	1100
11	Merla N-17R	24	VPC database	1100
12	McMurry C-2	24	VPC database	1100
13	Priority IPOC-2	12	VPC test	1100

4.1.2. Comparison of One-dimensional Model Results with the Valve Performance Clearinghouse Database for Flow Rate, Flow Coefficient, and Critical Pressure Ratio

Figure 4.4 and Figure 4.5 present simulation results for the 1D mechanistic model of gas flow rate as a function of the downstream pressure for an IPO GLV with either a 12- or 24/64-inch orifice, respectively. For this specific valve, actual dynamic flow test data using a modified valve is available and a 1D model simulation was conducted at the same test pressure to compare the performance curve generated for a fixed stem position. The test considered an injection pressure of 1200 psi for the 12/64-inch GLV and 1140 psi for the 20/64-inch GLV, and the data show characteristic critical flow with an almost constant flow rate as the pressure drop increases. Additionally, for these specific cases, the injection pressure represents the maximum flow rate observed in the test, which allows us to assume a fully open valve condition. The 1D simulation also considered a fully open valve position with the stem fixed at either 0.07 or 0.16 inches from

the seat for the 12/64- and 20/64-inch IPO GLVs, respectively. The distance from the seat represents the point where the equivalent circular diameter of the open area between the stem tip and the orifice becomes larger than the orifice diameter itself. For both valves, the simulated flow rates match fairly well when compared to the performance curve generated from experimental results for the modified valves. Practically all data points fall within the 15% error bar range.

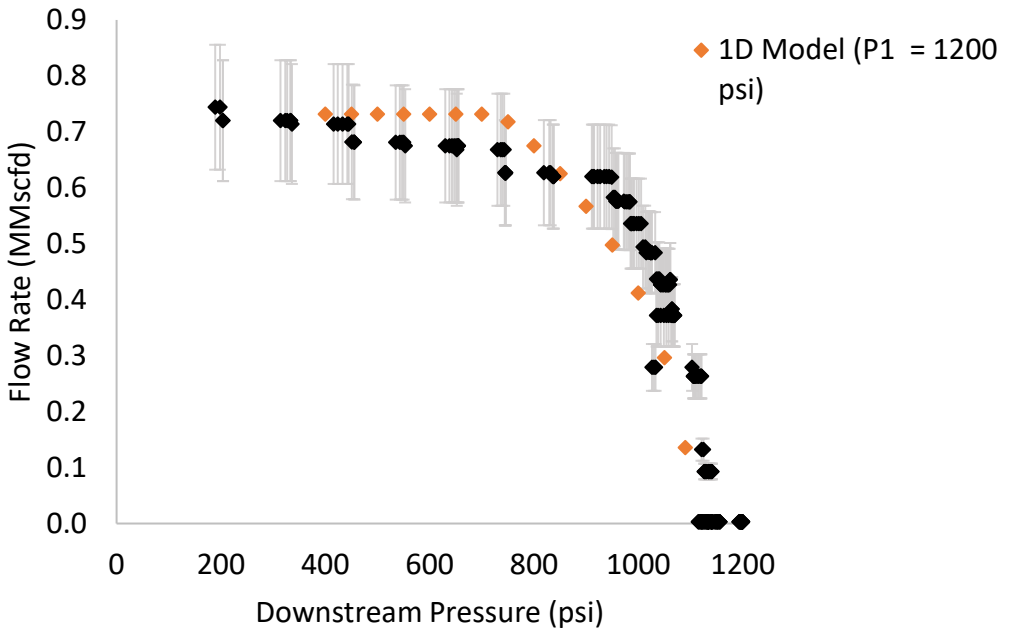

Figure 4.4. Production pressure versus flow rate for nitrogen flow simulation through a 12/64-inch injection pressure-operated gas lift valve with the stem located 0.07 inches from the seat. The error bars indicate a ±15% deviation range from the test data.

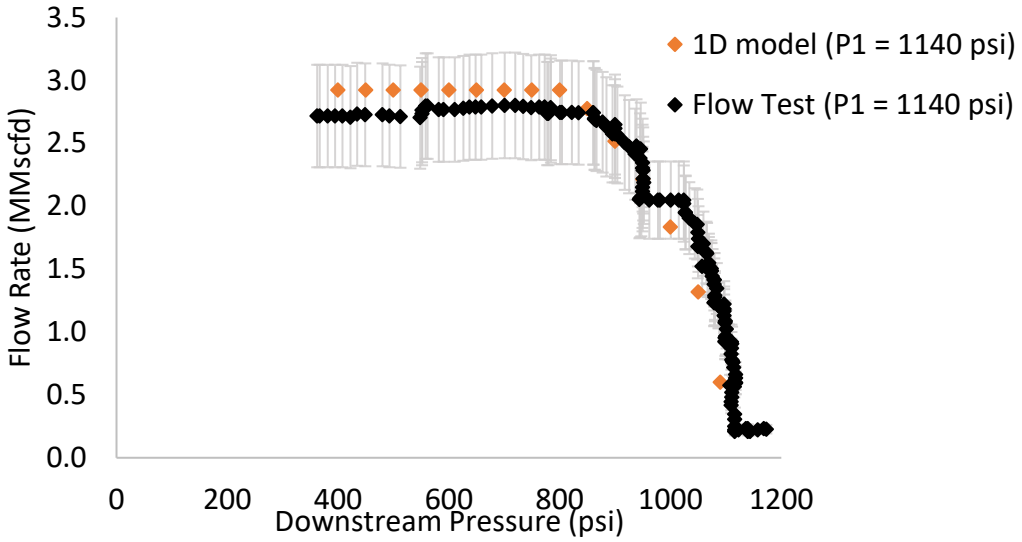

Figure 4.5. Production pressure versus flow rate for nitrogen flow simulation through a 24/64-inch injection pressure-operated gas lift valve with the stem located 0.16 inches from the seat. The error bars indicate a ±15% deviation range from the test data.

For a better evaluation of the 1D mechanistic modeling of the FCT, this study considered multiple GLV configurations from different manufacturers, models, and port sizes, as shown in Table 4.2. Notably, Figure 4.6 to Figure 4.9 present the values of flow coefficient and critical pressure ratio for the 12/64, 16/64, 20/64, and 24/64-inch IPO GLVs, respectively, considering multiple stem positions. The C_v and R_{cp} values from the 1D model were obtained by employing the procedure illustrated in Figure 3.6 (Decker, 1993b). The $C_v$and R_{cp} data points from the simulation were then compared to values generated from the VPC database to evaluate the performance of the modeling. $C_v$and R_{cp} results from the VPC database were computed using the available correlation coefficients and by implementing Equations 3.6 and 3.7.

Figure 4.6 presents the results for the 12/64-inches orifice valves, which is the smallest size tested in this study. Upon comparing C_v and R_{cp} values from the VPC database with the simulated

values, one can observe strong consistency between the data sets in terms of the magnitude of values and trend formed by the dataset. For different orifice sizes and valve models (Figure 4.6 to Figure 4.9), most of the graphs present similar behavior. Moreover, the simulated results form a smooth curve that is consistent with the results from the VPC database.

Overall, most of the simulated data points for all orifice sizes match the correlation data within a range of approximately 15% deviation. Considering the range of stem travel, the 1D model better predicts the flow coefficient for higher stem positions (i.e., larger open flow area). The majority of data points outside of the 15% error bars range appear for stem positions close to the valve seat (d_x = 0.02 in and d_x = 0.04 in). A better match for larger stem travel is likely due to the point of maximum opening being used to calibrate the model as well as the shape of the C_v curve being associated with a slightly bent line. Thus, simulated points close to the maximum opening are closer to the experimental data.

Similarly, the critical pressure ratio results also show similarity when compared to data from the VPC database for the pressure range and stem travel evaluated. In general, most of the R_{cp} results from the correlation only present slight changes, with increasing stem position behaving as a horizontal line in some cases. For some of the valve configurations, the VPC characterizes R_{cp} as a function of stem travel as a constant. For instance, the valves R-20 (16/64 inch) and RH-2 (for 12/64 and 16/64 inch) have R_{cp} fixed at a horizontal level. Stable behavior was also observed within the simulated data from the 1D model. Although the curves formed by the simulated data points differ from the correlation data (e.g., in valves R-20 12/64, R-2 16/64, R-20 20/64) in some cases, most data points still fall within a range of 15% deviation from the data obtained from the VPC database.

Moreover, very few systematic errors were observed since the 1D model underpredicted C_v for certain valve configurations and overpredicted in other cases. However, the simulated data points generally followed a similar trend to that observed in the experimental data. This result confirms that the 1D model approach can predict the flow coefficient and critical pressure ratio with at least 15% error for the specific cases simulated. The rightmost points in the C_v versus d_x, curves are equivalent to the maximum C_v obtained from the experiment and were used to calibrate the 1D model.

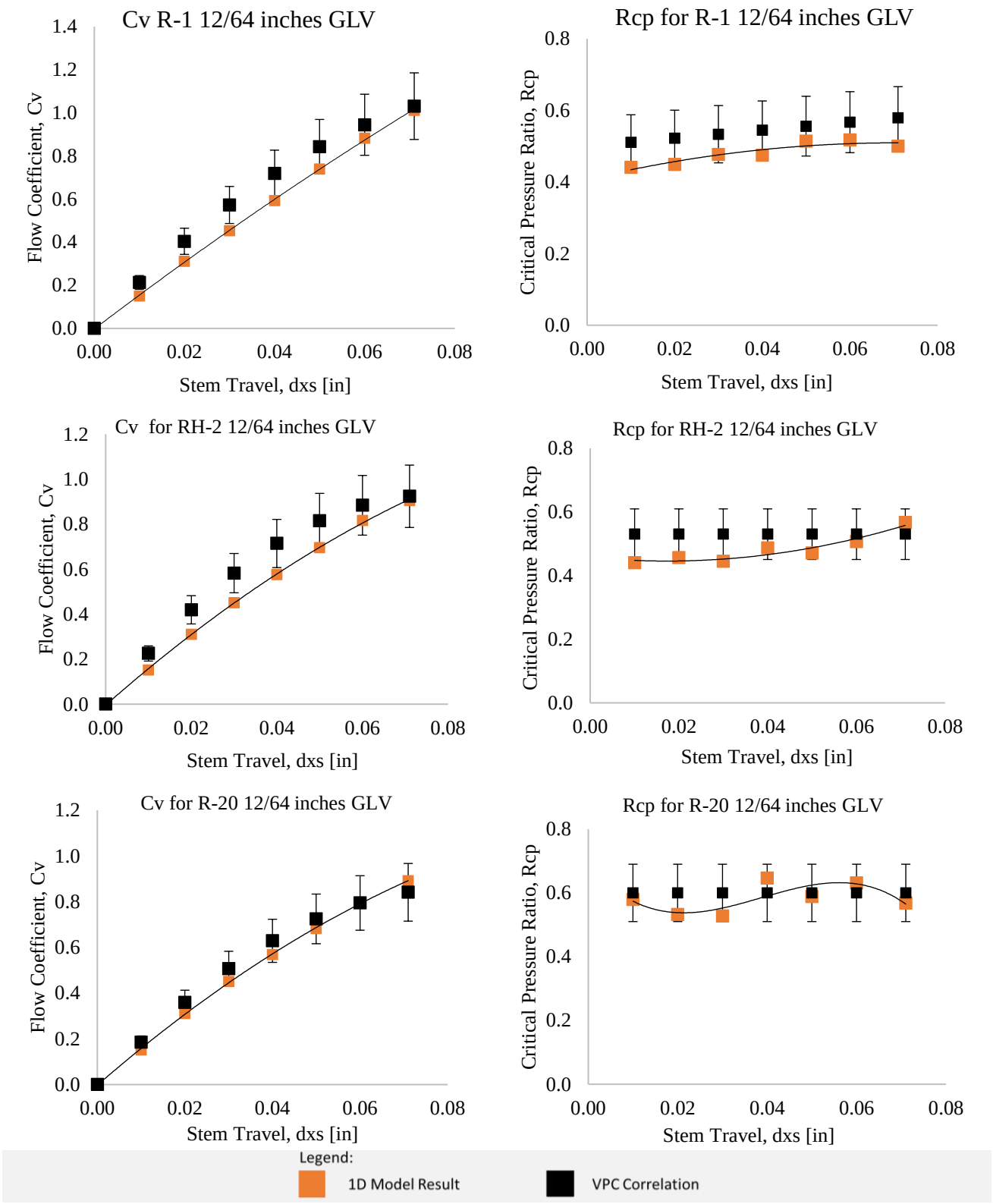

Figure 4.6. One-dimensional model simulation results of C_v and R_{cp} versus d_{xs} for the 12/64-inch gas lift valve. The error bars indicate a ±15% deviation range from the test data.

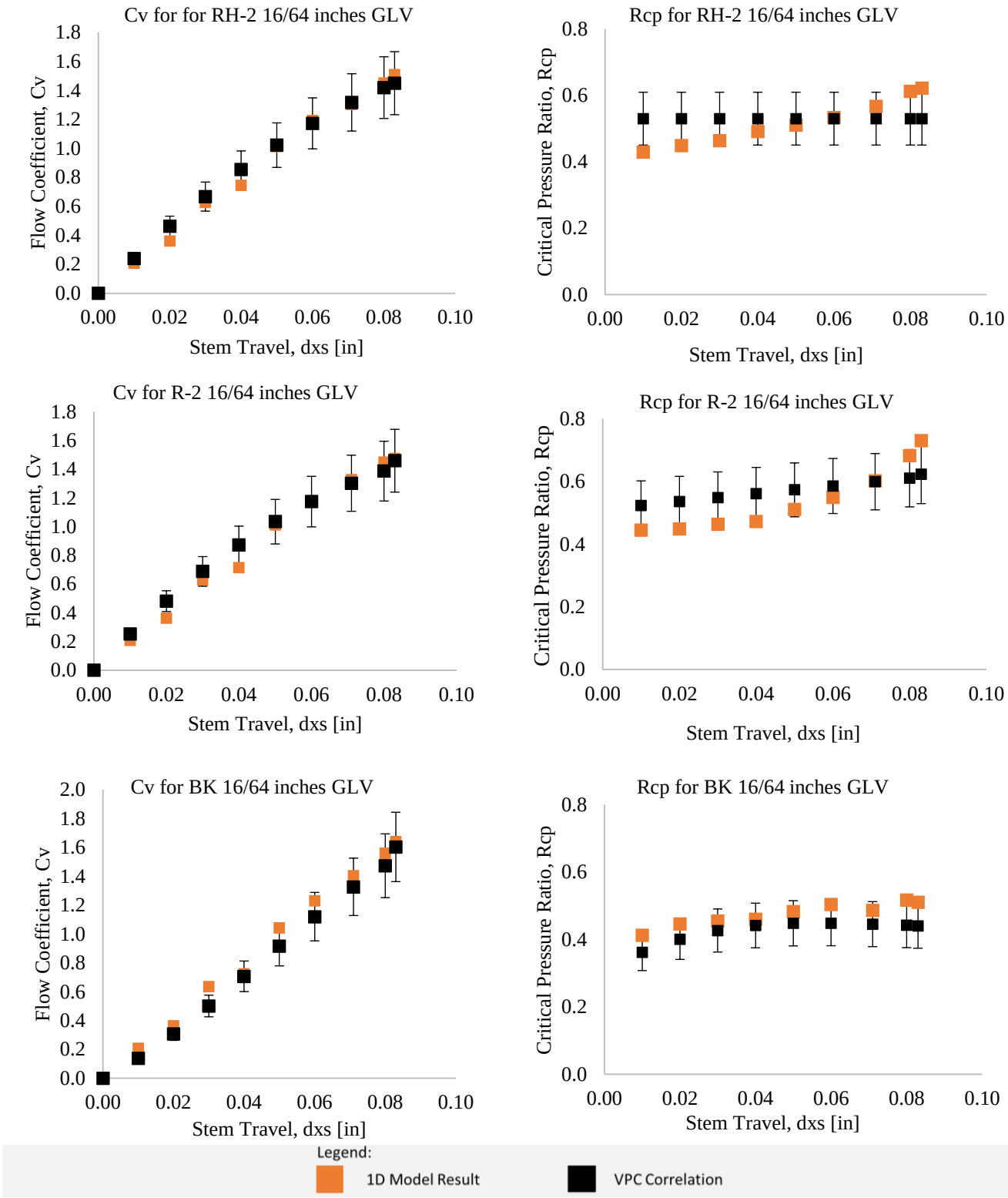

Figure 4.7. One-dimensional model simulation results of C_v and R_{cp} versus d_{xs} for the 16/64-inch gas lift valve. The error bars indicate a ±15% deviation range from the test data.

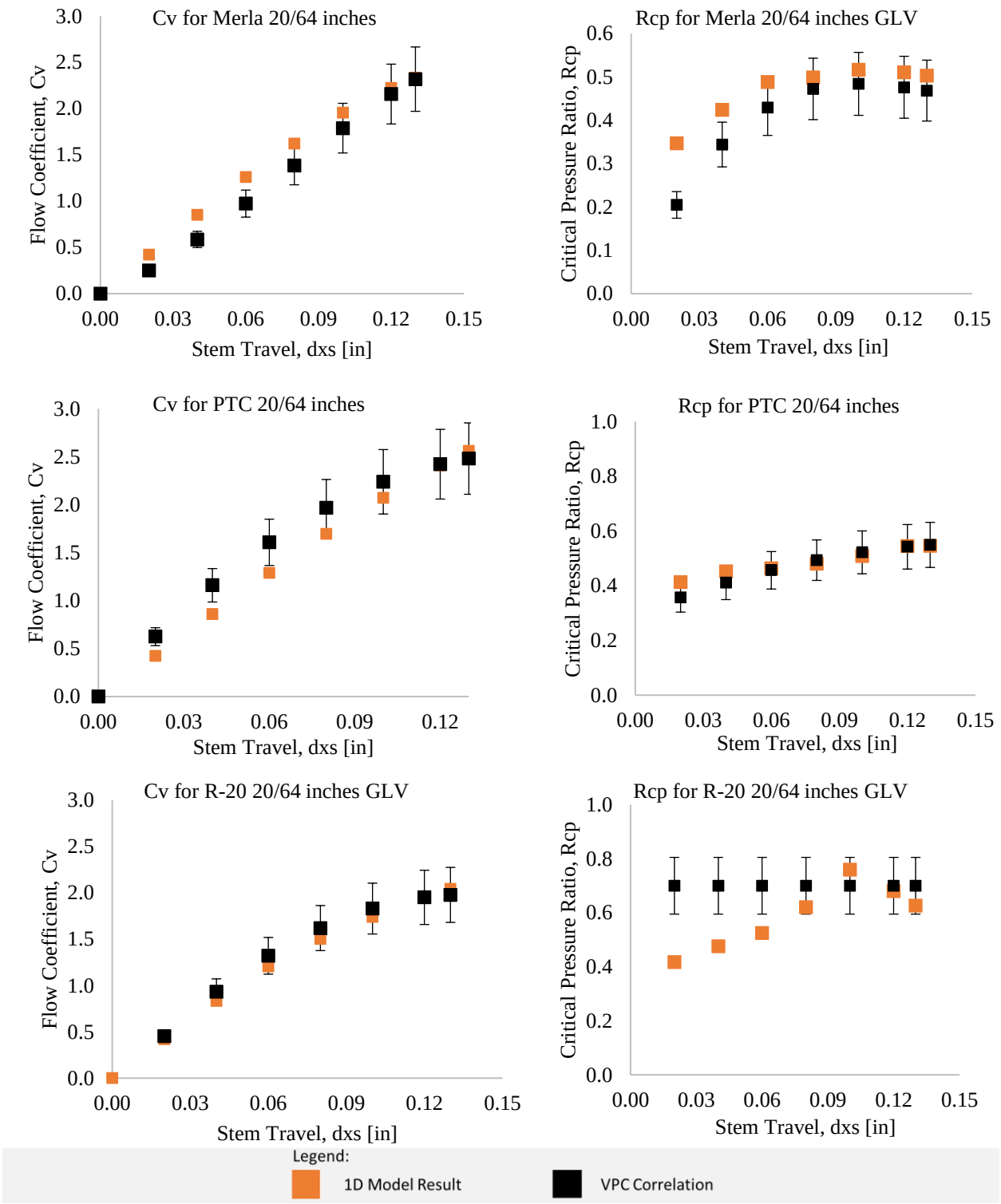

Figure 4.8. One-dimensional model simulation results of C_v and R_{cp} versus d_{xs} for the 20/64-inch gas lift valve. The error bars indicate a ± 15% deviation range from the test data.

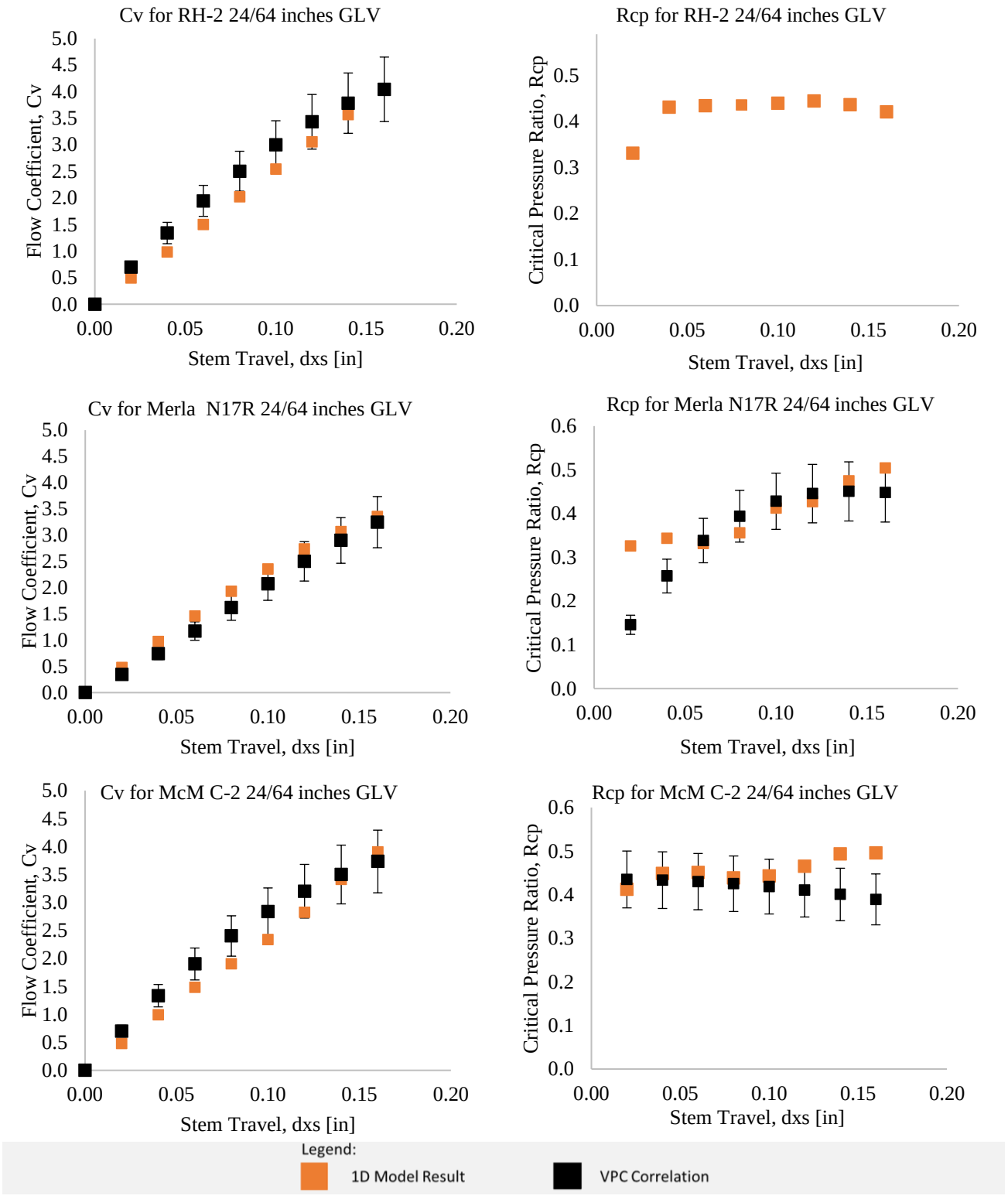

Figure 4.9. One-dimensional model simulation results of C_v and R_{cp} versus d_{xs} for the 24/64-inch gas lift valve. The error bars indicate a ± 15% deviation range from test data.

A summary of the average absolute errors for all 12 cases is presented in Table 4.3. Some valves (e.g., Weatherford RH-2) showed errors as low as 5% for C_v and 2% for R_{cp}. On the other hand, the highest average absolute error among the evaluated cases was approximately 25% for the Merla N-17R valve, with most cases around the 15% error range. Benchmarking the simulated results against data from the VPC database and test data allowed us to assess the performance of the modeling approach. In summary, for the cases presented in this study, an absolute average and average stable error range of up to 25% highlights the potential for using the 1D model to predict C_v and R_{cp} as a function of stem travel.

Table 4.3. Summary of average absolute error for the 1D model results of all 12 analyzed cases compared to VPC data and flow capacity test results with a modified valve

Valve name	**Port size (/64 inch)**	**Benchmark data**	**Average Absolute error (%)**	
			Cv	**Rcp**
Weatherford R-1	12	VPC database	16	12
Weatherford RH-2	12	Modified valve test data	18	9
Camco R-20	12	VPC database	7	9
Weatherford RH-2	16	Modified valve test data	5	2
Weatherford R-2	16	VPC database	7	6
Camco BK	16	VPC database	15	11
Merla N-17R	20	VPC database	25	19
PTC 15 IPO	20	VPC database	14	3
Camco R-20	20	VPC database	5	16
Weatherford RH-2	24	VPC database	19	-
Merla N-17R	24	VPC database	18	25
McMurry C-2	24	VPC database	14	9

4.1.3. Comparison of One-dimensional Model Results with Test Data for Flow Rate, Flow Coefficient, and Critical Pressure Ratio

As previously mentioned, one of the main advantages of using the 1D model to predict C_v and R_{cp} for IPO GLVs is the fact that no modified valve or dynamic FCT is necessary to obtain the parameters for the correlation. Notably, besides performing the FCT with the modified valve

method, it is possible to obtain C_v and R_{cp} from the dynamic flow test while considering a range of pressure drops below 100 psi. The test procedure is similar to that of a regular dynamic flow test except for the fact that the data points considered for calculating C_v and R_{cp} are only within the 100-psi range of the pressure differential. However, this method is particularly challenging to perform due to the strong variability of the pressure signal, especially during the tests for P1-P2 < 100 psi. Since no modified GLV is required for the test, the stem position is estimated for each upstream pressure and derived from the force balance described in Equation 4.1.

$$d_x = (P_{up} * (A_b - A_p) + P_{dn} * A_p - P_{vot} * (A_b - A_p)/A_b) / (LR * A_b) \quad 4.1$$

where d_x is the dynamic stem travel, P_{up} is the upstream pressure, A_b is the bellows area, A_p is the port area, P_{dn} is the downstream pressure, P_{vot} is the valve opening pressure, and LR is the LR obtained from the LRT.

For each upstream pressure, one stem position is calculated for the corresponding C_v and R_{cp} for that test. In other words, multiple tests considering a range of P1-P2 < 100 psi are required to develop a curve of C_v and R_{cp} versus stem position.

This method was performed for the valve IPOC-2 12/64, which was tested for the VPC project. Figure 4.10 and Figure 4.11 present the respective results of C_v and R_{cp} versus d_x from both the 1D modeling approach and the previously described experimental method for the injection of 1100 psi of pressure. The black square in Figure 4.10 indicates the C_v value from the dynamic test considering a fully open valve. For the C_v results, the deviations between experimental and simulated data extrapolated a 15% error range, while this specific case reached approximately 35% error. The data points from the experimental method are more scattered and concentrated at higher ranges of stem position when compared to the 1D model results. This variability suggests that the

results may not be entirely accurate since they show different C_v values for the same stem position. Despite these errors, C_v results from the two methods have values that approximate the reported accuracy of the VPC model (approximately ±20%) for stem positions above 0.04 inches. The 1D model provides a more stable and smoother curve that covers the entire range of stem travel from the fully closed valve position to the fully open position. Regarding the critical pressure ratio, Figure 4.11 presents the results of R_{cp} versus d_{xs} from the calibrated 1D model. Similarly, results from this test show high variability and are also concentrated toward the higher stem positions. This model also returns R_{cp} values for the full range of stem positions.

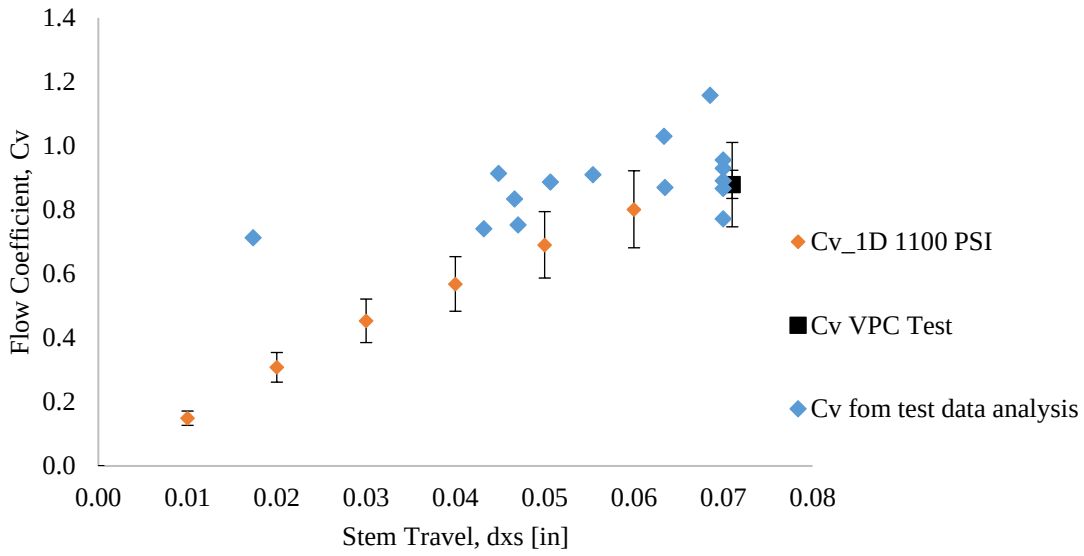

Figure 4.10. Comparison of C_v versus stem travel from the one-dimensional modeling and dynamic flow test for P1-P2 < 100 psi for an IPOC-2 12/64-inch valve. The error bars indicate a ±15% deviation range.

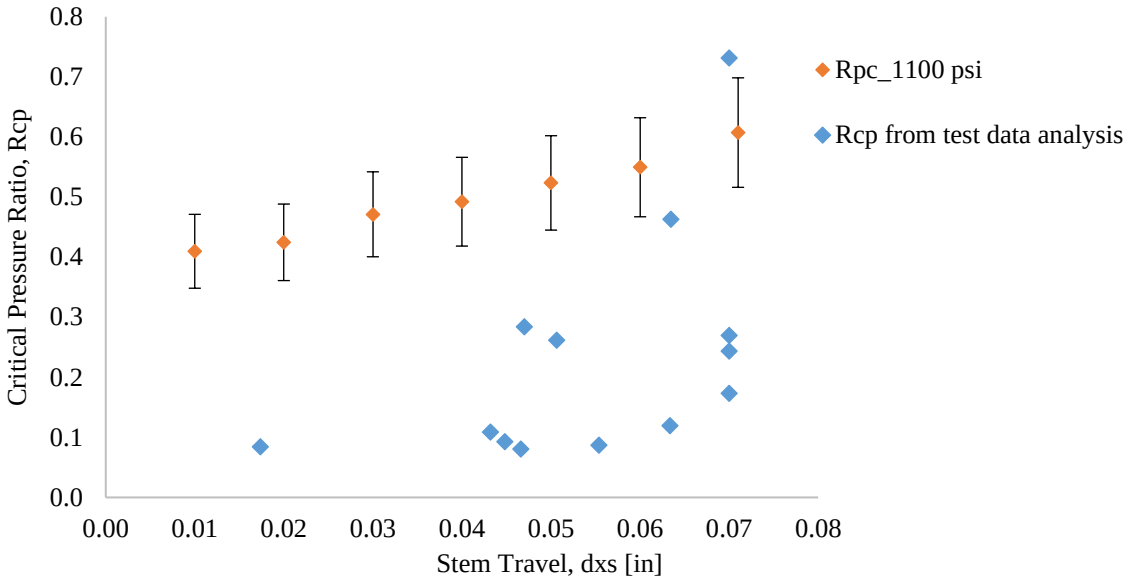

Figure 4.11. Comparison of R_{cp} versus stem travel from the one-dimensional modeling and dynamic flow test for P1-P2 < 100 psi for an IPOC-2 12/64-inch valve. The error bars indicate a ±15% deviation range.

4.2. Computational Fluid Dynamics Modeling Results

This section presents the results of the CFD model used to replicate the FCT. Similar to the previous section, the results of the flow coefficient C_v and critical pressure ratio R_{cp}— as a function of stem travel — are compared to data from the VPC database to assess the performance of the CFD model proposed in this study. Additionally, this section includes a discussion of the potential use of this CFD model to predict the force distribution at the stem tip to better understand the force balance dictating stem movement during gas flow through the valve.

4.2.1. Prediction of Flow Rate, Flow Coefficient, and Critical Pressure Ratio via Computational Fluid Dynamics Modeling

To obtain an accurate solution for the CFD model, aspects of the solution (e.g., the convergence of the numerical solution and deviation from available experimental benchmark data)

are analyzed. Since the CFD model consists of numerically solving the governing equations through the discretized fluid domain, the residues of the model's equations for numerical solutions (i.e., conservation of mass, momentum, energy, and the turbulent models k and ε) between iterations are considered acceptable when stabilized around a relative error of 10^{-5}. Previous works involving the CFD analysis of compressible flow utilized convergence criteria of 10^{-3} to 10^{-4} (Najar et al., 2013; Raback et al., 2001). However, for the case of this work, mass conservation (mass in- mass out = 0) was observed for ranges of residuals around 10^{-4} to 10^{-5}. Figure 4.12 presents an example of the residues for the 24/64-inch IPO valve simulation case with the stem positioned 0.16 inches from the seat. In general, the number of iterations required for the convergence of the residuals to a level of 10^{-5} was approximately 9000 to 15000, considering one stem position and a fixed pressure drop. For the utilized computing system, the number of iterations required 3 to 4 hours of processing time.

The net mass (mass flow in – mass flow out) in the domain should be zero or as close to zero as possible for a reasonable simulation result since the control volume does not have any additional mass source besides the inlet flow. Figure 4.13 presents the results of mass flow monitors at the inlet (positive values) and outlet (negative values) of the domain. At the beginning of the steady-state simulation, the inlet mass flow differed from outlet mass flow. As the simulation progressed, the net mass flow became zero as the flow entering the domain became the same as the flow leaving the domain. For the cases simulated in this work, an average percentage difference of 4% between inlet and outlet mass flow was observed.

iter	continuity	x-velocity	y-velocity	z-velocity	energy	k	epsilon
9417	1.2087e-05	1.8040e-07	9.5687e-08	8.8990e-08	1.9164e-06	6.3322e-07	5.1540e-07
9418	1.2091e-05	1.8025e-07	9.5640e-08	8.8713e-08	1.9230e-06	6.3316e-07	5.1484e-07
9419	1.2096e-05	1.8010e-07	9.5596e-08	8.8481e-08	1.9295e-06	6.3310e-07	5.1428e-07

Figure 4.12. Computational fluid dynamics simulation convergence of residues from the governing equations

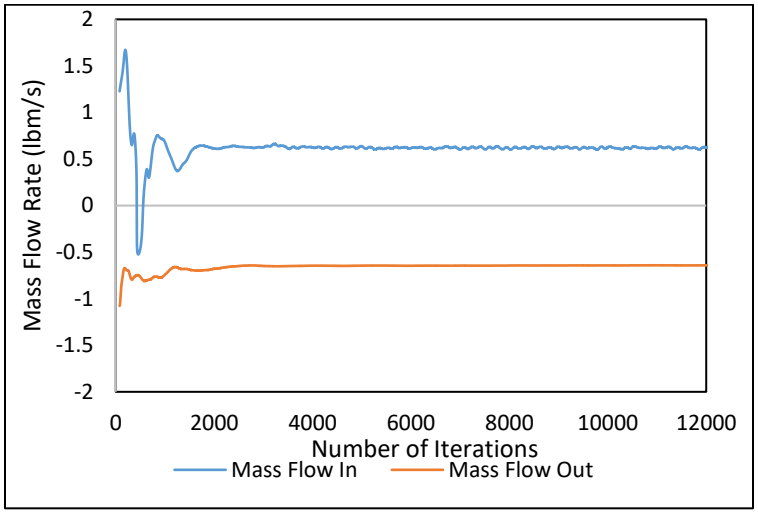

Figure 4.13. Mass balance representation for a computational fluid dynamics simulation of a 24/64-inch injection pressure-operated valve with the stem located 0.16 inches from the seat and P2 = 800 psi. The inlet mass flow was 0.612 lbs/s and the outlet mass flow was 0.634 lbs/s, which led to a net mass flow of 0.012 lbs/s (%diff = 2.12%).

Regarding model accuracy and validation, a comparison of the flow rate results against experimental data allowed us to assess the accuracy of the model. Figure 4.14 presents a comparison between results of flow rate versus downstream pressure for the RH-2 24/64 IPO from both experimental and CFD simulations. The available experimental data for these specific cases is from a dynamic flow test. Moreover, upstream pressure was high enough to maintain an orifice flow mode at the higher flow rate, which indicates that the open flow area was equivalent to the orifice area. The CFD simulations were also set for a fully open valve with a stem positioned at 0.16 inches from the seat for the 24/64-inch valve. Similar to the 1D model results, all CFD simulations in this section considered an upstream pressure of 1100 psi. For this comparison, the

experimental test data available on upstream pressure were 3.6% higher than that of the simulated CFD results, which also include additional deviation from the experimental results. The simulated flow rate curve is similar to that of the experimental results, and most of the data points fall within a 15% error range (see Figure 4.14).

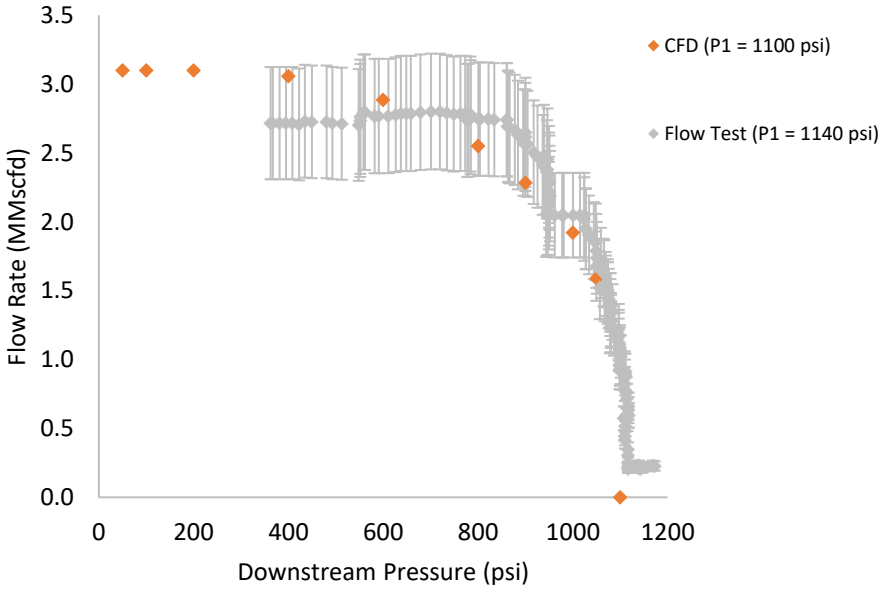

Figure 4.14. Comparison of experimental and simulated performance curves for the RH-2 24/64-inch injection pressure-operated valve with stem at dxs = 0.16 inch (full open) in the simulation and orifice flow mode in the dynamic flow test.

Figure 4.15 presents the results of flow rate versus downstream pressure for three distinct stem positions of four different valve configurations (RH-2 12/64-inch, RH-2 16/64-inch, RH-2 20/64-inch, and RH-2 24/64 inch). Since the stem positions are fixed for each curve and the equivalent flow area does not change through the valve, the performance curves are expected to have the asymptotic shape shown in the figures, resembling flow through a restriction. Finally, the

performance curves from each stem position enable the calculation of C_v and R_{cp} for each valve configuration considering the fluid dynamics scenario created by each particular valve position.

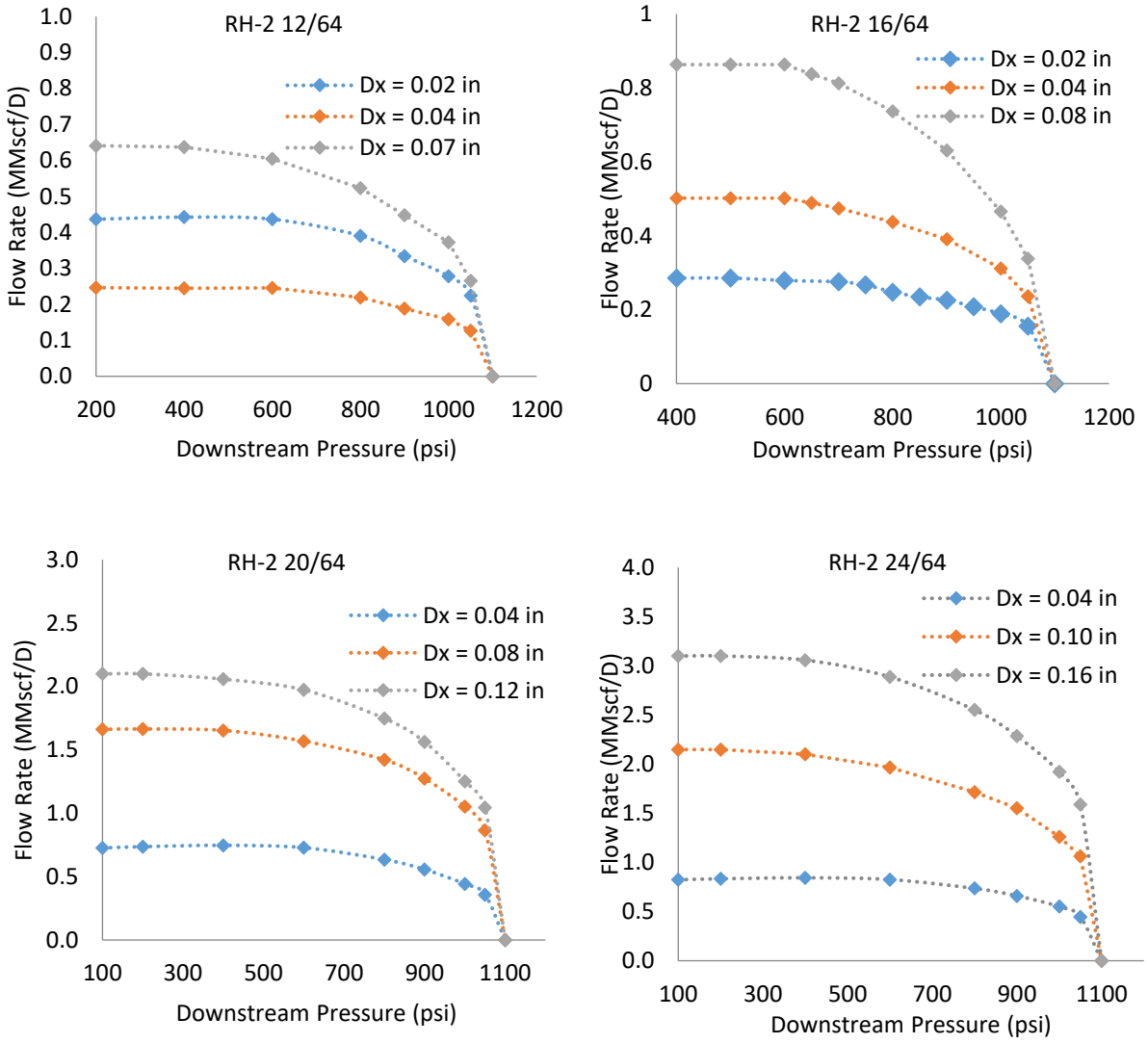

Figure 4.15. Performance curves of flow rate versus downstream pressure generated for different valve configurations and distinct stem positions.

As previously mentioned, four IPO GLV configurations were considered to evaluate the CFD modeling approach to replicate the FCT and predict the flow coefficient (C_v) and critical

pressure ratio (R_{cp}). The main reason why this valve model was chosen for the CFD simulations was the availability of FCT data with a modified valve with adjustable stem positioning. Therefore, flow coefficient test results were available for different stem positions of the RH-2 valve and orifice sizes of 12/64, 16/64, 20/64, and 24/64 inches. Although the test data did not include R_{cp} results, the VPC database provided the correlation parameters required to calculate R_{cp} for RH-2 valves with orifice sizes of 12/64 and 16/64 inches. Regarding the RH-2 20/64- and 24/64-inch valves, only a comparison of C_v was performed since the VPC database did not include results for these two valve configurations.

Figure 4.16 to Figure 4.19 present C_v and R_{cp} results from CFD simulations against the same variables calculated using test data and the VPC database. The CFD model also provides a similar accuracy when compared to the 1D model results. Generally, the simulation data and experimental results of C_v are nearly equivalent, and the CFD results are within a 15% error range for nearly all data points.

Regarding the R_{cp} values presented in Figure 4.16 and Figure 4.17, the CFD results also correlate with the VPC database results, which are within a 15% range of error. For these specific cases, results from the VPC database have constant R_{cp} values for the entire range of stem positions, with the curve showing a flat shape. Although the CFD results show greater variability, they still fall within the 15% range of error.

In general, the CFD model results for C_v and R_{cp} have a slightly higher accuracy level compared to those of the 1D mechanistic model shown in Section 4.1.3. This higher accuracy is likely related to the higher complexity of the modeling system and the modeling of the complete GLV geometry. Moreover, the flow field can be considerably affected by changes in valve design

for different valve configurations. Notably, the CFD approach allows designers or engineers to capture these changes and account for modifications in the flow field.

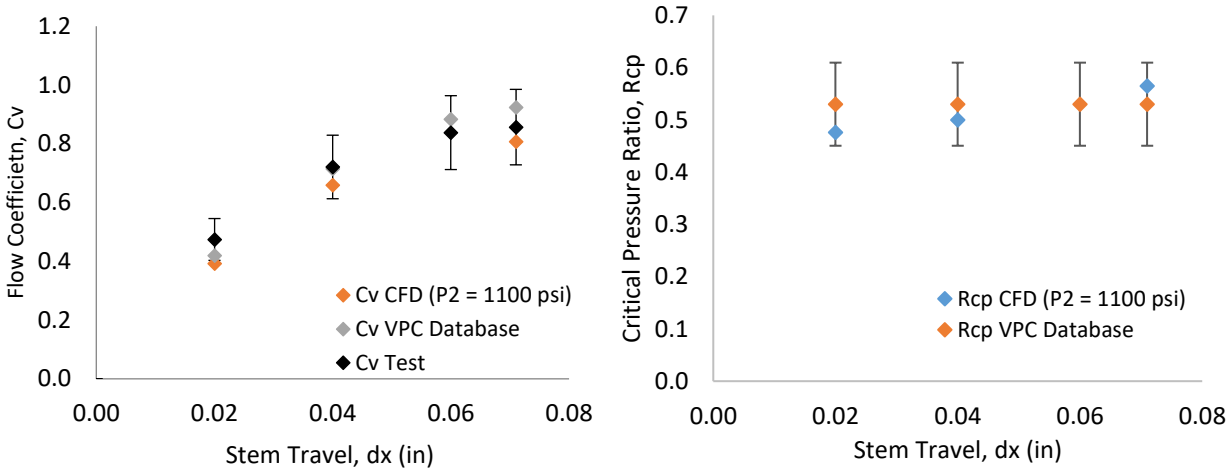

Figure 4.16. Comparison of the computational flow dynamics and experimental results for flow coefficient and critical pressure ratio (R_{cp}) for an RH-2 12/64-inch injection pressure-operated valve at three different stem positions.

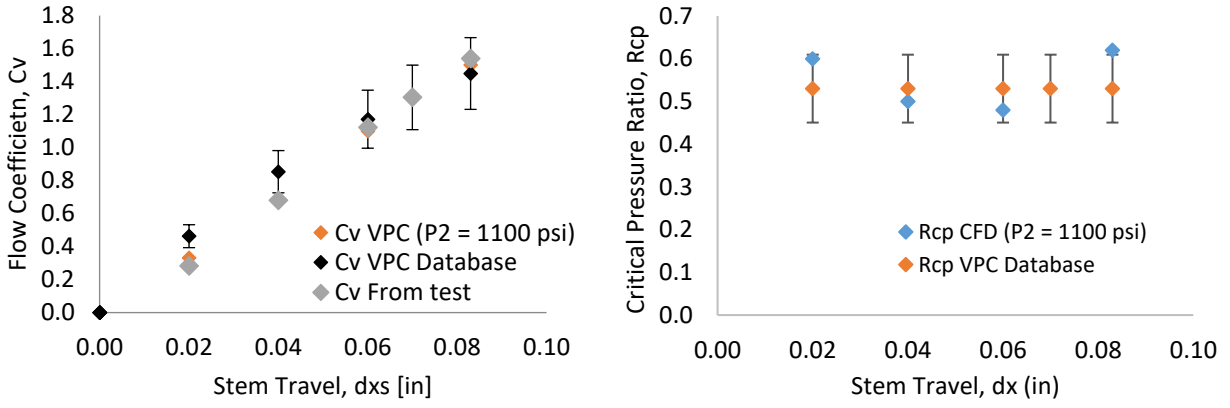

Figure 4.17. Comparison of the computational flow dynamics and experimental results for flow coefficient (C_v) and critical pressure ratio (R_{cp}) for an RH-2 16/64-inch injection pressure-operated valve at three different stem positions.

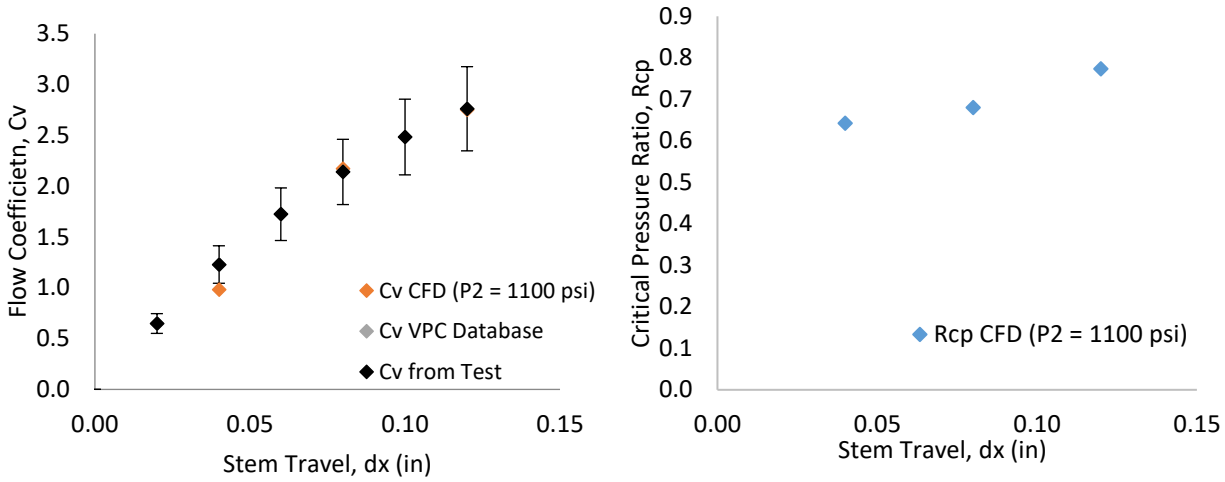

Figure 4.18. Comparison of the computational flow dynamics and experimental results for flow coefficient (C_v) and critical pressure ratio (R_{cp}) for an RH-2 20/64-inch injection pressure-operated valve at three different stem positions.

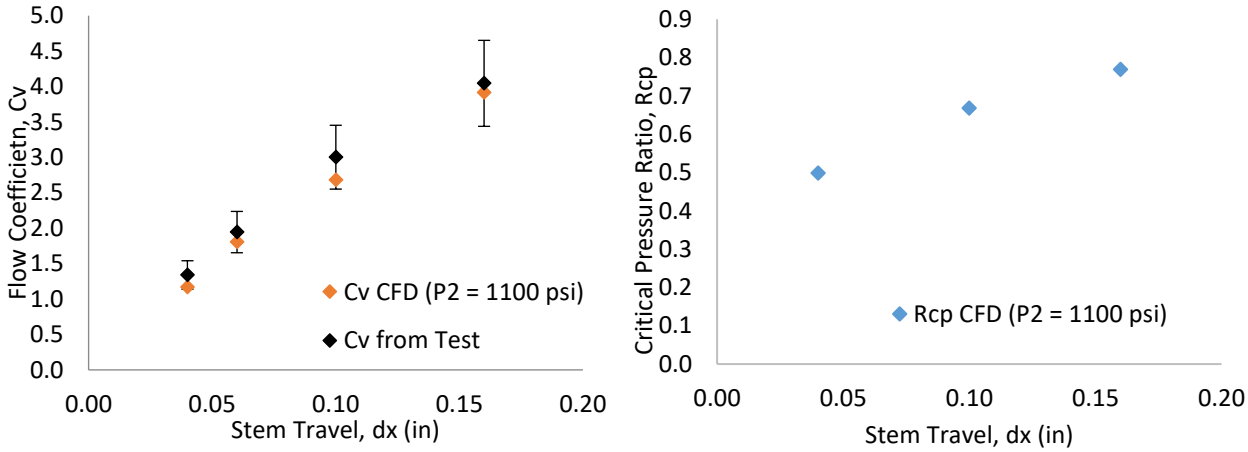

Figure 4.19. Comparison of the computational flow dynamics and experimental results for flow coefficient (C_v) and critical pressure ratio (R_{cp}) for an RH-2 24/64-inch injection pressure-operated valve at three different stem positions.

A summary of the average absolute errors for the four cases is presented in Table 4.4. Among all of the simulated cases, the highest error observed for the flow coefficient was approximately 14.6% for the 16/64-inch orifice size. For the critical pressure ratio, only two cases

have data available on the VPC database for comparison. However, the results for the 12/64- and 16/64-inch sizes show average deviations as low as 5.6%.

Table 4.4. Summary of average absolute error for four cases of computational fluid dynamics model results compared to Valve Performance Clearinghouse (VPC) database and flow capacity test results with a modified valve

Valves Name	Port size (/64 in)	Benchmark data	Average Absolute error (%)	
			Cv	Rcp
Weatherford RH-2	12	Modified valves test/VPC	7.7	5.6
Weatherford RH-2	16	Modified valves test/VPC	14.6	11.3
Weatherford RH-2	20	Modified valves test/VPC	7.3	-
Weatherford RH-2	24	Modified valves test/VPC	8.5	-

One of the main limitations of using CFD modeling is the complexity of the modeling, especially the computational capacity required to perform the simulations. For example, replicating a single C_v versus d_{xs} data point requires several CFD simulations to cover the range of pressure drops from zero flow to the critical flow condition. For instance, each simulated data point in Figure 4.16 required six CFD simulations (i.e., one for each downstream pressure). Therefore, for the three stem positions considered in this work, the total number of simulations is already 18. This number increases as additional stem positions are included in the curve to develop a more accurate correlation between C_v and d_{xs}. For each data point, an average of 4 hours of parallel simulation time is required on a high-performance computer system using 160 processing units.

Among the main advantages observed is that the CFD method allows better visualization of the details of flow fields for distinct valve configurations. Additionally, CFD software provides greater flexibility and precision in adjusting the stem position, which also speeds up the test process

since no modified valve is required. Finally, CFD analysis also enables a series of analyses that are not obtained through the test procedure, such as visualizing pressure and flow velocity contours at specific locations of the flow domain, evaluating points of choked flow through velocity field, and calculating the force distribution at sensitive elements (e.g., the stem tip).

4.2.2. Flow and Pressure Field Distribution

Besides flow capacity prediction, the CFD approach also provides a series of additional types of analysis that is relatively difficult to obtain from experimental FCTs. This includes the availability of detailed 3D simulation results for the pressure, temperature, and velocity fields along the flow path.

For instance, Figure 4.20. presents the CFD simulation results for the velocity field on a plane cutting through the center line of the valve. This figure shows the velocity field for four different orifice sizes with valve stem positioned at the maximum opening level. Also, for each result, the flow rate is also presented in Figure 4.20. Based on these results, it is possible to observe the impact of the orifice size for that, for smaller orifice sizes (12/64 and 16/64 inches), the high-velocity regions only appear near the orifice, while other parts of the valve maintain relatively low velocities. On the other hand, for larger orifice sizes (20/64 and 24/64 inches), the check valve also becomes an important flow restriction, with a considerable velocity increase in this region.

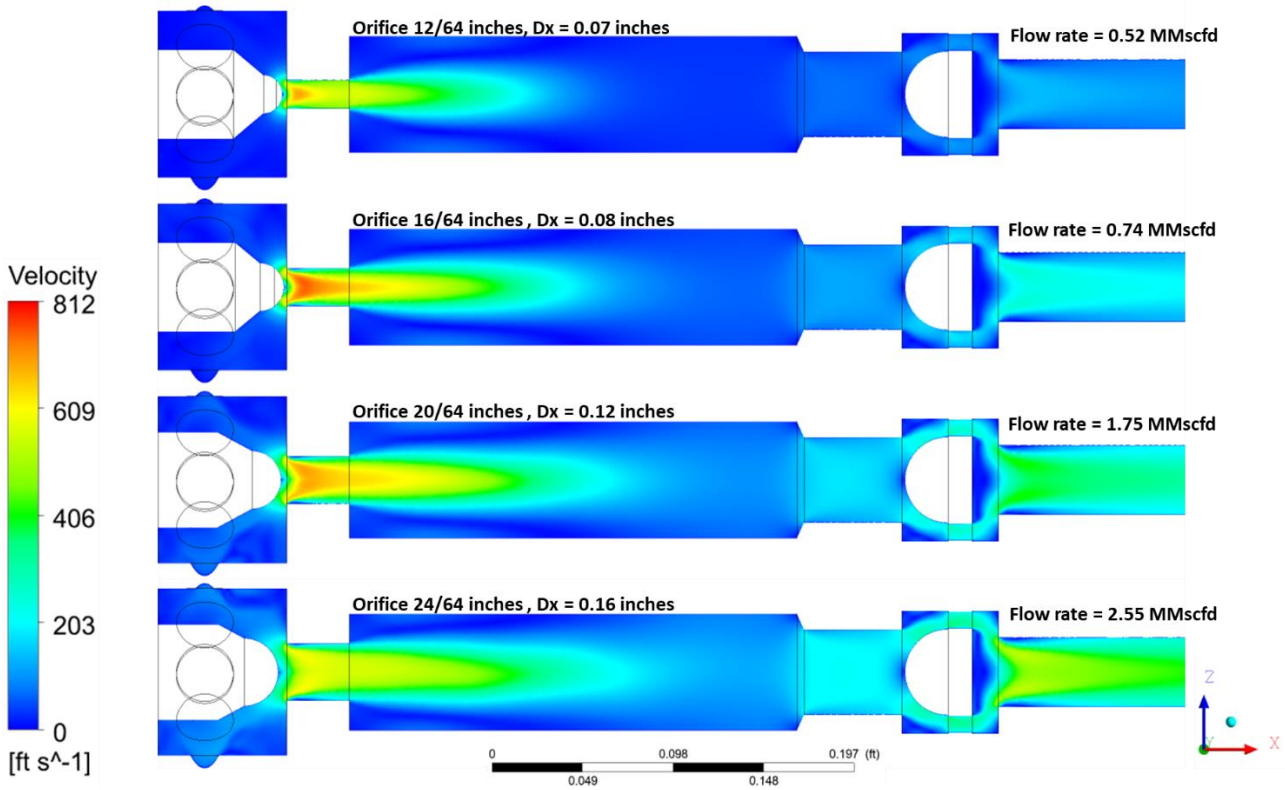

Figure 4.20. Velocity contour on a center plane cutting through the valve with different orifice sizes for injection pressure P1 = 1100 psi, production pressure P2 = 800 psi, and the stem at the fully open position.

Similarly, Figure 4.21. presents the pressure distributions over the same center plane. While the main pressure drop occurs at the orifice, a considerable pressure drop still occurs at the check valve for larger orifice sizes. The reason for this phenomenon is the flowing area for the check valve being the same for distinct orifice sizes. Additionally, by increasing the flow rate through larger orifices, the flow may experience a higher pressure drop at the fixed area check valve. These observations highlight the importance of the internal elements included in the mechanist model proposed in this study.

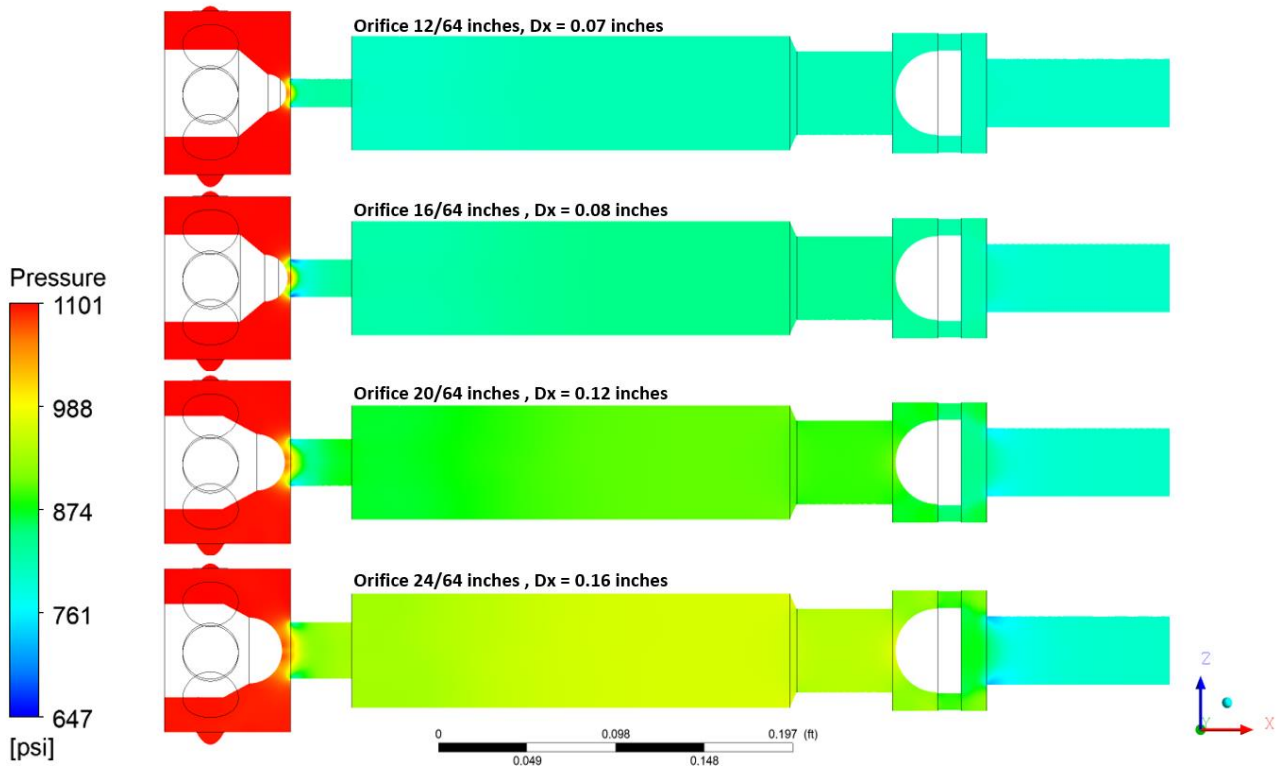

Figure 4.21. Pressure distribution on a center plane cutting through the valve with different orifice sizes for injection pressure P1 = 1100 psi, production pressure P2 = 800 psi, and the stem at the fully open position.

Figure 4.22. and Figure 4.23 present the pressure field details around the stem tip for a 16/64-inch valve with a fixed stem located 0.08 and 0.02 inches from the seat, respectively. With a larger opening, the stem tip is more exposed to the higher pressures from upstream of the orifice. A high-pressure point that may contribute to the upward movement of the stem was also observed in front of the stem tip for both the 0.08- and 0.02-inch openings. Besides the orifice zone, a pressure drop also occurred at the check valve (see Figure 4.22.) with a larger valve opening (stem located 0.08 inches from the seat). With the stem at 0.02 inches from the seat (Figure 4.23), the pressure drop at the check valve was negligible. This observation highlights the

importance of using CFD to better understand the flow and pressure fields of GLVs through analyses and visualizations that experimental approaches cannot easily provide.

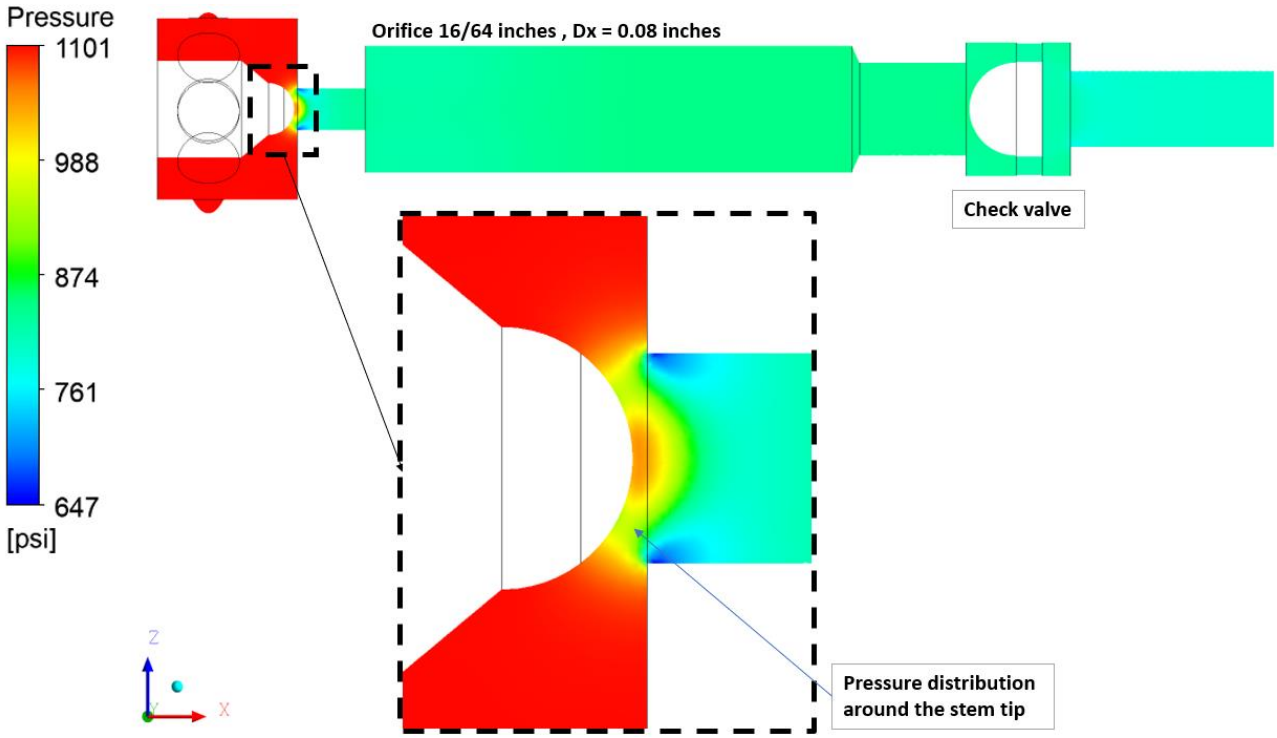

Figure 4.22. Details of the pressure field around the stem tip for a 16/64-inch injection pressure-operated gas lift valve with injection pressure P_1 = 1100 psi, production pressure P_2 = 800 psi, and stem position d_{xs} = 0.08 inches.

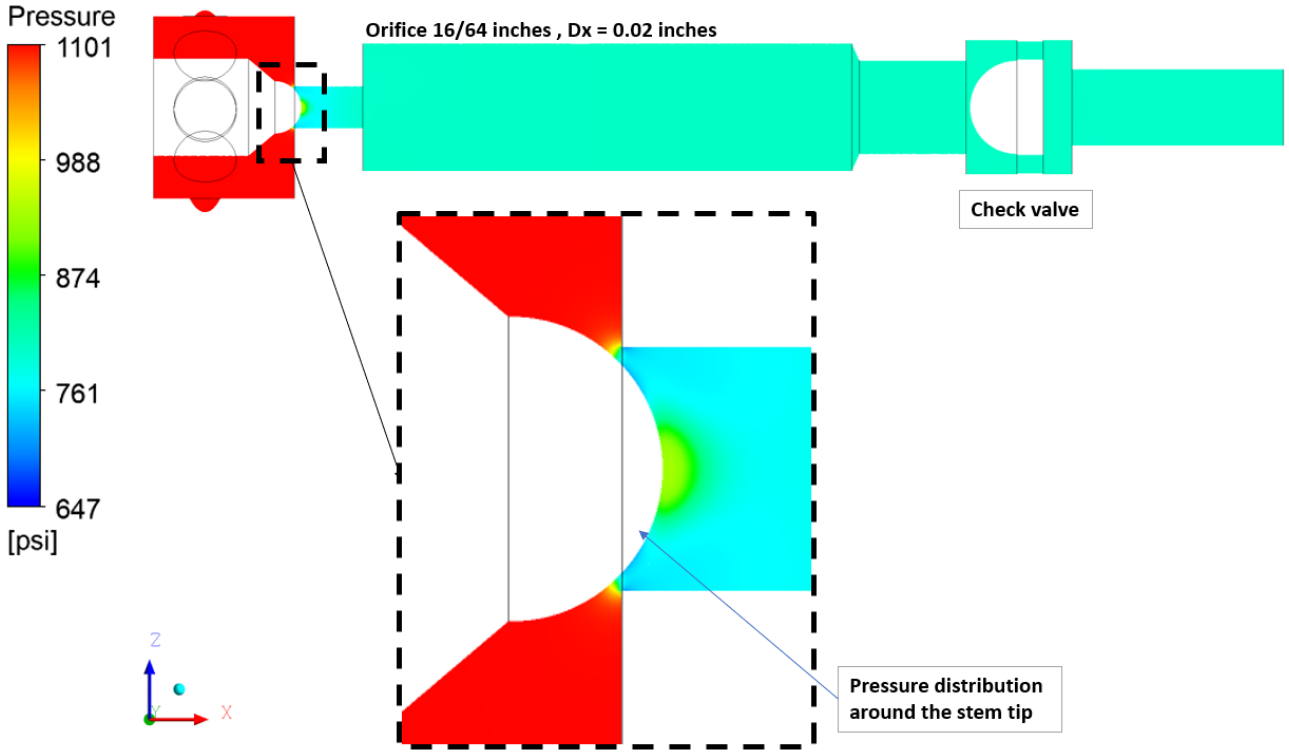

Figure 4.23. Details of the pressure field around the stem tip for a 16/64-unch injection pressure-operated gas lift valve with injection pressure P_1 = 1100 psi, production pressure P_2 = 800 psi, and stem position d_{xs}= 0.02 inches.

The pressure field at the stem tip is an important piece of information that can be obtained from CFD simulations and cannot be provided by experiments. With an accurate pressure field for a fixed stem position, it may be possible to calculate the force distribution at the tip to provide a better understanding of the force balance governing stem movement. Stem movement depends on the force balance acting on the bellows surface area (A_b) within the dome, on the stem surface, and outside of the bellows area ($A_{stem} + (A_b - A_{stem})$). Therefore, knowing the force and pressure distribution may facilitate the development of a model-based correlation to estimate the dynamic stem position for gas flow through a GLV.

Figure 4.24 and Figure 4.25 present the development of the resultant force at the stem tip as the downstream pressure increases at different stem positions for the 12/64 and 24/64-inch GLVs, respectively. The CFD approach can provide consistent resultant force data for the pressure force acting on the stem tip. Moreover, the ability of CFD to make force data available has the potential for developing modeling and correlation approaches to estimate the stem a dynamic scenario of the pressure difference between the inlet and outlet. Therefore, the use of CFD results for multiple downstream pressures and fixed stem positions facilitates the development of a modeling/correlation approach to determine the dynamic stem position, which represents a suggested path for future research in this area. Figure 4.26 presents the CFD results of the absolute value of force-x as a function of downstream pressure for three different stem positions. The injection pressure for the simulation was 1100 psi.

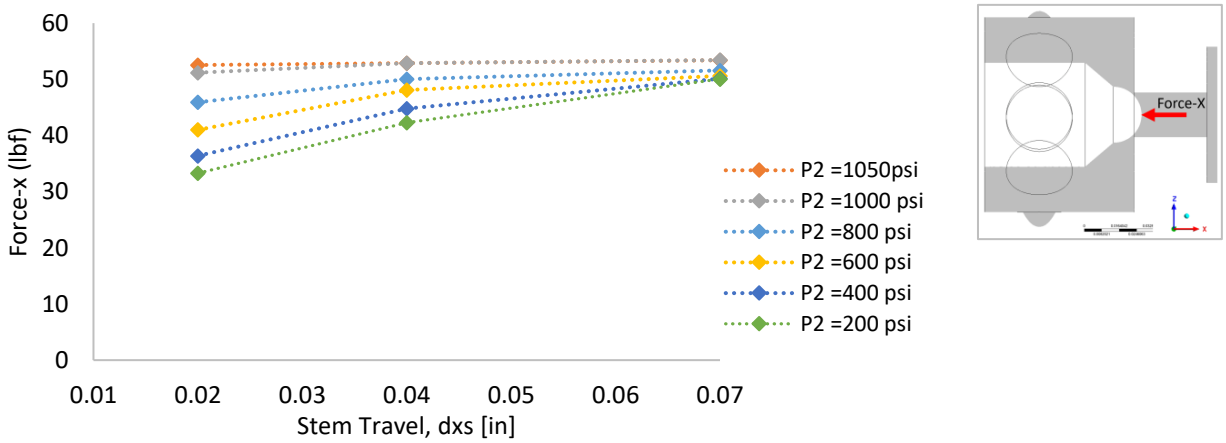

Figure 4.24. Modulus of the resultant force at the tip for the x-direction on a 12/64-inch injection pressure-operated gas lift valve. The figure in the upper right-hand corner indicates the direction of the force-x according to the coordinate system defined for the CFD model.

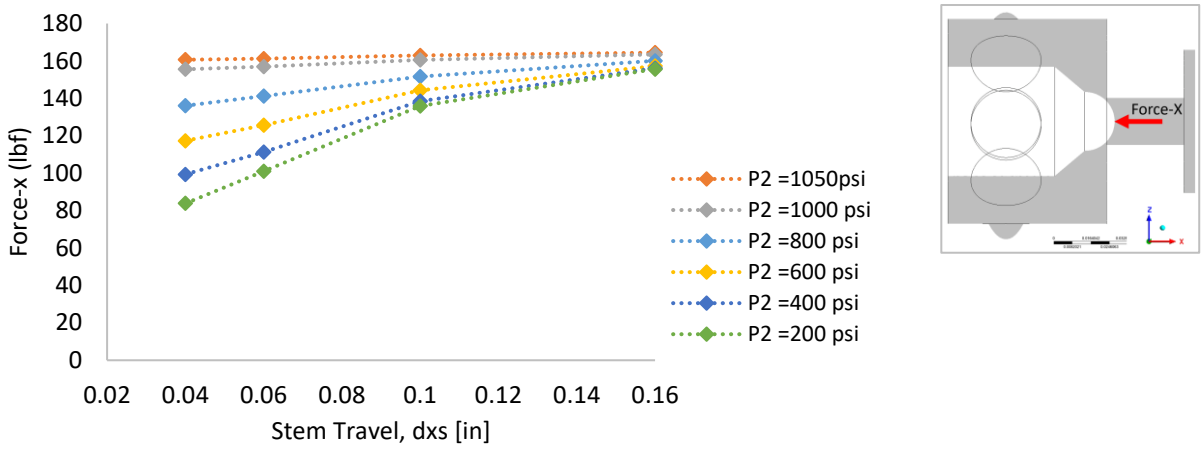

Figure 4.25. Modulus of the resultant force at the tip for the x-direction on a 24/64-inch injection pressure-operated gas lift valve. The figure in the upper right-hand corner indicates the direction of the force-x according to the coordinate system defined for the CFD model.

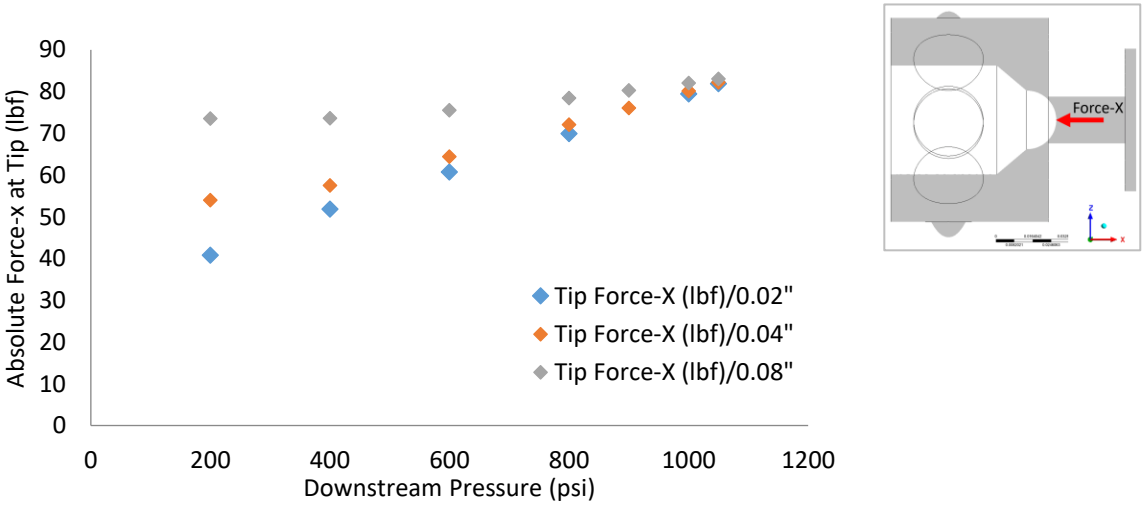

Figure 4.26. Absolute force at the x-direction versus downstream pressure at three different stem positions. The figure in the upper right-hand corner indicates the direction of the force-x according to the coordinate system defined for the CFD model.

Chapter 5. Conclusion and Recommendations

This study presented the use of a 1D model and a 3D CFD model to obtain the flow coefficient C_v and critical pressure ratio R_{cp} for GLVs. The main advantage of these models compared to previous models is the number of experimental tests used to calibrate both 1D and CFD 3D models to obtain C_v and R_{cp}.

The results for flow capacity modeling using both 1D mechanistic modeling as well as CFD models show agreement in experimental data (or data from the VPC database) within the range of ±15% accuracy for both C_v and R_{cp} for valves with different manufacturers and orifice port sizes. A sensitivity analysis of the upstream pressure was also carried out, which showed a weak effect of upstream pressure in the estimation of C_v and R_{cp}, with variations lower than 5% for upstream pressure varying from 500 to 2,000 psi.

Another important conclusion is related to the effectiveness of using the check valve discharge coefficient (C_d) and the open flow area to adjust and calibrate the model. Calibration using only one data point from the dynamic flow test results in a considerable reduction in the time required to perform an FCT. Moreover, the calibrated 1D mechanistic model eliminates the need to modify a GLV to perform FCTs, while also providing results within a ±15% range of error for both C_v and R_{cp}.

The disadvantages of the 1D modeling technique include the model being simplified and considering 3D area changes as equivalent circular diameters. On the other hand, the CFD model accounts for 3D geometry variations in the gas flow path and can also consider the impact of the internal elements of the valve (e.g., check valve design and changes in internal diameter).

Therefore, the CFD model results show cases with averaged absolute errors as low as 6.3% for C_v and 5.6% for R_{cp} for the specific valve and pressures considered.

Besides achieving greater accuracy for the estimation of C_v and R_{cp}, the CFD method also allows the estimation of pressure, temperature, and velocity fields across the GLV, which is not easily obtained from valve tests. For instance, the CFD velocity and pressure contour facilitates the assessment of the check valve effect on the flow field for GLVs with larger port sizes. In this case, a 24/64-inch orifice showed a larger pressure drop and higher velocities (approximately 500 ft/sec) at the check valve. The CFD model also enables the estimation of the pressure distribution around the stem tip, which can subsequently be used to better understand stem movement under dynamic conditions.

On the other hand, the disadvantages of the CFD modeling approach include the higher complexity of the model and the long time required to perform the simulations. The phenomenon of high-pressure compressible flow is relatively complex to model and requires powerful computational processing capabilities. Also, the fact that the detailed geometry of the GLV may not be always available is another drawback of this modeling approach.

Based on the outcomes of this thesis, some recommendations for future research projects include:

- An investigation of the turbulence model that best suits this methodology for the CFD modeling of GLVs.
- An exploration of the potential for using CFD pressure distribution results at the stem tip to predict the force balance for all downstream pressures. This method could facilitate a

better understanding of the dynamics of stem movement and aid in the development of a correlation to predict the stem position for a live valve scenario.

- Built an experimental setup with an instrumented gas lift valve to measure internal parameters and force acting at the ball in order to validate the CFD method.

Appendix. Computational Modeling

The computational geometry of the fluid domain and the mesh (or discretized fluid domain) were created using Ansys SpaceClaim and the Ansys Meshing Engine, respectively. The fluid domain volume consists of the valve's internal void space when the check valve is fully open. To assess the accuracy of the mesh size in terms of element number, a mesh independence test was performed.

Since the models account for distinct stem positions, each stem travel represents a different mesh that must be created. Performing a mesh independence study for each different model may be infeasible due to the time required to evaluate each individual model. Therefore, for this thesis, the mesh independency test considered only one valve geometry, while the characteristics of the resulting mesh were escalated for the other models. Specifically, the 16/64-inch orifice valve with a stem positioned 0.02 inches from the seat was employed in this test. This geometry was selected because it is intermediate in terms of orifice size and the meshing strategy can be extrapolated for other geometries. A total of three distinct meshes were built with increasing mesh sizes (see Table A.0.1). The minimum and maximum element sizes shown in Table A.0.1 were used to balance the refinement in tight flow regions (e.g., the open area at the orifice) and wider flow areas in the domain. To enforce higher refinement close to the orifice, a meshing method known as body sizing was used, and a sphere of influence set the elements within the sphere to the minimum element size. Figure A.2 presents the location of the sphere of influence, which manages to fix the elements' minimum size as required.

These three mesh configurations were used to simulate nitrogen flow through the valve with an inlet pressure of 1100 psi and outlet pressure of 800 psi. Subsequently, a comparison of

pressure and velocity evolution across the path from the inlet to the outlet zones facilitates the evaluation of which mesh configuration was better. Figure A.1 presents the location of the fluid path considered for the mesh test.

Table A.0.1. Mesh configurations regarding element size for the mesh independence test as well as the time required for the simulations to converge for each mesh

Mesh	Number of cells	Min. element size (inches)	Max. element size (inches)	Time (min)
1	1,843,728	0.004537	0.1800	157
2	3,342,345	0.003337	0.8087	185
3	4,525,432	0.003900	0.0219	487

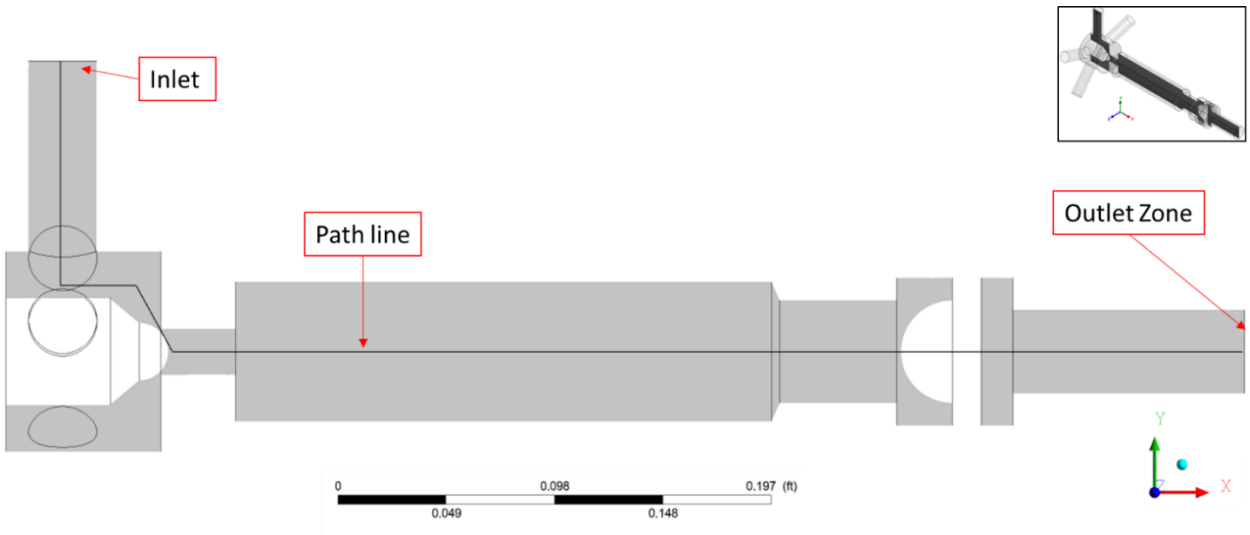

Figure A.1. Midplane across the computational geometry with an indication of the path line used to sample velocity and pressure evolution along the computational domain.

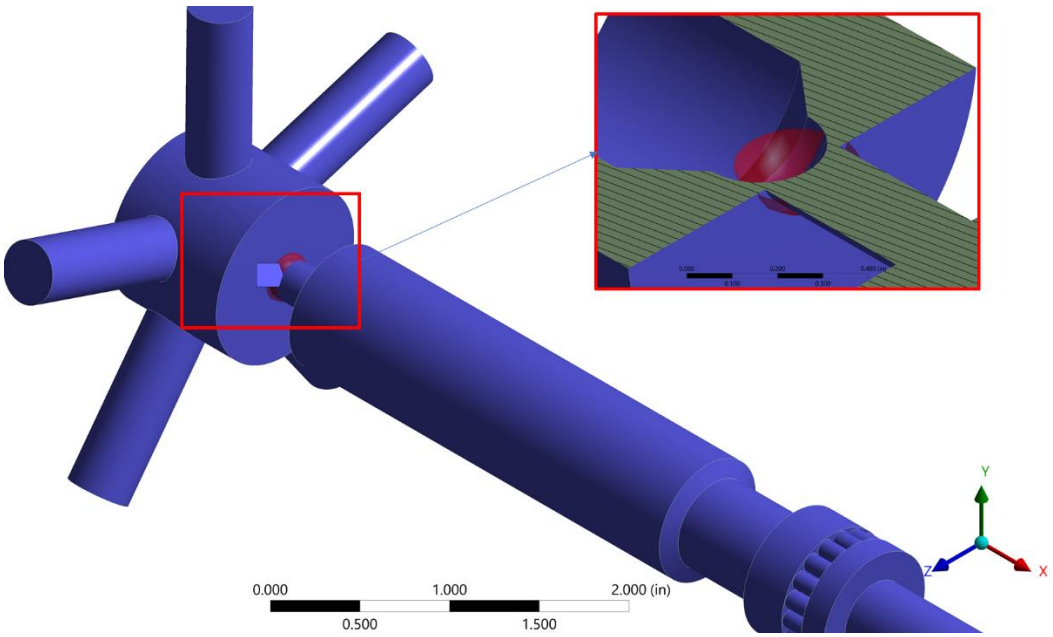

Figure A.2. Location of the sphere of influence, which enforces higher mesh refinement or resolution at the open area between the orifice and stem tip.

Figure A.3 presents the results of velocity evolution along the line path described for the mesh test. The velocity peaks at approximately 1 inch from the beginning of the line, which matches the position of the restriction at the orifice. Upon comparing the performance of the three meshes to predict the velocity profile, the results are fairly similar for the majority of the flow path. However, mesh 1 shows a slightly higher velocity at the beginning of the path and orifice zone. On the other hand, meshes 2 and 3 have larger cell counts and show more consistent results with only small deviations. Mesh independence was observed from mesh 2 to 3, which returned similar results despite the cell count increasing to over 1 million cells for mesh 3. Similar behavior occurred with pressure evolution through the line (see Figure A.4). The pressure calculated at the beginning of the path using mesh 1 also shows a slight deviation from the results of meshes 2 and 3.

Based on both outcomes, one can observe that meshes 2 and 3 show a higher level of mesh size independence. Since these two mesh configurations return very similar results—and considering the processing time required to run both models—the characteristics of mesh 2 appear to be more efficient for the simulations. Thus, the characteristics of mesh 2 were replicated for the other 12 meshes in this thesis.

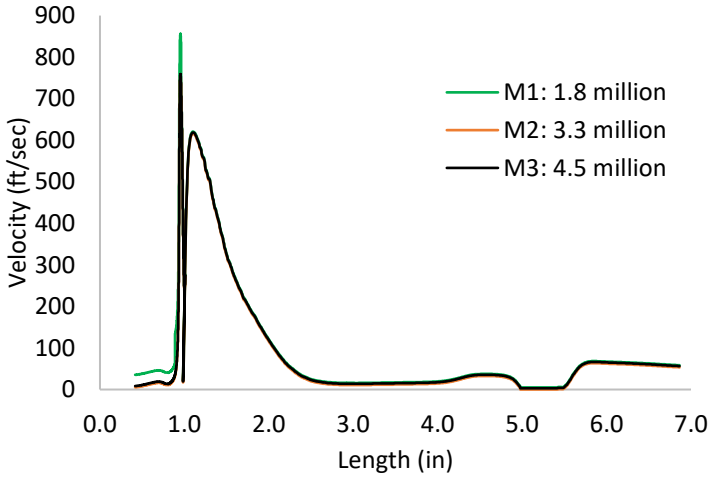

Figure A.3. Comparison of velocity evolution profiles along the path lines shown in Figure A.1

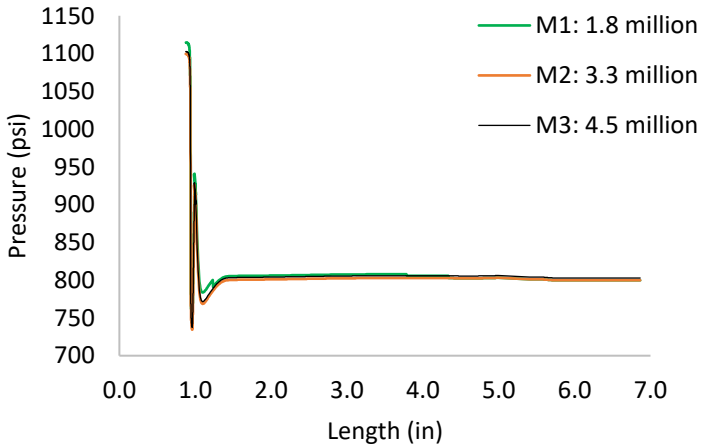

Figure A.4. Comparison of pressure evolution profiles along the path lines shown in Figure A.1

References

Altarabulsi, K. A. K. (2018). *An Improved Method To Calculate Gas-Lift Valve Set Pressure And Valve Performance Curves* (Vol. 1, Issue December). Louisiana State University.

Andrei Nikolaevich Kolmogorov. (1991). The local structure of turbulence in incompressible viscous fluid for very large Reynolds numbers. *Proceedings of the Royal Society of London. Series A: Mathematical and Physical Sciences*, *434*(1890), 9–13. https://doi.org/10.1098/rspa.1991.0075

Ansys. (2014). *8.16.1 The Aungier-Redlich-Kwong Real Gas Model*. https://www.afs.enea.it/project/neptunius/docs/fluent/html/ug/node335.htm

ANSYS, I. (2013). *ANSYS Fluent Theory Guide* (v. 15317, n.; pp. 724–746).

API, R. (2001). 11V2, Recommended Practice for Gas Lift Valve Performance Testing. In: Washington, DC: API.

API (2010). *Flow-control Devices for Side-pocket Mandrels* rp19G2. Washington DC. API.

API Recommended Practice 520: Sizing, Selection, and Installation of Pressure-relieving Devices, American Petroleum Institute (2013).

Ashford, F. E. Pierce, P. E. (1975). Determining multiphase pressure drops and flow capacities in down-hole safety valves. *Journal of Petroleum Technology*, *27*, 1–145.

ASME. (1971). *Fluid Meters: Their Theory and Application*. American Society of Mechanical Engineer.

Aungier, R. H. (1995). A Fast, Accurate Real Gas Equation of State for Fluid Dynamic Analysis Applications. *Journal of Fluids Engineering*, *117*(2), 277–281. https://doi.org/10.1115/1.2817141

Azim, R. A. (2019). Full Field Production Optimization Study Using Nodal Analysis Technique. *Petroleum and Coal. Coal.*, *67*(12), 317–319. https://doi.org/10.1021/ac00108a600

Bertovic, D. (1995). *Unified model for gas-lift valve performance incorporating temperature effects*. The University of Tulsa, Tulsa, Oklahoma.

Bertovic, D., Doty, D., Blais, R., & Schmidt, Z. (1997, March 9). Calculating Accurate Gas-Lift Flow Rate Incorporating Temperature Effects. *All Days*. https://doi.org/10.2118/37424-MS

Brahma, I. (2019). Measurement and Prediction of Discharge Coefficients in Highly Compressible Pulsating Flows to Improve EGR Flow Estimation and Modeling of Engine Flows. *Frontiers in Mechanical Engineering*, *5*(May), 1–18. https://doi.org/10.3389/fmech.2019.00025

Brill, J. P., & Beggs, H. D. (1991). *Two-phase Flow in Pipes: Univ*.

Buchan, A. G., Yang, L., & Atkinson, K. D. (2020). Predicting airborne coronavirus inactivation by far-UVC in populated rooms using a high-fidelity coupled radiation-CFD model. *Scientific Reports*, *10*(1), 1–7. https://doi.org/10.1038/s41598-020-76597-y

Cable, M. (2009). *An Evaluation of Turbulence Models for the Numerical Study of Forced and Natural Convective Flow in Atria* (Issue May). Queen's University.

Cook, H. L., & Dotterweich, F. H. (1946). *Report on Calibration of Positive Flow Beans Manufactured by Thornhill-Craver Company, Inc., Houston, Texas, Aug. 10, 1946*. 1–2. https://books.google.com/books?id=K8dstwAACAAJ

Cook, H. L., & Dotterweich, F. H. (1981). *Report on calibration of positive flow beans manufactured by Thornhill-Craver Company, Inc Department of Energy*.

Coutinho, R. (2018). *Experimental and Numerical Investigation of Liquid-Assisted Gas-Lift Unloading* [LSU]. PhD. Dissertation. Louisiana State University. https://digitalcommons.lsu.edu/gradschool_dissertations/4625

Decker, K. L. (1986). Computer modeling of gas-lift valve performance. *Proceedings of the Annual Offshore Technology Conference*, May 1986.

Decker, K. L. (1993a). Gas-lift valve performance testing. *Production Operations Symposium, March*, 347–356. https://doi.org/10.2118/25444-ms

Decker, K. L. (1993b). Gas-lift valve performance testing and data correlation. *SPE Production and Facilities*, *8*(2), 101–107. https://doi.org/10.2118/22789-PA

Decker, K. L. (2014). *The Valve Performance Clearing House, VPC Help Contents (VPCTM)*. Decker Technology.

Driskell, L. (1983). *Control Valve Selection and Sizin*. Instrument Society of America, Research Triangle Park, North Carolina .

Economides, M. J. (2013). *Petroleum production systems* (2nd ed.). Pearson Education Upper Saddle River, NJ : Prentice Hall, c2013. 2nd ed.

Elldakli, F. (2015). *Enhanced Gas Lift Valve Performance for Sharp Edged Seat Using Larger Ball Sizes*. Master Thesis. Texas Tech University.

Elldakli, F., & Soliman, M. (2017). Optimum design for new gas lift valve seat. *Journal of Petroleum Science and Engineering*, *149*(June 2016), 456–464. https://doi.org/10.1016/j.petrol.2016.10.062

Faustinelli, J. G., & Doty, D. R. (2001). Dynamic Flow Performance Modeling of a Gas-Lift Valve. *SPE Latin American and Caribbean Petroleum Engineering Conference*. https://doi.org/10.2523/69406-ms

Hepguler, G. (1988). *Dynamic model of gas-lift valve performance*. The University of Tulsa, Tulsa,

Oklahoma.

Hepguler, G., Schmidt, Z., Blals, R. N., & Doty, D. R. (1993). Dynamic model of gas-lift valve performance. *JPT, Journal of Petroleum Technology*, *45*(6), 576–583. https://doi.org/10.2118/21637-PA

Hérnandez, A. (2016). *Fundamentals of Gas Lift Engineering Well Design and Troubleshooting*. Gulf Professional Publishing, Elsevier, 2016.

Kabir, E., Emadi, H., McElroy, P., Elldakli, F., & Young, M. (2020). Optimizing seat and ball combination of actual gas lift valve: An experimental and CFD simulation study. *Society of Petroleum Engineers - SPE Artificial Lift Conference and Exhibition - Americas 2020, ALCE 2020*. https://doi.org/10.2118/201119-ms

Kontogeorgis, G. M., & Tassios, D. P. (1997). Critical constants and acentric factors for long-chain alkanes suitable for corresponding states applications. A critical review. *Chemical Engineering Journal*, *66*(1), 35–49. https://doi.org/10.1016/S1385-8947(96)03146-4

Kumar, A., Ghobadian, A., & Nouri, J. M. (2020). Assessment of cavitation models for compressible flows inside a nozzle. *Fluids*, *5*(3). https://doi.org/10.3390/fluids5030134

Meriem-Benziane, M., Bou-Saïd, B., & Abdelkader, B. (2020). A CFD modeling of oil-water flow in pipeline: Interaction analysis and identification of boundary separation. *Petroleum Research*. https://doi.org/10.1016/j.ptlrs.2020.10.004

Mokhtari, K., & Waltrich, P. J. (2016). Performance evaluation of multiphase flow models applied to virtual flow metering. *Advances in Fluid Mechanics XI*, *1*(Afm), 99–111. https://doi.org/10.2495/afm160091

Najar, N. A., Dandotiya, D., & Najar, F. A. (2013). Comparative Analysis of K-Epsilon and Spalart-Allmaras Turbulence Models for Compressible Flow Through a Convergent-Divergent Nozzle. *The International Journal of Engineering and Science*, *2*(8), 8–17. www.theijes.com

OLGA. (n.d.). OLGA Dynamic Multiphase Flow Simulator: Schlumberger. *2015*.

Owczarek, I., & Blazej, K. (2003). Recommended Critical Temperatures. Part I. Aliphatic Hydrocarbons. *Journal of Physical and Chemical Reference Data*, *32*(4), 1411–1427. https://doi.org/10.1063/1.1556431

PIPESIM. (2018). *PIPESIM Steady-State Multiphase Flow Simulator: Schlumberger*.

Pittman, R. W. (1982). Gas lift design and performance. *Society of Petroleum Engineers - International Petroleum Exhibition and Technical Symposium, IPETS 1982*, 1–8. https://doi.org/10.2118/9981-ms

Poling, B. E., Prausnitz, J. M., & O'Connell, J. P. (1959). The Properties Of Gases and Liquids. In *Physics Today* (5th ed., Vol. 12, Issue 4). McGRAW-HILL.

https://doi.org/10.1063/1.3060771

Pope, S. B. (2001). Turbulent Flows. *Measurement Science and Technology*, *12*(11), 2020–2021. https://doi.org/10.1088/0957-0233/12/11/705

Potter, M. C., Wiggert D.. (2010). *Mechanics of Fluids*. Cengage (ed.); 3rd SI ed. Prentice Hall PTR.

Raback, P., Ruokolainen, J., & Lyly, M. (2001). Fluid-structure interaction boundary conditions by artificial compressibility. *ECCOMAS Computational Fluid Dynamics Conference*, *September*, 4–7.

Rasouli, H., Rashidi, F., & Karimi, B. (2013). Integrated gas lift system optimization. *Theoretical Foundations of Chemical Engineering*, *47*(4), 397–405. https://doi.org/10.1134/S0040579513040271

Reynolds, O. (1895). IV. On the dynamical theory of incompressible viscous fluids and the determination of the criterion. *Philosophical Transactions of the Royal Society of London. (A.)*, *186*, 123–164. https://doi.org/10.1098/rsta.1895.0004

Ruiz, R., Brito, A., & Marquez, J. (2014). Evaluation of multiphase flow models to predict pressure gradient in vertical pipes with highly viscous liquids. *SPE Latin American and Caribbean Petroleum Engineering Conference Proceedings*, *1*, 804–811. https://doi.org/10.2118/169328-ms

Sagar, R. (1991). *Improved dynamic model of gas-lift valve performance*. The University of Tulsa,1991. Master Thesis.

Sakthivel, R., Vengadesan, S., & Bhattacharyya, S. K. (2011). Application of non-linear k-e turbulence model in flow simulation over underwater axisymmetric hull at higher angle of attack. *Journal of Naval Architecture and Marine Engineering*, *8*(2), 149–163. https://doi.org/10.3329/jname.v8i2.6984

Sami, N. A., & Turzo, Z. (2020). Computational fluid dynamic (CFD) simulation of pilot operated intermittent gas lift valve. *Petroleum Research*, *5*(3), 254–264. https://doi.org/10.1016/j.ptlrs.2020.05.002

Shahri, M. A. (2011). *Simplified and Rapid Method for Determining Flow Characteristics of Every Gas-Lift Valve (GLV)* (Issue August). Texas Tech University.

Sladkov, I. B. (2001). Physicochemical properties of methyl- and ethylhalosilanes. *Russian Journal of Applied Chemistry*, *74*(11), 1801–1805. https://doi.org/10.1023/A:1014807719997

Tang, Y., Schmidt, Z., Blais, R. N., & Doty, D. R. (1999). Transient dynamic characteristics of the gas-lift unloading process. *SPE Journal*, *4*(3), 268–277. https://doi.org/10.2118/57659-pa

Trindade, F., Costa, N., Jr, R., Meri, J., Valentim, E., & Sim, F. (2021). *Atmospheric dispersion*

and urban planning : An interdisciplinary approach to city modeling. *70*(August 2020). https://doi.org/10.1016/j.scs.2021.102882

Tunzo, Z., & Takacs, G. (2009). CFD techniques determine gas-lift valve behavior. *Oil and Gas Journal*, *107*(22), 46–51.

Turzo, B. Z., & Takacs, G. (2009). Special Report : CFD techniques determine gas - lift valve behavior. *Oil and Gas Journal*, *22*, 1–12.

Uygun, M., Onbaşıoğlu, S., & Avcı, S. (2004). (2004). Turbulence Modeling for Computational Fluid Dynamics, Part I: Conceptual Outlook. *Journal of Aeronautics and Space Technologies,* 1(4), 19-26.

Versteeg, H. K., & Malalasekera, W. (1980). An introduction to computational fluid dynamics: the finite volume method. *Computer Physics Communications*, *20*(2), 321–322. https://doi.org/10.1016/0010-4655(80)90010-7

Versteeg, H. K., & Malalasekera, W. (2007). (2007). *An introduction to computational fluid dynamics: the finite volume method.* Education., Pearson.

Xu, Z., Richard, B. M., & Kritzler, J. H. (2013). Smart gas lift valves enhance operational efficiency of offshore wells. *Proceedings - SPE Annual Technical Conference and Exhibition*, *4*, 2529–2533. https://doi.org/10.2118/166291-ms

Yusof, S. N. A., Asako, Y., Sidik, N. A. C., Mohamed, S. B., & Japar, W. M. A. A. (2020). A short review on rans turbulence models. *CFD Letters*, *12*(11), 83–96. https://doi.org/10.37934/cfdl.12.11.8396

Vita

Felipe Simoes Maciel, is a native of São Mateus, Espírito Santo, Brazil, received his first Master's Degree in Environmental Engineering from Universidade Federal do Espírito Santo (UFES) and Bachelor's Degree in Petroleum Engineering, also from Universidade Federal do Espirito Santo. Felipe also holds and Associate Degree in Electrotechnical from the Instituto Federal do Espírito Santo (UFES). Felipe anticipates graduating with a Master Degree in Petroleum Engineering in August 2021.